Embrittlement induced by the synergistic effects of radiation damage and helium in structural steels

THÈSE N^{O} 6824 (2015)

PRÉSENTÉE LE 26 OCTPBRE 2015
À LA FACULTÉ DES SCIENCES DE BASE
LABORATOIRE DE PHYSIQUE DES RÉACTEURS ET DE COMPORTEMENT DES SYSTÈMES
PROGRAMME DOCTORAL EN SCIENCE ET GÉNIE DES MATÉRIAUX

ÉCOLE POLYTECHNIQUE FÉDÉRALE DE LAUSANNE

POUR L'OBTENTION DU GRADE DE DOCTEUR ÈS SCIENCES

PAR

Kun WANG

acceptée sur proposition du jury:

Prof. A. Fontcuberta i Morral, présidente du jury
Dr Ph. Spätig, Dr Y. Dai, directeurs de thèse
Dr J. Henry, rapporteur
Dr M. Victoria, rapporteur
Dr A. Hessler-Wyser, rapporteuse

ÉCOLE POLYTECHNIQUE
FÉDÉRALE DE LAUSANNE

Suisse
2015

Acknowledgements

First of all, I would like to express my sincere gratitude to Dr. Yong Dai, the leader of spallation materials team, Paul Scherrer Institute, Villigen, who initiated the research described in this thesis. He arranged my work and help in the interpretation of experimental results, and his insights and discussions have been invaluable. Specifically, I am indeed impressed for his active and hard working attitude.

I am extremely grateful to Dr. Philippe Spätig of Laboratory for Nuclear Materials at Paul Scherrer Institute, Villigen. He arranged the enrollment to EPFL for me and gave me the general guidance of the thesis. Particularly, his useful discussion and attentive correction on the manuscript help me very much to write the thesis. I am really inspired by his responsibility.

I thank Mr. Roger Brun, who provided vast amounts of support throughout the whole duration of the PhD in work and my personal matter. His joke and funny stories make the work in office and hot lab not so boring. Besides, I would like to thank Mr. Reuning Hartmut and Mr. Mueller Mario for their help in the active sample transfer in hot lab.

I also want to thank Dr. Elisabeth Mueller, the manager of Electron Microscopy Facility at Paul Scherrer Institute, Villigen. Her selfless help and sincerely encouragement for me really support my work of the electron microscopy at Paul Scherrer. Many thanks to Mrs. Julijana Krbanjevic for the introduction and help with FIB-SEM and Mrs. Eugenia Minikus for the introduction of TEM.

I would like to say words of appreciation to my friends and colleagues at PSI for all their help: Dr. Tao Zhang, Dr. Tielong Shen, Dr. Wenwang Wu, Dr. Vladimir Krsjak, Dr. Viacheslav Kuksenko, Dr. Christiane Vieh, Mr. Hongen Ge, Dr. Rui Liu, Ms. Jemila Habainy, Dr. Barbara Horvath, Dr. Jiaochao Chen, Dr. Susan Abolhassani, Mr. Juxin Bai.

I also would like to thank Dr. Manuel Pouchon, Mrs Barbara Furger for their support in administrative matters. This work was supported by PSI and EU FP7 GETMAT project.

Finally, I want to thank my family for their everlasting understanding and support and especially my wife, for her silent and selfless love and care during my PhD period.

Abstract

Ferritic/martensitic steels are candidate materials for fusion reactor structural components, liquid metal containers of spallation neutron sources, and accelerator driven systems, with good radiation resistance and thermo-mechanical properties. However, embrittlement resulting from the combined effects of radiation induced displacement damage (measured in dpa = displacement per atom) and transmutation products, especially helium gas, is one of the key issues.

Four different steels were selected for mechanical and microstructural studies to understand the mechanisms of embrittlement induced by the combined effects of displacement damage and helium after irradiation in SINQ, the Swiss spallation source. The irradiations conditions were in the range: 10.7 – 20.4 dpa with 850-1750 appm He at 160-300 °C. The evolution of the mechanical properties after irradiation was investigated by tensile and hardness tests. Radiation-induced defect clusters and helium bubbles were quantified by transmission electron microscopy (TEM). Emphasis was put on the deformation mechanisms under the different observed fracture mode, (ductile, quasi-cleavage and intergranular), whose occurrence depends on the irradiation conditions (dpa, He content and irradiation temperature).

The tensile stress-strain curves and the scanning electron microscopy images of fracture surfaces showed distinct fracture mechanisms under different irradiation and test conditions. The tensile tests showed a yielding stress increase and loss of ductility of irradiated specimens. Hardness was measured on the specimens before tensile testing. The hardness results demonstrated an increasing trend with irradiation dose and helium content.

TEM observations were done for all irradiated fractured specimens. Small defect clusters were observed in the 12.3 dpa specimen, but large defect clusters with loop-shape were very few. In the specimens of 17.2, 17.7 and 20.4 dpa, many large dislocation loops were detected besides small clusters. In addition, helium bubbles were observed in all specimens. The average size of defect clusters increased from 4.2 nm to 11.8 nm with dose increasing from 12.3 dpa to 20.4 dpa, whereas the number density did not change significantly. Meanwhile, the average size of visible helium bubbles increased from 1.03 nm to 1.93 nm. The microstructures in deformed area of irradiated specimens were observed and defect free channels with $\{110\}$ and $\{112\}$ slip planes were found in some specimens, indicating plastic flow localization. The average width of the channels is about 100 nm.

Regarding the brittle samples, the TEM-lamella were extracted directly below intergranular fracture surfaces or cleavage surfaces by focused ion beam. Strikingly, deformation twinning was observed as the main feature in three irradiated specimens at high dose. Only twins with $\{112\}$ planes were observed in all of these samples. The average thickness of twins is about 34 nm. Twins started from a fracture surface became gradually thinner with distance away from the fracture surface and stopped in the matrix finally. Features such as twin-precipitates interaction, twin-grain boundary and/or lath boundary interaction were observed. Twinning bands were seen to be arrested by grain boundaries or large precipitates, but could penetrate martensitic lath boundaries. Unlike the case of defect free channels, inside twins small defect-clusters, dislocation loops and dense small helium bubbles were observed.

Key words: ferritic/martensitic steels, spallation irradiation, defect clusters, helium bubbles, embrittlement, micro-cracks, deformation mechanism, defect-free channeling, deformation twinning.

Résumé

Les aciers ferritiques/martensitiques (F/M) sont des matériaux candidats pour des composants structuraux de réacteurs à fusion, les cuves des sources de spallation à métal liquide and les systèmes nucléaires contrôlés par accélérateur, grâce à leur bonne résistance aux irradiations et propriétés thermo-mécaniques. Cependant, la fragilisation de ces aciers résultant des effets combinés des dégâts d'irradiation (mesuré en dpa = displacement per atom) sur la microstructure et de l'accumulation de produits de transmutation, notamment de l'hélium, est un des points critiques.

Quatre aciers différents ont été sélectionnés pour des études mécaniques et microstructurales dans le but de mieux cerner les mécanismes de fragilisation induits par les effets combinés des dégâts d'irradiation et d'hélium, après irradiation dans SINQ, la source de spallation suisse. Les conditions d'irradiation couvrent le domaine: 10.7 - 20.4 dpa avec 850 -1750 appm He entre 160 et 300 °C. L'évolution des propriétés mécaniques après irradiation a été étudiée par des essais de traction et de dureté. Les dégâts d'irradiation et les bulles d'hélium ont été quantifiés par microscopie électronique à transmission (MET). L'accent a été mis sur les mécanismes de déformation sous différents mode de fracture, à savoir ductile, quasi-clivage et intergranulaire, dont l'occurrence dépend des conditions d'irradiation (dpa, contenu d'hélium and température d'irradiation).

Les courbes contrainte-déformation et les images correspondantes de microscopie à balayage des surfaces de fracture ont montré des mécanismes distincts de fracture sous diverses conditions d'irradiations et de tests. Les essais de tractions ont clairement indiqué une augmentation de la limite d'élasticité et une diminution de la ductilité des échantillons irradiés. La dureté a été mesurée sur les échantillons de traction avant les essais de traction. Les résultats de dureté ont démontré une claire augmentation avec la dose d'irradiation and le contenu en hélium dans les échantillons.

Des observations par MET ont été réalisées sur tous les échantillons fracturés dans l'état irradié. Des petits clusters de défauts ont été observés dans l'échantillon à 12.3 dpa, alors que les grands clusters en forme de boucle n'étaient pas nombreux. Dans les échantillons à 17.2, 17.7 and 20.4 dpa, de nombreuses boucles ont été détectées à côté des petits clusters. Le diamètre moyen des clusters de défauts augmente de 4.2 nm à 11.8 nm lorsque la dose augmente de 12.3 dpa à 20.4 dpa, alors que la densité ne change pas significativement. Dans le même temps, le diamètre des bulles d'hélium visibles augmente de 1.03 à 1.93 nm. Les microstructures des zones déformées d'échantillons irradiés ont été observées et des canaux libres de défauts avec des plans plan de glissement$\{110\}$ et $\{112\}$ ont été trouvés dans certains échantillons, indiquant une localisation de la déformation plastique. La largeur moyenne des canaux est de l'ordre de 100 nm.

En ce qui concerne les échantillons fracturés en mode fragile, des échantillons ont été extraits par faisceau d'ions focalisés, soit sous les surfaces de fracture intergranulaire, soit sous les surfaces de clivage. Etonnamment, de la déformation par maclage a été observée dans trois échantillons irradiés à forte dose. Seules des macles sur les planes $\{112\}$ ont été observées dans tous ces échantillons. L'épaisseur moyenne des macles est d'environ 34 nm. Les macles sont initiées près des surfaces de fractures et deviennent plus fines avec la distance et s'arrêtent finalement dans la matrice. Des traits caractéristiques tels que l'intéraction macle-précipité, macle-joint de grains et macle/joint de lattes ont été observés. Des macles ont aussi été observées être arrêtées aux joints de grains, mais pénétrant les joints de lattes. Contrairement aux canaux libres de défauts, de petits clusters et des petites boucles de dislocation ainsi que de denses petites bulles d'hélium résident dans les macles.

La formation de macles est attribuée à l'effet de durcissement extrême d'irradiation induit par les clusters de défauts, des boucles de dislocations aux fortes doses, où le mouvement des dislocations y compris dans des canaux est effectivement bloqué.

Mots-clé: aciers ferritiques/martensitiques, spallation irradiation, clusters de défauts, bulles d'hélium, fragilisation, micro-fissures, mécanismes de déformation, canaux libres de défauts, macles de déformation.

Table of content

Acknowledgments

Abstract

Introduction……..1

1. Literature Review……………………………………………………………………………………………………..5

- 1.1 Radiation damage of metals……………………………………………………………………………………5
  - 1.1.1 Primary damage…………………………………………………………………………………………….5
  - 1.1.2 Radiation-induced microstructure and defect evolution in metals…………………………………6
  - 1.1.3 TEM observation of radiation-induced defects………………………………………………………….8
    - 1.1.3.1 Imaging conditions for observation…………………………………………………………………8
    - 1.1.3.2 Two beam dynamical conditions……………………………………………………………………10
    - 1.1.3.3 Weak-beam dark-field conditions……………………………………………………………………11
- 1.2 Ferritic/Martensitic Steels in nuclear applications………………………………………………………11
- 1.3 Helium effects on the mechanical properties of ferritic/martensitic (F/M) steels………………..14
- 1.4 In-situ SEM investigations on micro-crack behavior……………………………………………………18
- 1.5 Defect-free channeling in deformed metals……………………………………………………………….19
- 1.6 Deformation twinning…………………………………………………………………………………………..26
- 1.7 Objective of this PhD research………………………………………………………………………………33

2. Experimental Methods……………………………………………………………………………………………35

- 2.1 Investigated materials, specimens and irradiation………………………………………………………35
  - 2.1.1 Materials………………………………………………………………………………………………………35
  - 2.1.2 Irradiation conditions of the F/M steels irradiated at SINQ…………………………………………36
  - 2.1.3 Preparation of the tensile specimens for mechanical testing………………………………………..38
- 2.2 Mechanical testing……………………………………………………………………………………………….38
  - 2.2.1 Hardness measurement………………………………………………………………………………………38
  - 2.2.2 Tensile tests…………………………………………………………………………………………………..39
- 2.3 Investigation on the micro-crack initiation and propagation…………………………………………40
  - 2.3.1 Successive small punch testing with SEM observation……………………………………………..40
  - 2.3.2 Successive tensile testing with SEM observation……………………………………………………..41
- 2.4 Microstructure investigation with TEM technique………………………………………………………42
  - 2.4.1 Thickness Measurement……………………………………………………………………………………43

2.4.1.1 Determination of specimen thickness via thickness fringes under WBDF conditions……43

2.4.1.2 Determination of specimen thickness via EELS……43

2.4.2 Data Analysis……44

2.5 TEM-lamella sample preparation with Focused Ion Beam (FIB) technique……45

2.6 Flash electropolishing……49

3. Results……**53**

3.1 Mechanical testing……53

3.1.1 Tensile tests and SEM observations of fracture surface……53

3.1.2 Hardness Measurement……57

3.2 Micro-crack initiation and propagation……58

3.2.1 Successive small punch tests and SEM observations……58

3.2.2 Successive tensile tests and SEM observations……62

3.3 Microstructure Evolution……67

3.3.1 Microstructures of as-irradiated F82H, Eurofer 97, MANET-II……67

3.3.2 Deformed microstructures of as-irradiated F82H and MANET-II……73

3.3.3 Microstructures underneath fracture surfaces of F82H and Eurofer97……76

3.3.3.1 Brittle fracture of Irradiated F82H and Eurofer 97……76

3.3.3.2 Low temperature brittle fracture of unirradiated F82H, ODS-Eurofer 97 and SP T91……84

4. Discussion……**89**

4.1 The dose dependence of defect density and size distribution……89

4.2 Correlation between irradiation defects and hardening (F82H)……91

4.3 Fracture mechanisms of FM steel in different irradiation and test conditions……93

4.4 Deformation microstructure and fracture mechanisms……95

4.4.1 Relationship of defect free channels with deformation and fracture……95

4.4.2 Relationship of defect free channels with deformation and fracture……97

5. Conclusions……**103**

References……**107**

Curriculum vitae……**117**

Introduction

Reduced activation tempered martensitic steels are leading candidate materials for fusion reactor structural components, liquid metal containers of future high power spallation neutron sources and accelerator driven systems (ADS) due to their resistance to void swelling and creep and good balance of physical and mechanical properties, and well-established commercial production and fabrication technologies [1, 2]. Indeed, these steels have high strength up to temperatures around 500 °C, low thermal stresses and good resistance to high dose fission neutron irradiation [3]. Since the materials will be intensively irradiated by energetic neutrons and or other types of particles, a degradation of their overall mechanical properties will occur. For irradiation temperatures below 400-450 °C, irradiation hardening, defined as the increase of the yield stress, occurs and is accompanied with a decrease of ductility and fracture toughness. The degradation of fracture toughness is reflected in an upward shift of the transition temperature between the brittle and ductile fracture modes [4-6]. In a fusion or spallation irradiation environment, structural materials will experience a production of high quantities of transmutation induced impurities (notably helium and hydrogen) besides extensive displacement damage, which may result in additional detrimental effects on the mechanical properties [5, 7]. Helium has a very low solubility in materials. Helium atoms are easily trapped by vacancies, dislocations, grain-boundaries and precipitate-matrix interfaces and develop into bubbles [8-10], which may cause strong embrittlement effect. Hydrogen has a high diffusivity, which leads to desorption at high temperatures [11-13]. In FM steels irradiated in spallation targets, the hydrogen effect is not evident. Therefore, an important issue related to the use of tempered martensitic steels in fusion and spallation devices is embrittlement induced by combined effects of displacement damage and helium accumulation.

Many studies of helium effect have used charged particle irradiation or doping techniques [14-18]. For charged particle irradiation, although the experiment can be flexibly controlled in parameters (dose, dose rate and temperature) and achieve a high irradiation dose and a high He concentration in a very short time period, the limited implantation depth and the high dose rate make it difficult to directly simulate bulk properties and the real irradiation environment [17]. Doping technique in fission irradiation, with either nickel or boron isotopes, allows producing helium in bulk specimens via transmutation reactions with thermal neutrons [15]. However, the clear demonstration of a specific helium effect is difficult, because of a number of artefacts induced by the doping (modifications of transformation temperatures by nickel, formation of nickel rich precipitates during irradiation, boron segregation to grain boundaries and formation of lithium as well as helium etc.). Due to the cons of helium implantation and doping techniques, using spallation irradiation is an excellent opportunity to study the combined effect of helium and displacement damage.

Compared with neutron irradiation, ferritic/martensitic (F/M) steels in spallation irradiation exhibit a strong increase of ductile-brittle transition temperature (DBTT) based on the results obtained at Paul Scherrer Institut (PSI), which is partially attributed to helium effect [6, 7]. However, the fundamental mechanism is still not well understood. In addition, while it has been well established that F/M steels are relatively immune to the so called ‘high temperature helium embrittlement’ phenomenon in fusion materials research [19, 20], helium effects at low temperatures (<400 °C) are still fully understood.

In irradiated materials, dislocation channeling has been generally observed in both pure metals and alloys by many researchers [21, 22], which is suspected to lead to intergranular cracking as an intrinsic embrittlement cause [23, 24]. For unirradiated materials, brittle fracture is usually related to various possible reasons such as dislocation pile-ups nearby grain-boundaries or the intersection of mechanical twinning inducing micro-crack. No matter which cases induced brittle fracture, the deformation mechanism is essential to be understood. Up to now, the deformation microstructures of irradiated F/M steels are still very limited studied.

The availability of tensile test and hardness measurement machines and electron microscopy facilities including focused ion beam and transmission electron microscopy for radioactive materials at PSI allows a comprehensive study of relationships among radiation-induced microstructures and change of mechanical properties of highly activated specimens. The specimens irradiated in the SINQ Target Irradiation Program (STIP) provide an excellent opportunity to study the embrittlement induced by the combined effects of displacement damage and helium. In this work our goal is to study some of the issues mentioned above by conducting mechanical tests and microstructural observations on different F/M steels irradiated in the second experiment of STIP (STIP-II).

1. Literature Review

1.1 Radiation damage in metals

1.1.1 Primary damage

There are three types of interactions between irradiating particle with a target material, which contribute to the energy loss of the incident high energy particle [25]:

1) Elastic interaction between the particle and the target material atoms,
2) Inelastic interaction between the particle and the electrons of the solid, and
3) Inelastic interaction between the particle and the nuclei of the target.

As consequence of these interactions, three types of defects are introduced: i) the displacement of original atoms from their lattice sites leads to the formation of vacancy-interstitial pairs (Frenkel pairs); ii) the excitation of electrons and iii) the introduction of foreign atoms, either by nuclear transmutations or by the projectile ions stopping in the solid. In general, all electronic excitations do not result in radiation damage effects due to the quick thermalization in metallic materials. Hence, the first and third types of damage are contemplated as the principal interest for the damage occurring in metallic materials.

For the first type of damage, how the incident high energy particle bombarding the lattice causing the formation of defect clusters can be described as follow [25, 26]: Firstly, a primary knock-on atom (PKA) with a recoil energy T is created within less than 1 fs (10^{-15} s). The minimum material-dependent threshold energy (T_d) needed for an atomic-displacement is between 10 eV and 50 eV for metals [27]. In the following, a collision cascade is produced as a result of the slowing down of the PKA within a very short period of time about ~0.2 ps (10^{-12} s). The collisional stage ends with significant amounts of lattice atoms being displaced from their normal sites. The energy stored in the cascade region is then released in ~3 ps to form a thermal spike core, which is a very hot (several times T_m, T_m being melting point temperature [28]) but less dense zone. A vacancy-rich depleted zone and an interstitial shell around the depleted zone are created when the spike core is cooled down within another ~7 ps. The cool down phase lasts up to 100 ps [29]. The cascade volume increases with increasing T below 10 keV, while cascades are inclined to break up into sub-cascades above 10 keV [30]. The molten material cools down and approaches the surrounding environment temperature in few tens of picoseconds. Subsequently, most (70-90%, temperature dependent) of interstitials and vacancies annihilate by thermal intracascade recombination. The surviving vacancies and interstitials agglomerate to form dislocation loops or annihilate at other existing defects such as GBs and dislocation lines, or move as free point defects.

In addition to the stated elastic collision, inelastic collisions between the incident particles and the bombarded atom may lead to nuclear transmutation products such as helium and hydrogen in gaseous state within a few femtoseconds, when the energy of the impinging particle is higher than a given threshold energy.

1.1.2 Radiation-induced microstructure and defect evolution in metals

The types of defect structure created by irradiation in crystalline lattice can be given in the following:

i) Point defects (0D): vacancies and interstitials

ii) Line defects (1D): dislocation line

iii) Planar defects (2D): dislocation loops

iv) Volume defects (3D): cavities, stacking fault tetrahedral (SFTs), precipitates

The vacancy is a missing atom in the lattice and it is the simplest point defect in any crystalline lattice, while an interstitial is an extra atom that is located in a position of a crystal that is not a regular lattice site. Multiple vacancies (cluster up to 4 vacancies), with a binding energy of about 0.62 eV [31] are smaller compared to interstitial clusters and often observed in irradiated metals. Self-interstitials atoms (SIAs) have a high formation energy (>2.0 eV) and a low migration energy (>0.15 eV) resulting in a high mobility, on the other hand, vacancies have a low formation energy (<2 eV) and high migration energy (>0.5 eV) and therefore they are much less mobile than SIAs. An agglomeration of SIAs to form SIA cluster can occur at elevated temperatures. Once these multiple SIAs form, they are very stable against dissociation at low temperatures [32].

The experimental conditions have significant influence on irradiated microstructure. The irradiation dose and temperature are the two main concerns as discussed below.

The calculated damage level is directly proportional to the product of the fluence and the average kinetic energy transferred to the host lattice atoms (damage energy). The efficiency of radiation can be characterized by cross section, which depends on the type of energetic particles. For instance, the effective damage cross-sections for 1 MeV particles incident on copper range from ~ 30 barns (1 barn=1×10^{-24} cm^2) for electrons to ~ 600 barns for neutrons and ~ 2×10^9 barns for Cu ions [33]. The displacement per atom (dpa) unit as the most important parameter for quantifying radiation effects in materials is remarkably effective in correlative the initial damage production levels over a wide range of materials and irradiating particles. In general, numerous aspects of microstructural evolution are qualitatively equivalent on a dpa basis for materials irradiated in widely different irradiation environments. The accumulated damage, as the form of dislocation loops or other microstructural features, typically exhibits a complex nonlinear relationship with irradiation dose that depends on irradiation temperature and several other factors. Besides, the dpa unit does not precisely characterize some of the complicated differences in primary damage production for energetic displacement cascade conditions compared to isolated Frenkel pair production [34]. For instance, defect production at cryogenic temperatures (where long-range defect migration and annihilation does not occur) for neutron and heavy ion-irradiated materials is about 20-30% of the calculated dpa value because of athermal in-cascade recombination processes [34, 35].

Irradiation temperature typically has a strong influence on the microstructural evolution of irradiated materials. There are several major temperature regimes delineated by the onset of migration of point defects. As an example, figure 1.1 shows the five major defect recovery stages for copper irradiated with electrons at 4 K [36]. Stage I corresponds to the onset of long-range SIA migration. Stage II involves migration of small SIA clusters and SIA-impurity complexes. Stage III corresponds to the onset of vacancy motion. Stage IV involves migration of vacancy-impurity clusters, and Stage V corresponds to thermal dissociation of sessile vacancy clusters.

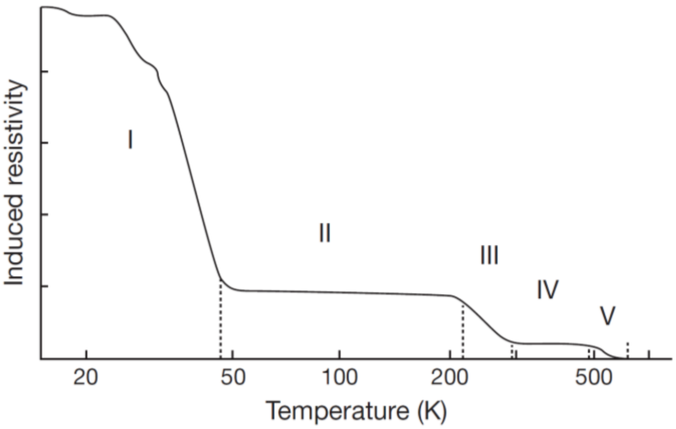

Fig 1.1: Electrical resistivity defect recovery stages for copper following electron irradiation at 4 K [36].

In the following, summaries are given on the experimental microstructural observations for five key irradiation temperature regimes. At very low temperatures, defect accumulation is generally proportional to dose until defects created in displacement events reaches the level to overlap and annihilate preexisting defects. Defect clusters resolvable by TEM are usually not visible in this irradiation temperature regime due to the lack of defect mobility [37]. Between recovery Stage I and Stage III, the SIA point defects and small SIA clusters have sufficient mobility to migrate and produce visible dislocation loops as well as agglomerate with sessile monovacancies and vacancy clusters. In this temperature regime, the defect accumulation is initially linear with dose, followed by a square root dependence at an intermediate dose in pure materials. The critical dose for this kinetic transition is dependent on the concentration of other defect sinks in the lattice (dislocations, grain boundaries, precipitates, etc.) [38-41]. At temperatures where both SIAs and vacancies are mobile, the predominant visible features in this temperature regime are vacancy and interstitial loops and SFTs for irradiated fcc materials and vacancy and interstitial loops and voids for irradiated bcc materials. The loop density and nature in bcc metals is strongly dependent on impurity content in this temperature regime [42-44]. The individual loops within the raft aggregations exhibited the same Burgers vector in neutron irradiated Fe. Submicroscopic cavities with cavity densities that are about two orders of magnitude higher than the visible loop densities can be measured by Positron annihilation spectroscopy analyses in the irradiated bcc metals [45-48]. The typical microstructural features that appear during irradiation at temperatures above recovery Stage V include dislocation loops (vacancy and interstitial type), network dislocations, and cavities. A diversity of precipitates may also be formed in irradiated alloys [49-52]. At high irradiation dose, a moderate density of network dislocations is created due to loop unfaulting and coalescence. Compared with lower temperature irradiation, significant levels of cavity swelling are observed in the temperature regime above Stage V. Above 0.5 T_M, there is minor microstructural changes because of thermodynamic equilibrium processes unless a great number of impurity atoms such as helium are introduced by nuclear transmutation reactions or by accelerator implantation [33].

1.1.3 TEM observation of radiation-induced defects

In the following paragraphs, we shortly describe the origin of the contrast in TEM observations that allows identifying the irradiation-induced defects.

1.1.3.1 Imaging conditions for observation

Phase Contrast

The specimen introduces local changes in the phase of the electron wave. These local phase variations are converted into amplitude variation via the Scherzer phase shift produced by the microscope over which the operator has control by defocusing, e.g. the imaging of voids in out-of-focus conditions. An important sub-area of phase contrast imaging is high-resolution structural imaging. Under some conditions, the resulting image may show resolution on a scale close to the atomic level. Generally, however, if the image is to resemble the projected charge density of the specimen, several stringent imaging conditions must be met. Unlike diffraction contrast images, high-resolution 'structural' are obtained by allowing several diffracted beams to contribute to the image. Usually, the specimens is tilted to a low-index 'zone-axis' orientation and a large objective aperture objective aperture is used to select a number of beams to form the image [53].

Z contrast

The scattering of the electron wave by atoms is proportional to their atomic mass, or Z, the atomic number. The intensity at large scattering angles becomes higher with the increase of the atomic number. Allowing incoherent imaging of materials represents a new approach to high-resolution electron microscopy. The Z-contrast high-resolution transmission electron microscopy technique provides directly interpretable images-maps of scattering power of the specimen. There are no phases in a Z-contrast incoherent image, therefore, no phase problem for structure determination. Location of atom column positions in an image is simplified. In addition, the resolution is higher than in a coherent image, the information is highly localized, the intensity of atom columns directly reflects their mean square atomic number (Z), and there are no contrast reversals with crystal contrast image is obtained by scanning an electron probe of atomic dimensions across the specimen and collecting electrons scattered to high angles. The resolution of the technique is determined by the size of the electron probe [53].

Diffraction contrast

When passing through a crystal lattice, electrons diffract on the atomic planes according to Bragg's law:

$$n\lambda=2d\sin\theta \tag{1.1}$$

Where n is an integer, λ is the wavelength of the incident beam, d is the distance between the atomic planes and θ is the angle between the incident beam and the scattering planes. In the resulting diffraction pattern the reciprocal lattice vector $\vec{g}$ relating the transmitted and diffracted spots, as shown in figure 1.2, is referred as the diffraction vector, its magnitude $g=1/d$. The reciprocal lattice vector g corresponds to the diffraction vector from (000) to (h k l) spot in the diffraction pattern. The radius of Ewald sphere k ($k=1/\lambda$) is much bigger than g. The diffraction condition is often specified by the deviation vector $\mathbf{S_g}$**,** which is the measure of deviation from the exact Bragg condition. The diffraction condition is specified by ‘ng(mg)’, where ng is the beam selected to form the image and mg is the beam intersecting with the Ewald sphere. The deviation vector is then given geometrically by $\mathbf{S_g} = n(n-m)g^2\lambda/2$.

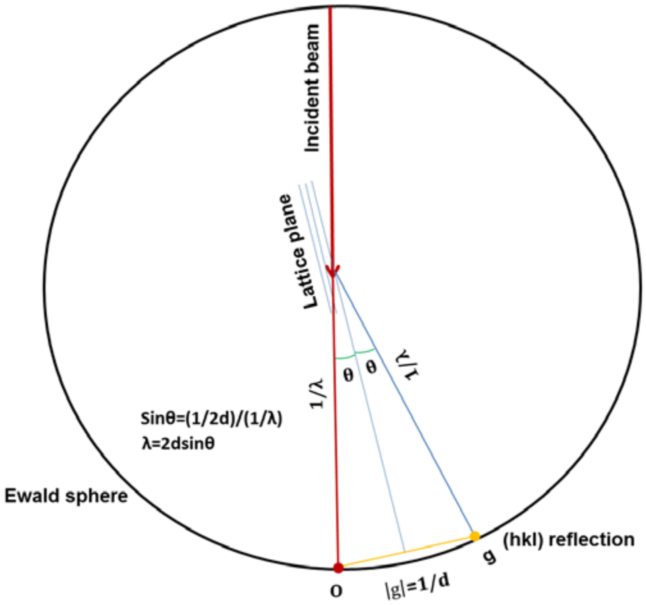

Fig 1.2: Schematic of basic principle of Bragg diffraction condition and Ewald sphere.

In the microscope, as shown in Fig. 1.3, the objective aperture allows forming an image by selecting only the transmitted beam (bright field mode) or one of the diffracted beams (dark field mode). The resulting contrast is named diffraction contrast. In diffraction contrast, defects are imaged by virtue of their elastic strain fields. The crystal is set at some well-defined diffracting condition, and an objective aperture is used to form an image using one of the diffracted beams. The defect strain field causes local changes in diffraction conditions: for instance, the diffracted planes may be locally bent, causing changes in the amplitude of the diffracted beam used to form the image. This is the most common mechanism used in radiation-damage studies. The image characteristics depend sensitively on the chosen diffraction conditions [54].

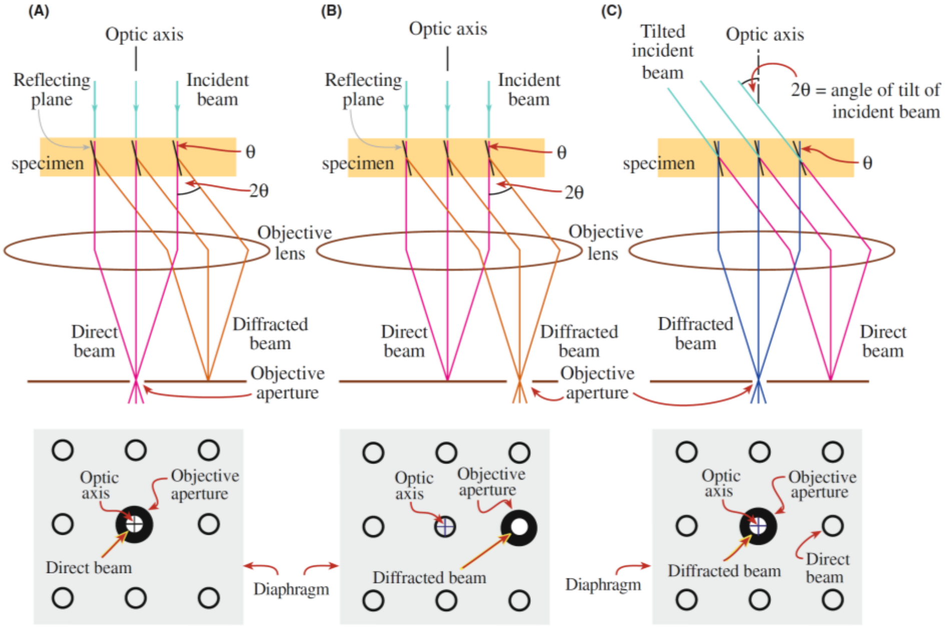
(A)
Optic axis
Reflecting plane
Incident beam
specimen
θ
2θ
Objective lens
Direct beam
Diffracted beam
Objective aperture
Optic axis
Objective aperture
Direct beam
Diaphragm
(B)
Optic axis
Reflecting plane
Incident beam
specimen
θ
2θ
Objective lens
Direct beam
Diffracted beam
Objective aperture
Optic axis
Objective aperture
Diffracted beam
Diaphragm
(C)
Tilted incident beam
Optic axis
2θ = angle of tilt of incident beam
specimen
θ
Diffracted beam
Direct beam
Optic axis
Objective aperture
Diffracted beam
Direct beam

Fig 1.3: Diagram for transmitted beam and diffracted beam [54].

The imaging of small point-defect clusters shall mostly be concerned. ‘Small’ in this context is in relation to the extinction distance ξg, which plays a critical role in the description of electron diffraction phenomena. The value of ξg depends on the materials, the excited reflection g, and the microscope operating voltage, but is typically several tens of nanometers. The effective extinction distance is given by [55].

$$\xi_g^{eff} = \frac{\xi_g}{\sqrt{1+\omega^2}} = \frac{\xi_g}{\sqrt{1+\xi_g^2 \bullet s_g^2}} \qquad (1.2)$$

where **ω** is ξg·S_g and $\mathbf{S_g}$ is deviation vector.

1.1.3.2 Two beam dynamical conditions

The TEM specimen is at or close to Bragg condition in the two-beam dynamical condition, where the spots size of transmitted and 1g diffraction beam are nearly same and the intensity is equally distributed between transmitted and 1g diffracted beam. The deviation vector $\mathbf{S_g}$ is therefore zero or very small under dynamical two-beam conditions. Under strong two-beam conditions, there is a strong dynamical interaction between the two beams, and the resulting image characteristic may be quite complicated. Image peak widths are generally rather broad, about $\frac{1}{3}$ξg for a line dislocation. Dislocation loops smaller than ξg will not be resolved directly, in the sense that their images will not be ‘loop-like’ but will be more complex. Therefore, it is not straightforward to study line dislocations and their interactions. However, the contrast features of small defect clusters and helium bubbles under strong two-beam conditions can be exploited usefully. Particularly, for the characterization of tiny helium bubbles (1-2 nm), the 'two-beam' conditions together with over-focused or de-focused technique were employed to take images [53].

Usually, bright-field kinematical conditions are used when it is desired to avoid the dynamical contrast effects seen in strong two-beam images. A two-beam condition is set up with a small positive deviation parameter ($\mathbf{S_g}>0$).

1.1.3.3 Weak-beam dark-field conditions

As the name implies, weak-beam images are dark-field images obtained using a weakly-excited beam. The foil is tilted so that in regions far away from dislocations or other defects, the diffraction planes are well away from the Bragg condition with large magnitude of deviation parameter$|\mathbf{Sg}|$. The contrast under weak-beam conditions arises from regions of large lattice strain close to the cores of defects. Since the foil is tilted well away from the Bragg condition the average image intensity is very low. The value of the deviation parameter $|\mathbf{Sg}| \geq 2 \times 10^{-1}$ nm^{-1}, this condition gives rise to a narrow (<2 nm), high-contrast image peak located close to the dislocation core. Besides, the narrow image peaks obtained in weak-beam microscopy are a consequence of the small value of the effective extinction length ξ_g^{eff}. With $\mathbf{S_g} = 2 \times 10^{-1}$ nm^{-1}, $\xi_g^{\mathrm{eff}} \approx 5$ nm, giving dislocation peak widths of about $\frac{1}{3}\xi_g^{\mathrm{eff}} \approx 2$ nm. Because of these small dislocation peak widths, weak-beam microscopy has been particularly successful in characterizing dislocation microstructures, including the complex dislocation microstructures frequently produced by irradiation [53]. In our present work, weak-beam dark-field conditions at z=111, (g, 5g) =110 were exploited to investigate irradiation-induced small defect clusters and dislocation loops in irradiated F82H.

1.2 Ferritic/Martensitic Steels in nuclear applications

Before 1970s, austenitic stainless steels were applied as primary material for fast reactor structures and fuel cladding. Then the 9-12% Cr-Mo steels with higher thermal conductivities and lower expansion coefficients were considered better than austenitic stainless steels for in-core applications (cladding, wrappers, and ducts) in fast reactors. Besides, these steels have excellent irradiation resistance to void swelling compared to austenitic stainless steels. Sandvik HT9 steel was the selected as candidate in the US fast reactor program. EM-12, FV448, DIN 1.4914, and JFMS as similar steels to HT9 with maximum operating temperature of ~ 550 °C were chosen in France, United Kingdom, Germany, and Japan, respectively. In Fusion reactor studies community, HT9, EM-12, FV448, DIN 1.4914, and JFMS are firstly considered in US, Europe and Japan Fusion Materials Programs [3].

In the mid-1980s, the concept of low-activation materials was applied in the international fusion programs [1, 56-62]. The objective was to facilitate the maintenance operations by reducing the activity level of reactors, and to limit the residual radioactivity to gain and improve public acceptance towards fusion energy [56, 57]. Fusion reactor materials research programs in Japan, Europe and the United States began to develop reduced-activation ferritic/martensitic steels in the mid-1980s and early 1990s [57-59]. Based on nuclear calculations, the typical steel alloying elements Mo, Nb, Ni, Cu, and N had to be suppressed or minimized, and the development of reduced-activation ferritic/martensitic steels replaced molybdenum in conventional Cr-Mo steels by tungsten and /or vanadium [1, 60-63] and substitute niobium by tantalum [59]. Steels with 7-9% Cr and less carbon or manganese for austenite stabilization were favored over those with 12% Cr steel where embrittlement can be caused by lower toughness induced by delta-ferrite and increasing chi-phase precipitation during irradiation promoted by manganese [63]. Eventually, 7-9% Cr steels were selected for further study and development. F82H with compositions of Fe-7.5Cr-2.0W-0.2V-0.04Ta-0.10C was chosen in the Japanese program and was investigated as part of the IEA (International Energy Agency) Implementing Agreement on Fusion Materials. Eurofer97 with compositions of Fe-8.5Cr-1.0W-0.05Mn-0.25V-0.08Ta-0.05N-0.005B-0.10C was the selection of the development program in Europe. ORNL 9Cr-2WVTa steel with compositions of Fe-9Cr-2W-0.25V-0.07Ta-0.10C was considered as the steel with the best properties in the US.

For the Cr-Mo and Cr-W elevated-temperature steels with about 5-12% Cr, martensite (body-centered-tetragonal structure) is produced by quenching. As quenched, a high number density of dislocations is contained in 7-12% Cr steels. Quenched steel is then tempered to improve toughness and ductility. During tempering, $M_{23}C_6$ (M is primarily Cr, Fe, and Mo) and MX (M is primarily vanadium and niobium, and X is carbon and nitrogen) precipitate, leading to a ferrite matrix with the large (60-200 nm) $M_{23}C_6$ particles on lath and prior-austenite grain boundaries and smaller (20-80 nm) MX particles in the matrix. In addition, normalizing lowers the high number density of dislocations in the untempered martensite.

After high-energy neutron irradiation in a fast reactor, the obvious changes of microstructure involves the formation of dislocation loops, swelling and irradiation-induced segregation as well as precipitation. Below 400-450 °C, loop size increases and number density decreases with increasing temperature. Loops develop into a dislocation network with increasing temperature [50, 64-66]. Above 400-450 °C, more rapid diffusion allows the irradiation-induced defects to anneal out and precipitates to coarsen. Agglomeration of vacancies can cause void swelling up to about 500 °C. The low-swelling property of 5-9% Cr ferritic/martensitic steels has been validated in irradiations of modified 9Cr-1Mo (T91) and HT9 in the Fast Flux Test Facility (FFTF) and the Experimental Breeder Reactor (EBR-II) [65, 67]. Irradiation in EBR-II and FFTF to over 200 dpa at 400-420 °C, which is near the maximum swelling temperature for the steels, produced swelling of <2% in FFTF and <3% for irradiation in EBR-II. Swelling can be accelerated by high stress levels which was found in irradiation creep studies [67]. For most of the 9-12% Cr steels investigated, Laves phase, which forms during thermal aging and irradiation at ~ 400-600 °C during high-energy neutron irradiation, can cause embrittlement.

Transmutation reactions of neutrons can produce new atom and gas helium or hydrogen. This effect is significantly important for the fusion reactors. The helium to dpa ratio for ferritic/martensitic steels in a fusion reactor is about two orders-of magnitude higher than in most fission reactors. Nevertheless, just little helium is produced by fast neutrons in FM steels.

In Spallation Neutron Sources irradiation, at irradiation temperature above 175 °C, high-density helium bubbles of about 1 nm diameter appeared. The microstructure changes of bubbles were observed within increasing irradiation temperature: the size of bubbles increases and the density slightly decreases. However, for defect clusters, there is almost no change in size at temperatures below 235 °C and thereafter rapidly increase at higher temperatures, while there is no obvious change in number density up to 255 °C but then rapidly decreasing above this temperature. The $M_{23}C_6$ precipitation was amorphized at the irradiation temperature below about 235 °C, which corresponds to about 0.3 T_m (T_m is the absolute melting temperature) of the steel [68, 69]. The bubble size increased up to 50 nm in the F82H specimen irradiated to 20.3 dpa/1800 appm He at 400(±50) °C [8].

In fast neutron reactors, the tensile behavior of irradiated 5-12% Cr ferritic/martensitic steels depends significantly on irradiation temperature [70-74]. It was observed that the increase of yield stress (hardening) and the loss of ductility were caused by the irradiation-induced microstructural changes in modified 9Cr-1Mo and HT9 [71, 72] irradiated to 9-12 dpa at 390 °C. However, no change in the amount of hardening was essentially observed when the steels were irradiated at 390 °C to 23 dpa, which indicates that hardening saturated with increasing fluence [73]. Saturation occurs by 10 dpa for irradiation at around 400 °C [73], but higher fluences are demanded at lower temperatures [74]. Mechanical properties are generally unchanged compared to unirradiated and the thermally aged samples after irradiation at 425-450 °C. An increase in the ductile-brittle transition temperature (DBTT) and a decrease in upper-shelf energy (USE) were found by qualitative observation on effect of irradiation hardening on toughness in a Charpy curve to higher temperatures [4, 5, 75, 76]. The increase in DBTT (ΔDBTT) of HT9 saturates with fluence just like the yield stress saturates and the magnitude of the shift varies inversely with irradiation temperature alike as the variation in hardening after irradiation in FFTF at 365 °C.

In spallation neutron sources irradiation, ΔDBTT of FM steels shifts to higher temperature observed in both small punch and Charpy impact tests. In small punch test [77], it was found that the DBTT increases with increasing irradiation dose in F82H, T91 and Optimax-A irradiated in SINQ Target up to 9.4 dpa at the temperatures between 90 °C and 275 °C and has more quickly increasing above ~6-7 dpa. In addition, ΔDBTT increases linearly with the helium contents. In Charpy impact test [6], the DBTT increasing with irradiation dose was also observed in four different FM steels (T91, F82H, Optifer-V and Optimax-A and –C) irradiated in SINQ Target up to 7.5 dpa at the temperatures between 120 °C and 195 °C. The tensile test results indicate that the irradiation hardening increases with dose and the uniform elongation decreases to less than 1% as well as the embrittlement effect is significant, however, the total elongation still can be maintained larger than 5% for four different FM steels (T91, F82H, Optimax-A and EBW F82H) irradiated in SINQ Target below 10 dpa [78]. Besides, Henry et al [79] found there was a change in fracture behavior at doses > 16 dpa for T91 and EM10 in tensile test. The specimen exhibits brittle fracture and some fractured in the elastic regime at high dose, whereas the lower dose samples are ductile. Moreover, the annealing effect with ductility recovery of some specimens at 11-12 dpa was occasionally observed, which was attributed to the short period of high temperature excursion during irradiation [78, 80]. On the other hand, T91 and EM10 specimens irradiated to 20 dpa exhibit a recovery of ductility but still increased strength compared to unirradiated samples after annealing [79]. FM steels irradiated in high-energy protons and spallation neutrons environment (STIP) show more severe embrittlement effect compared to fission neutron irradiations as seen in Fig.1.4 [81]. The colorful symbols represent results from Spallation irradiation, while the black symbols represent results from fission neutron irradiation. The figure indicates the saturation phenomenon of ΔDBTT of FM steels irradiated in fission neutron irradiation and the ΔDBTT of FM steels irradiated in Spallation irradiation is much higher than that of neutron irradiated steels above 10 dpa.

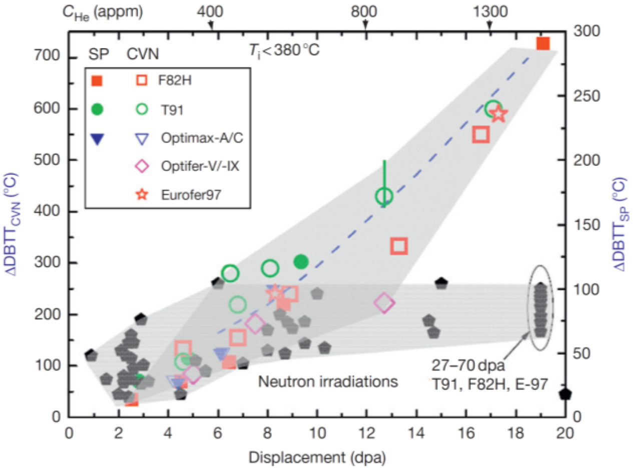

Fig 1.4: DBTT shift as a function of irradiation dose for different FMS irradiated in STIP. Neutron-irradiation data are included for comparison [81].

1.3 Helium effects on the mechanical properties of ferritic/martensitic (F/M) steels

With the development of fusion energy, the study of irradiation effects on structural materials for fusion applications has increased importantly in recent years. However, due to the lack of an intense source of 14 MeV neutrons, such those that will be present in any fusion facility and producing large amounts of transmutation helium, we need to use other methods to simulate the irradiation effects of these 14 MeV neutrons. The main simulation experiment methods include ion implantation, nickel or boron doping with fission neutrons and spallation neutron source irradiation.

P. Jung et al. [16] made research on T91 samples implanted with He_4 to concentrations up to 0.5 at.% at temperatures from 150-550 °C by α-particle beam of energy 28 MeV. From their tensile test results in Fig 1.5, we could observe that the effects of implantation are much more pronounced at 250 °C than at 550 °C.

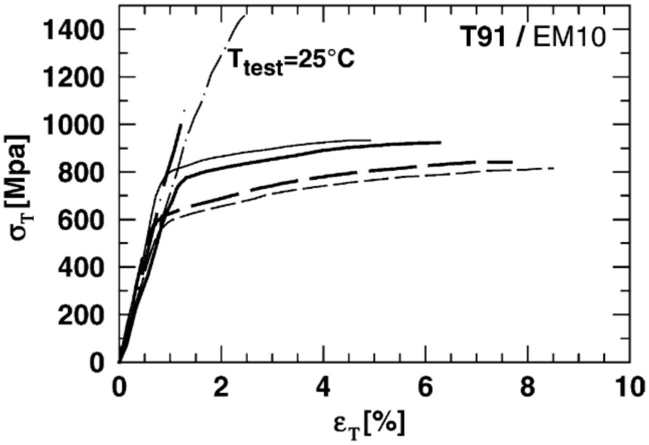

Fig 1.5: Comparison of true tensile curves at 25 °C and strain rates of 8.5×10^{-5}/s for T91 (bold lines) and EM10 after implantation of 0.5 at.% He (0.8 dpa) at 250 °C (dash-dotted) and 550 ℃ (solid), respectively. Unimplanted controls (dashed) are given for comparison [16].

From the fracture surface in Figure 1.6, they also found that implantation at 250 °C induces fracture without necking, while some necking and ductile appearance is retained at 550 °C

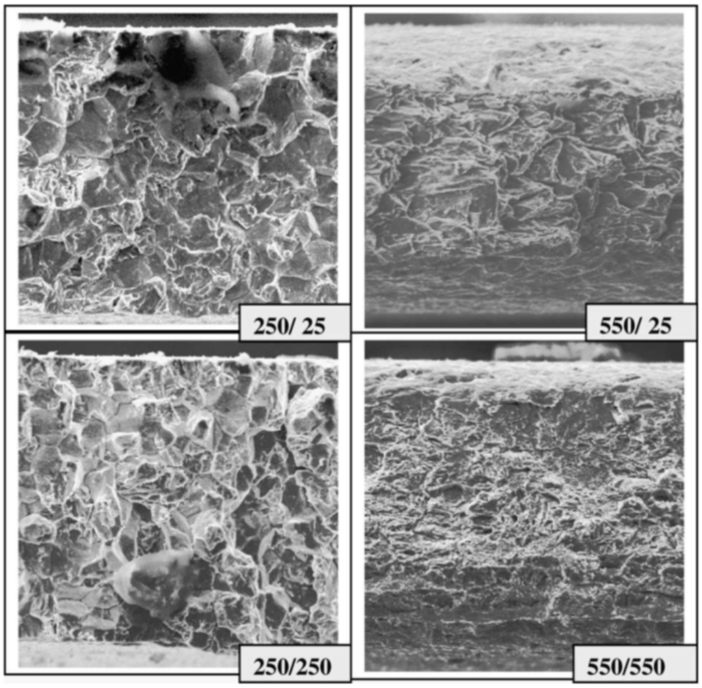

Fig 1.6: Fracture surfaces of 100 µm thick T91 specimens after implantation at 250 and 550 °C, tested at 25 °C and implantation temperature, respectively [16].

H. Ullmaier et al. [17] made research on 316L specimens implanted with He_4 to concentrations up to 1 at.% at 25 °C by α-particle beam of energy 28 MeV. The samples harden rapidly with irradiation. They observed that the strength decreases with the increase of testing temperature, while the total elongation decrease with the increase of helium content. They also found the hardening is dominated by dpa as long as the helium concentration does not exceed 0.5 at.%. However, for He contents of around 1 at.% an additional hardening/embrittlement was observed. A. Hasegawa et al. [18] investigated the effect of helium concentration and annealing time on the property of 316FR at 750 °C and related phenomena such as the microstructural change and helium desorption behavior to clarify the helium embrittlement mechanism in the 316FR steel at high temperature by using 50 MeV α particle beam of the cyclotron accelerator of Tohoku University. The thickness of the samples was 300±20 µm. Fully transgranular fracture was observed in the unimplanted specimens regardless of the annealing time, on the other hand, the helium-implanted specimens showed fully intergranular fracture regardless of the helium concentration and the annealing time. Threshold helium concentration for the helium embrittlement in the 316FR steel was considered to be below 5 appm.

In other investigations, the helium production results from thermal neutron induced reactions such as:

$$\begin{aligned} &{}^{58}_{28}Ni + {}^{1}_{0}n^{th} \rightarrow {}^{59}_{28}Ni + \gamma \\ &{}^{59}_{28}Ni + {}^{1}_{0}n^{th} \rightarrow {}^{56}_{26}Fe + {}^{4}_{2}He \ (4.76\ MeV) \\ &{}^{10}_{5}B + {}^{1}_{0}n^{th} \rightarrow {}^{7}_{3}Li + {}^{4}_{2}He \ (1.47\ MeV) \end{aligned} \tag{1.3}$$

So far, some researchers have simulated helium embrittlement based on the Ni or B doping technology to simulate helium embrittlement. K. Shiba et al [82] made research on the F82H and ^{10}B-doping F82H specimens which were irradiated at lower temperatures (260-360 °C to 0.3-0.6 dpa in JMTR (Japan Materials Test Reactor). They observed that the DBTT of ^{10}B-dope F82H appeared to be well above room temperature and much larger than that for the standard F82H irradiated similarly, i.e. 230-320 °C and 0.2-0.5 dpa vs 260-360 °C and 0.3-0.6 dpa. E. Wakai et al [15] indicates that the shift of DBTT in the radiation-hardened specimens increases with increasing helium production by comparing F82H +11B, F82H+10B and F82H+10B+11B specimens irradiated at 250 °C in JMTR to 2.4 dpa. He gave a model to explain the shift of DBTT in Figure 1.7. The fracture stress 1 is shown to be constant during irradiation without helium production and fracture stress 2 is shown to be changed by the helium production during irradiation. T_i and T_{ii} are identified as DBTT before and after irradiation without helium production. T_{iii} and T_{iv} are identified as DBTT after irradiation with a synergistic effect of displacement damage and helium production under fracture stress 1 and 2.

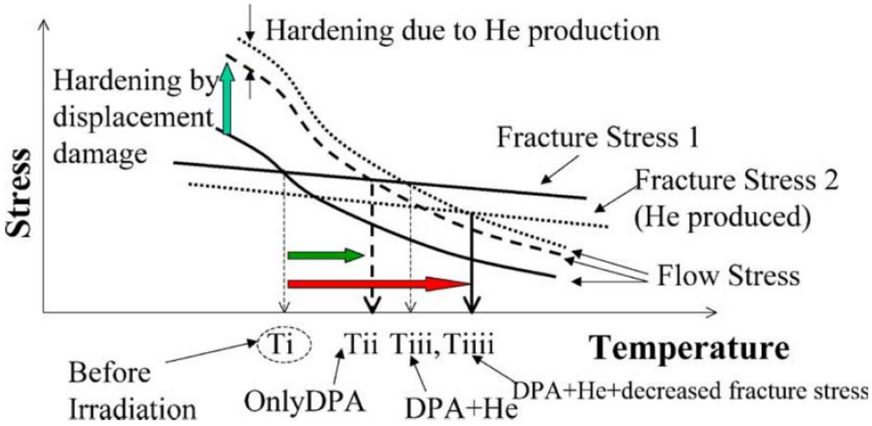
Hardening due to He production
Hardening by displacement damage
Stress
Fracture Stress 1
Fracture Stress 2 (He produced)
Flow Stress
Temperature
Ti
Tii
Tiii, Tiiii
Before Irradiation
OnlyDPA
DPA+He
DPA+He+decreased fracture stress

Fig 1.7: Explanation of ΔDBTT due to He production [15].

The shift of DBTT due to helium production at higher irradiation temperature will be smaller than that at lower irradiation temperature under the fracture stress 2.

Since the He production rate in steels under the irradiation in spallation targets is very high, understanding the respective behavior of austenitic stainless steels and FM steels in such irradiation environments is an important materials issue for developing high-power liquid metal spallation targets, accelerator driven systems (ADS) and fusion reactor in the future. Several mixed proton and neutron irradiation facilities such as SINQ and LANSCE in Los Alamos (USA) have been used to investigate irradiated materials behavior. Jia et al. [77] conducted small punch tests in the temperature range from -190 to 80 °C on martensitic/ferritic steels F82H, T91 and Optimax-A irradiated in SINQ Target-3 up to 9.4 dpa in the irradiation temperature range of 90–275 °C. The dose dependence of the ductile to brittle transition temperature shift $\Delta DBTT_{sp}$ for three FM steels shows that at lower irradiation doses, the $\Delta DBTT_{sp}$ increases linearly with increasing dose, but at irradiation dose higher than about 6–7 dpa with helium concentrations above about 400 appm, there is a substantial increase of $\Delta DBTT_{sp}$. The results also show that the $\Delta DBTT_{sp}$ increases linearly with helium concentration of the specimens. Compared with neutron irradiation where the ΔDBTT increasing tends to saturate at a dose level of about 3–5 dpa, the ΔDBTT does not saturate in the case of high-energy proton irradiation. In addition, it increases more rapidly at the higher dose level of 6–7 dpa. The additional increase of $\Delta DBTT_{sp}$, may indicate that helium does not only contribute to the hardening commensurate with the additional shift in the ΔDBTT but also weakens the grain- and lath-boundaries in reducing the fracture stress. Dai et al. [7, 83] compared the data of DBTT-shift obtained from the T91 and EM10 and other steels irradiated in STIP with some data of T91 and Eurofer-97 steels after neutron irradiation [75, 84-87]. They found that: (1) the DBTT-shift of all the steels irradiated in STIP shows a similar trend of DBTT shift versus irradiation dose, and (2) the DBTT-shift of the steels irradiated in STIP is much higher than that of neutron irradiated steels and the difference increases with irradiation dose, which is attributed to the He-induced embrittlement effects.

1.4 In-situ SEM investigations on micro-crack behavior

In-situ SEM and small punch tests have been used to study crack initiation and propagation by several groups. YU et al [88] used small punch test to evaluate stress corrosion cracking (SCC) susceptibility of high-strength steel. The surfaces of several specimens obtained after unloading at different deformation levels (see Fig 1.8) were observed in a SEM, as shown in Fig 1.9. They observed microcracks formed at different deformation levels in different environments (air and synthetic sea water).

Isselin et al [89] studied crack initiation resistance characterization of weld in boiling water reactor environment by small punch test. They concluded that 1) there were two mechanisms of initiation: initiation at slip lines and initiation at inclusions. 2) the crack length distribution has been fitted with the Poisson distribution. The heat affected zone (HAZ) presented the highest number of crack initiation. 3) the HAZ specimen surface had some deformation irregularity at the micro scale enhancing the initiation of microcrack groups.

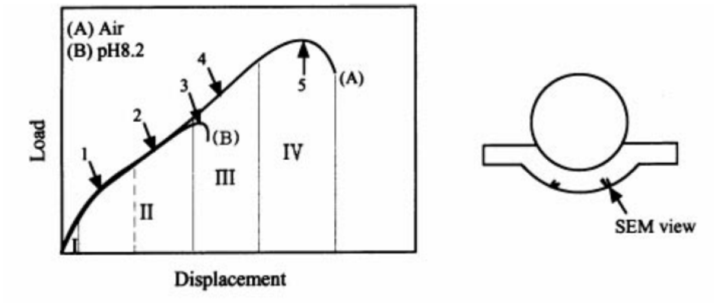

Fig 1.8: Unloading points on the load-displacement curve [88].

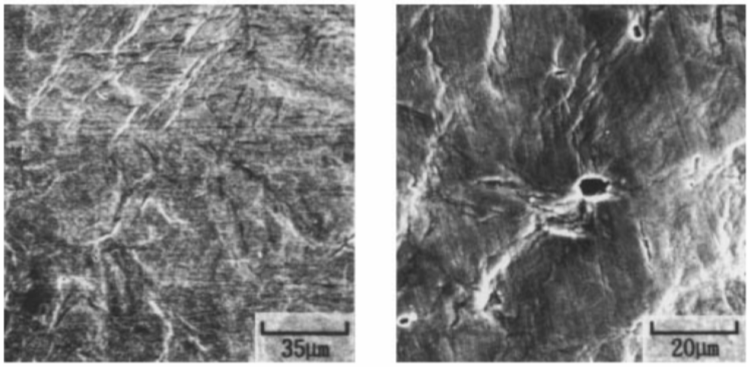

(a) point 1 (a) point 1

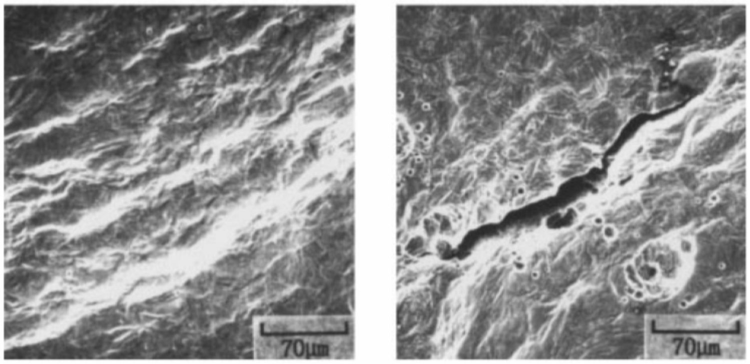

(b) point 4 (b) point 2

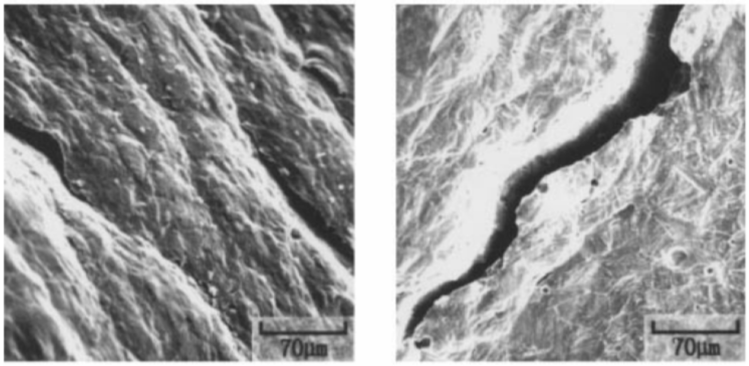

(c) point 5 (c) point 3

(A) Air (B) SSW-pH8.2

Fig 1.9: Micrographs of the specimen surface in air and in the synthetic sea water, pH 8.2 environment [88].

1.5 Defect-free channeling in deformed metals

- Defect-free channeling in unirradiated materials

Irradiation induced hardening due to numerous small defects clusters is very often accompanied by localized dislocation glide during plastic deformation. The microscopic mechanisms of strain localization usually observed in irradiated materials are dislocation channeling. A number of studies have been employed to indicate the features for these mechanisms in the past few years [21, 22, 46, 90-107]. Several years ago, a lot of researchers used different methods to investigate slip channels [90-98]. M.S. Bapna et al [90-92] examined the deformed structure of quench-hardened gold with

TEM. They found that plastic deformation takes place in confined regions, thereby forming the slip channels which are free of tetrahedral stacking faults. T. Mori et al [93] studied the deformation morphology of quench-hardened aluminum with TEM. The results showed that plastic deformation occurred only in distinct slip bands and that these slip bands corresponded to vacancy loop free channels. Ritschel et al [94] studied the channel slips in pre-strained molybdenum single crystals. Their results indicated that the formation of distinct slip channels in prestrained crystals is linked to the simultaneous fulfillment of the following conditions: (1) the prestrained sample must contain a homogeneous dislocation structure, in which there is no noticeable excess of dislocations of one sign; (2) the subsequent strain must take place at a temperature such that on the one hand collective dislocation movements are able to occur, and on the other hand the barrier dislocations present become sufficiently mobile. Besides, many researchers [95-98] observed the precipitate-free slip zones in precipitation hardened materials.

- Defect-free channeling in irradiated face-centered cubic (fcc) materials

Microscopic strain localization in face-centered cubic (fcc) pure metal or alloys has been observed by a number of researchers all over the world in many metallic materials such as Cu, Ni, Cu alloy and austenic steels after several different kinds of irradiation conditions [90-95]. Since 1960s, scientists [21, 100-102] began to study the deformation and slip bands of neutron irradiated copper crystals. They found that copper crystals yielded in relatively few strongly developed slip bands. The deformation in the slip bands was caused by glide of inclined dislocations close to screw orientation belonging to the primary slip system and radiation-induced point-defect clusters were swept out by the dislocations forming superjogs. Y. Dai, D.J. Edwards and J. S. Robachy et al [21, 100, 101] observed the dislocation channeling after proton, neutron and ion irradiation in Cu and Cu alloy. Particularly, D.J. Edwards [100] tried to illustrate initiation and propagation of channels during post-irradiation deformation of neutron irradiated Cu and Cu alloy. Some of their results were presented as in Figure 1.10. According to the observations, they suggested that the channels were initiated at boundaries, large inclusions and even at previously formed cleared channels. Some of the channels have been observed to penetrate through both the twin boundaries and grain boundaries. It was argued that the high stress level reached during post-irradiation tensile tests activate dislocation sources at the sites of stress concentrations at boundaries and interfaces.

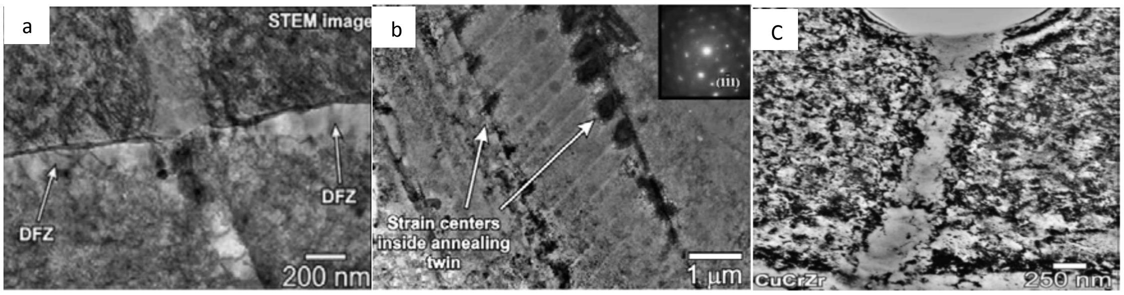

Fig 1.10: The images in (a) shows view of the intersection point of a channel with a grain boundary (b) shows strain accumulation on the inside of the annealing twin where the channels intersected and (c) a channel has been formed in the grain interior from an inclusion that fell out during electropolishing [100].

Z. Yao et al [102] observed dislocation channels in single crystalline Ni irradiated with 590 MeV protons. It appeared that in the 0.13 dpa specimens dislocation channeling is the initial deformation mode. The dislocation image is shown in figure 1.11.

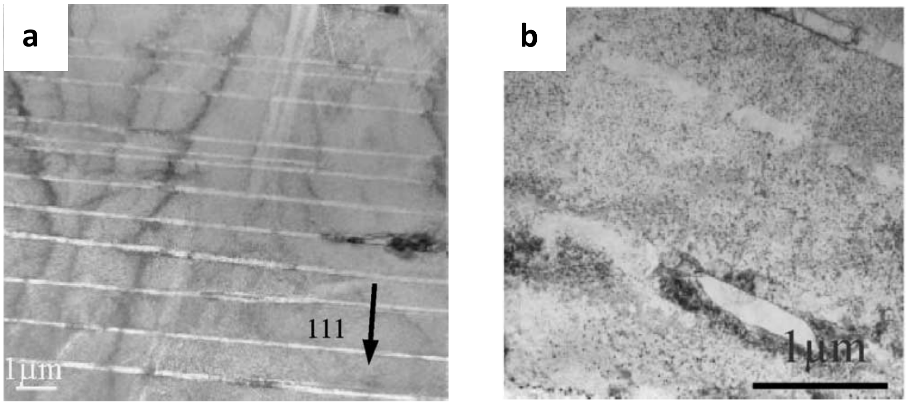

Fig 1.11: Deformation channels in (a) 0.13 dpa at RT specimens.
(b) channels containing blocked dislocations [102].

The dislocation channels in post-tensile microstructures of irradiated austenitic steels were studied by T.S. Byun, Z. Jiao et al [22, 103]. T. S. Byun et al [22] found that cleared channels were the dominant deformation mechanism after neutron irradiation to a dose of 0.78 dpa. Both the uniaxial tensile loading and the multiaxial bend loading produced straight channels, which form well-defined narrow bands. The dislocation channel images in 316 stainless steel irradiated by fast neutrons are shown in Figure 1.12. Jiao et al [103] investigated the deformation microstructure of three model alloys (E(UHP-304), H(304+Si), L(304+Cr+Ni)) which were irradiated with 3.2 MeV protons at 360 °C to 1.0 and 5.5 dpa and then strained in 288 °C Ar atmosphere. From the research, near defect-free dislocation channels were observed in austenitic alloys irradiated to 5.5 dpa and strained to 7%. Channel expansion was found at locations where channels intersecting with grain boundaries or other channels. The main results are shown in Figure 1.13.

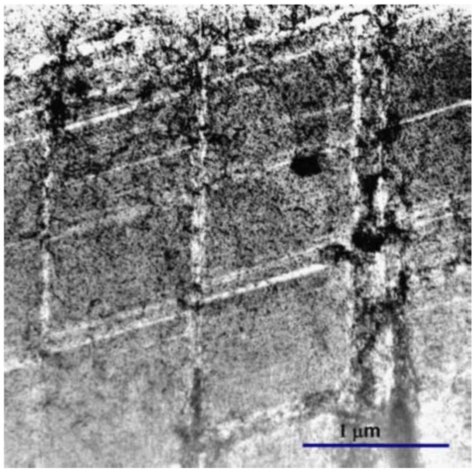

Fig 1.12: Network of dislocation channels in 316 stainless steel irradiated by fast neutrons to 0.78 dpa and tensile strained 32% [22].

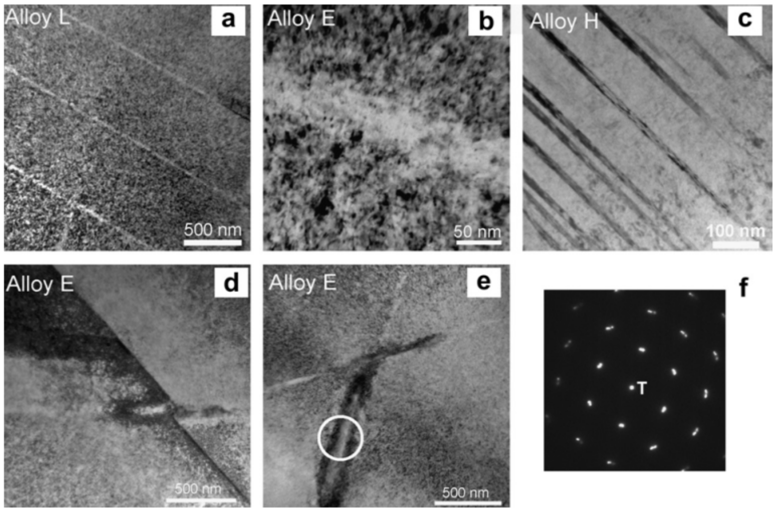

Fig 1.13: Deformation microstructure in alloys H, E and L irradiated to 5.5 dpa and strained to 7%: (a) dislocation channels, (b) a dislocation channel at high magnification, (c) deformation twins, (d) an expanded channel intersecting a grain boundary, (e) channel expansion at a channel–channel intersection, and (f) selected area diffraction pattern taken from the expanded channel in (e) showing atomic planes rotation [103].

- Defect-free channeling in irradiated body-centered cubic (bcc) materials

A few of body-centered cubic (bcc) pure metals or alloys such as Fe, V, V alloy and ferritic steels were also taken to investigate the microscopic deformation mechanisms [22, 46, 104-107]. The dislocation channeling in pure vanadium (BCC) was studied by T.S. Byun et al [22] after tensile deformation and bend deformation. The shape of the strain localization bands was found to be completely different from that in fcc structure metal. In vanadium specimens, curved channels were observed after tensile deformation, and these became a common feature after multiaxial bend deformation. A river pattern of channels was observed in the bent samples after irradiation to a high dose of 0.69 dpa. A highly curved channel can be formed by successive cross slip of screw dislocations. Also, the channel width was not constant along the channel, channel widening occurred when weak defect clusters were removed by the gliding screw dislocations changing their paths by cross slip. Figure 1.14 presents complex channeling features after neutron-irradiation to 0.69 dpa and disk bend deformation to 10% strain. The channels can be splitting, merging, widening, and curving during propagation. TEM micrographs of bcc vanadium in this study also show that channels in vanadium are formed primarily on [112] planes with a few exceptions in which channels are formed on [110] or [123] planes.

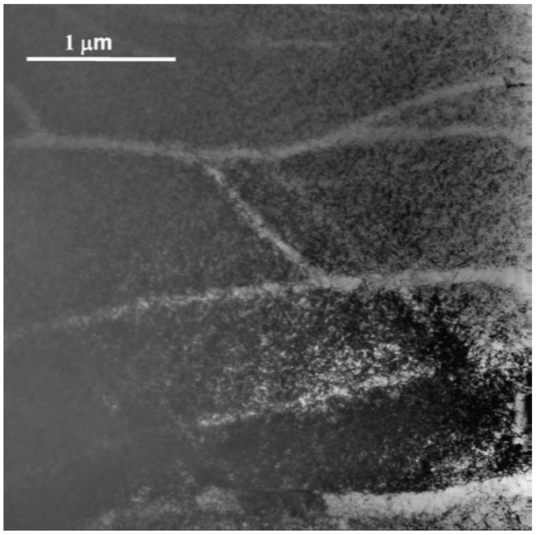

Fig 1.14: Deformation microstructures in vanadium after neutronirradiation to 0.69 dpa and disk bend deformation to 10% strain (Z=[-111]) [22].

The slip band of neutron-irradiated V-Cr-Ti alloys deformed in a tensile test was investigated by. M. Sugiyama et al [104]. TEM micrographs of irradiated specimens deformation formed to the UTS stress are shown in Figure 1.15. Outside of the deformation band, a lot of defect clusters are found, whereas inside the band no defect clusters or dislocation lines are seen. No dislocation walls or network can be observed on the interface between the matrix and the deformation band. The deformation bands entirely traversed grains and extended into the next grain across the grain boundaries.

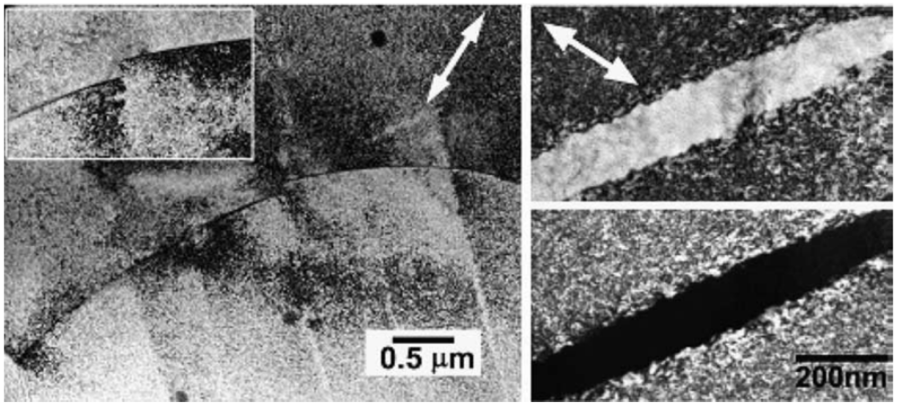

Fig 1.15: TEM micrographs of a deformed V–4Cr–4Ti alloy at the UTS. The left micrograph shows dislocation channels crossing grain boundary. The right one shows the BF and DF images inside of a dislocation channel [104].

B. N. Singh et al [105] investigated the microstructures of irradiated pure iron after tensile test. It is suggested that the formation and interaction of cleared channels may play a significant role in determining the deformation and fracture behavior of the irradiated pure iron. The plastic deformation seems to be concentrated mainly in the cleared channels (Figure 1.16). There is generally no indication of dislocation generation and interactions in the volumes between the cleared channels. Furthermore, it is rather significant to note that the formation of cleared channels at this dose level becomes so extensive that the cleared channels begin to interact with each other. This could be very important from the point of view of crack nucleation and fracture of the material.

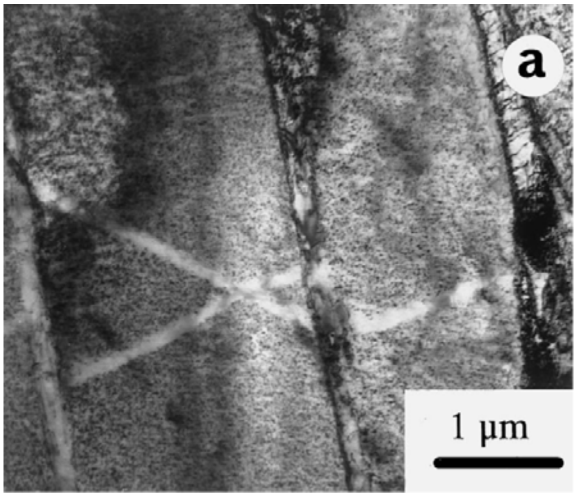

Fig 1.16. TEM image of Pure iron post-deformation microstructure, irradiated at 320 K to 0.375 dpa (NRT) and tensile tested at 320 K [105].

S.J. Zinkle et al [46] used tensile specimens of pure Fe which were neutron irradiated at 50-70 °C in three fission reactors to 0.0001-0.79 dpa to investigate deformation mechanism of pure Fe after neutron irradiation. Examination of specimens after tensile deformation revealed localized deformation in the form of cleared dislocation channels. Relatively few channels were formed in the uniform elongation region of the gage section. Dislocation channels on multiple slip systems were observed in the deformation region near the fracture surface, presumably due to the multiaxial stress state produced during necking and fracture of the tensile specimen. The microstructure of specimens tensile tested following irradiation at 0.4 dpa was shown in Figure 1.17.

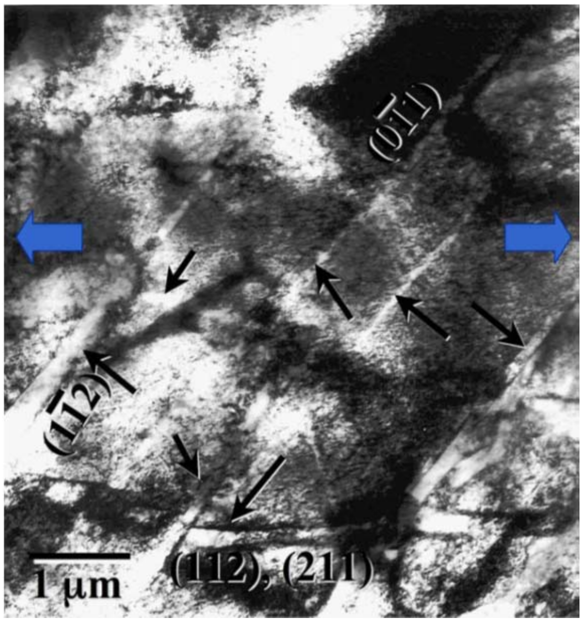

Fig 1.17: General microstructure near the fracture surface of Fe irradiated to 0.4 dpa at 70 °C and then tensile tested. Several cleared channels are marked with small arrows. The large arrows show the direction of the applied uniaxial stress. The zone axis is near [111]. The slip plane traces for several dislocation channels are also labeled [46].

The dislocation channels were associated with the 1/2 <111> {110} slip systems and 1/2 <111> {211} slip systems in BCC Fe. It can be seen that most of the cleared dislocation channels are oriented near the maximum resolved shear stress position 45° from the applied uniaxial stress. In particular, the channels running diagonally in Figure 1.17 correspond to the (1-12)[-111] and (0-11)[-111] slip systems, which have the maximum resolved shear stress for {112} and {110} slip planes in this grain. The horizontal dislocation channel corresponds to (-112)[1-11] and (21-1)[1-11] slip systems, both of which have a resolved shear stress that is only 40% of the maximum resolved shear stress. They found the horizontal dislocation channel appears to have formed prior to the diagonal channels, this suggests the dislocation source responsible for the horizontal channel formation may have been associated with a localized stress concentrator such as a grain boundary inclusion that cause the source to begin operation at relatively low applied stress. Besides, they also found the number of cleared dislocation channels was considerably higher in TEM specimens taken near the fracture surface compared to the uniform strain region in the tensile gage section.

Investigations of deformation mechanisms in irradiated bcc crystal structure ferritic steels were seldom reported. So far, only N. Hashimoto [106] and K. Farrell [107] published the results of the dislocation channeling observation in F82H steel (F/M structure) and A533B steel (tempered ferrite bainitic structure), respectively. N. Hashimoto et al observed defect free bands, which may be dislocation channels in the microstructure of the necked region irradiated at 300 °C and tested at RT. The defect free bands were shown in Figure 1.18.

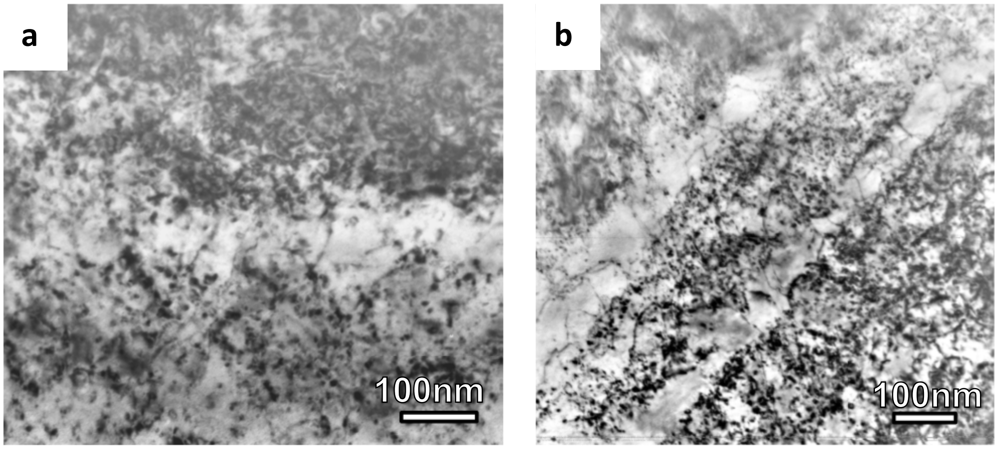

Fig 1.18: Microstructure of F82H (IEA heat) irradiated at 300 °C and tested at RT (a) and (b) [106].

Deformation bands with a 100 nm in width were lying on the (110). The result suggests that dislocation channeling appears to be the dominant deformation mechanism, resulting in the loss of strain-hardening capacity at 300 °C.

K. Farrel et al [107] observed dislocation channeling in the samples of 0.1 and 0.89 dpa, where large increases in yield stresses accompanied by prompt plastic instability failures as shown in Figure 1.19.

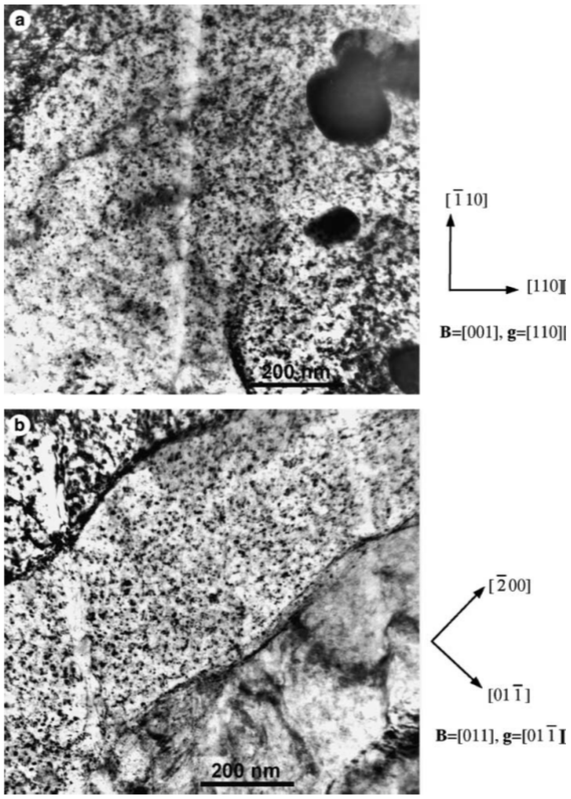

Fig 1.19: Dislocation channels in A533B steel: (a) and (b) from different places, at 0.89dpa after 0.2% strain. Defect clusters (black dots) are evident at this dose [107].

They are about 30 nm wide. The channels pass undeflected through the laths but change direction at the former bainite packet boundaries.

From the theory aspect, Tomas Diaz de la Rubia [99] used dislocation dynamics (DD) simulation to investigate the relation between the irradiation field and mechanical behavior. The simulation in Cu shows the two partial dislocations move under an applied stress of 300 MPa, the leading partial dislocation is initially pinned by the overlapping SFT. At a later time, then the leading partial dislocation absorbs part of the overlapping stacking-fault tetrahedra (SFT) and climbs (clearly seen in <110> projection) as the trailing partial dislocation approaches, and finally the trailing partial dislocation catches the leading partial dislocation at the location of the overlapping SFT, constricts and climbs by absorbing the remaining defect. Following absorption of the SFT, the dislocation continues to move but with reduced mobility as a result of the jogs that form on the constricted line movement.

1.6 Deformation twinning

In irradiated metals, T.S. Byun et al [108] found that deformation microstructure changed from dislocation networks dominant to a large stacking fault/twin band dominant microstructure with increasing radiation dose in 316LN stainless steel. Large stacking faults (>1µm)/twin bands became dominant at stresses >600 MPa in 316LN regardless of different strengthening methods such as irradiation dose, strain hardening and low temperature. Dense twin lamellas with $\{111\}$ twin plane were observed by Dai et al [109]. The width of the twin lamella and their bundles varies from a few nanometers to more than 100 nm. Zinkle et al [110] also mentioned that twinning appears when glide dislocations are strongly pinned by defect clusters (so that normal dislocation glide deformation cannot occur up to very high stress levels). The interaction of defects and moving twinning boundaries has been studied by atomistic simulation previously [111, 112]. A. Serra et al [112] investigated the interaction of moving $\{10\bar{1}2\}$ twin boundary with clusters of self-interstitial atoms and vacancies in a hcp metal with perfect dislocations and dislocation loops. They found that the moving interfaces can restrict the mobility of twinning boundary, modify the material microstructure by either removing or changing components of it depending on the nature of boundary. Whereas, M. Niewczas et al [111] studied the interactions of moving boundaries with stacking fault tetrahedra (SFTs) in copper by molecular dynamics. The results reveal that these interactions lead to damage of the parent SFT and formation of new defects in the twin lattice.

As a matter of fact, deformation twinning has been observed in a number of brittle materials including metals and ceramics under different kinds of mechanical tests such as high strain rate test (Charpy impact or shock loading) [113-117] and low temperature testing [118, 119]. A lot of evidences have been reported to prove that the cleavage and intergranular fracture in metal and ceramic has relation with twinning deformation. All of these research works include experiment and simulation. All the former results show that mechanical twinning plays an important role in the cleavage or intergranular fracture. Tibor et al [120, 121] found that ductile-brittle transition (DBT) of bcc Fe and some ferritic steels can be closely related to the occurrence of deformation twinning from SEM observation of Charpy impact testing sample. Jan et al [116] observed that deformation twinning was in the vicinity of the main cleavage crack and numerous cleavage nuclei were revealed on the twins in the close vicinity of cleavage facets in Charpy impact testing sample by SEM. They concluded that the deformation twinning represents an integral part of the deformation processes in the region of the propagating cleavage crack tip and that the deformation twins, which nucleate in front of the crack act as nucleation sites for cleavage fracture nuclei. Chen et al [122] observed deformation twinning underneath cleavage fracture surface in shock loading alumina sample by HRTEM observation.

Simkin et al [123, 124] and T.R. Bieler et al [125] found that microcracks were observed at strains below but near the fracture strain of a near-gamma TiAl alloy where deformation twins interacted with grain boundaries. And the microcracks were speculated to be caused by the twin shear that generated a concentrated opening force on one side of the twin at the boundary interface. The crack opening is expected as a consequence of twin shear as shown in a schematic representation in Fig. 1.20 [124]. The twin shear on the illustrated $(1\bar{1}1)$ plane moves material away from the boundary on the upper right side of the twin plane. (On the opposite side of this plane, i.e. the $(\bar{1}1\bar{1})$ plane, the twin shear would be in the opposite direction and move material on the lower left of the twin toward the boundary.) As the $(1\bar{1}1)$ plane twin develops, it requires a jog in the boundary, which can be accommodated elastically and possibly plastically by slip in the lower grain. As the twin thickens, a crack forms that follows the twin interface along the grain boundary-twin interface, beneath as well as on the surface of the material (the same microcracks were observed after removal of 3 μm from surface).

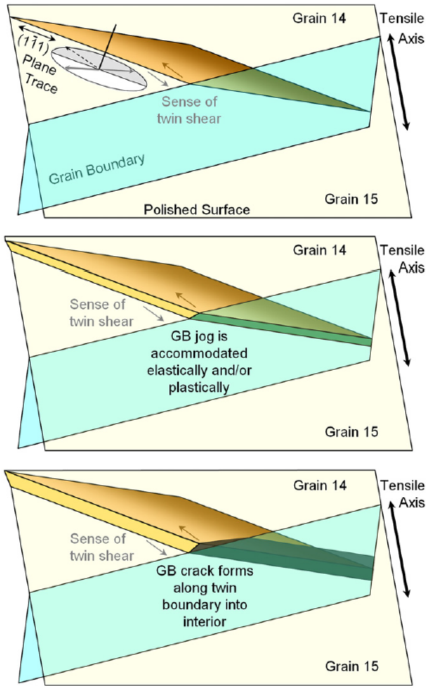
Grain 14
Tensile Axis
$(1\bar{1}1)$ Plane Trace
Sense of twin shear
Grain Boundary
Polished Surface
Grain 15
Grain 14
Tensile Axis
Sense of twin shear
GB jog is accommodated elastically and/or plastically
Grain 15
Grain 14
Tensile Axis
Sense of twin shear
GB crack forms along twin boundary into interior
Grain 15

Fig. 1.20: Schematic view of twin growth before microcrack nucleation for twins [124].

More recently, Zhang [126, 127] also observed that deformation twinning could cause crack nucleation in bcc nanocrystalline Mo by molecular dynamic (MD) simulation. In <110> columnar nanocrystalline body-cnetered cubic Mo, deformation mechanism is dominated by deformation twins which nucleate primarily from the grain boundaries by successive emission of twinning partials and thickens by jog nucleation in the grain interiors. As a twin approaches a grain boundary, local stress concentration develops due to the incompatible plastic deformations in the two neighboring grains. The magnitude of the stress concentration increases as the twin widens, leading to grain boundary cracking by nucleation and coalescence of microcracks/voids. The proposed mechanism for twin-induced GB cracking is illustrated in Fig. 1.21. The model of two neighboring grains (grains 1 and 2) with a twin formed in grain 1 and intersecting with the corresponding GB is shown in Fig. 1.21(a). To accommodate the lattice rotation caused by twinning in grain 1, the GB is subjected to a displacement Δ proportional to the twin width h (number of twinned layers) by $\Delta = h\ (\hat{b} \cdot \hat{n})$. Here $\hat{b}$ is the Burgers vector for the twinning partial and $\hat{n}$ is the GB normal (see Fig. 1.21(a)). Such a GB displacement is not allowed if no compatible plastic deformation occurs in grain 2, resulting in concentrated tensile stress at the intersection. The stress concentration magnifies as the twin in grain 1 widens, until the GB is pulled open to nucleate a GB crack. As shown in Fig. 1.21(c), as the twin widens, the plastic deformation mismatch between grains 1 and 2 intensifies, as does the stress concentration. Consequently, GB failure takes place and leads to intergranular fracture (Fig. 1.21 (d)).

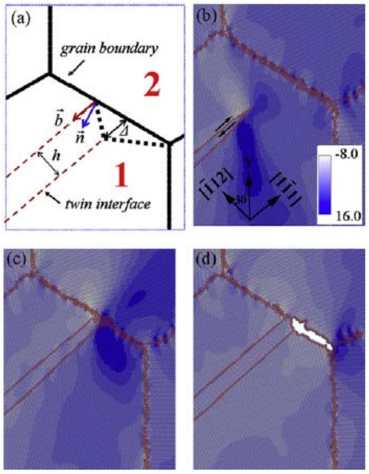

Fig 1.21: (a) Schematic mechanism of twin-induced GB cracking, and distribution of atomic stress σ_{yy} (GPa) near a GB at (b) 3.3%, (c) 3.4% and (d) 3.7% tensile strain. The twin boundaries and GBs are outlined by red dots. Tensile loading is applied along Y axis [126].

One prominent class of dislocation sources for twinning dislocations is that of pole mechanisms, which produce spiral dislocations. Considering bcc crystals, evidently, if the spiral dislocation b=$\frac{1}{6}[111]$ has a pitch equal to the interplanar spacing of $\{112\}$ planes and moves in a direction to produce fault I_1, a twin will be formed [128]. Cottrell and Bilby [129] proposed a pole mechanism that fulfills the above requirements for bcc crystals. Their model is illustrated in Figure 1.22. A $\frac{1}{2}[\bar{1}\bar{1}\bar{1}]$ dislocation lying on (112) plane dissociates by the reaction

$$\frac{1}{2}[\bar{1}\bar{1}\bar{1}] \rightarrow \frac{1}{3}[\bar{1}\bar{1}\bar{2}] + \frac{1}{6}[111] \qquad (1.4)$$

Which involves a zero change in elastic energy to first order, but that can occur under bow-out stresses. The partial $\frac{1}{6}[111]$ cross slips onto $(1\bar{2}\bar{1})$ as shown in Fig. 1.22 (a). The partial can then wind around the $\frac{1}{3}[\bar{1}\bar{1}\bar{2}]$ pole dislocation. The pole dislocation has a right-handed screw component normal to $(1\bar{2}\bar{1})$ planes. Thus the partial forms a spiral and generates a twin with twinning plane as $(1\bar{2}\bar{1})$ and shear direction as $[\bar{1}\bar{1}1]$.

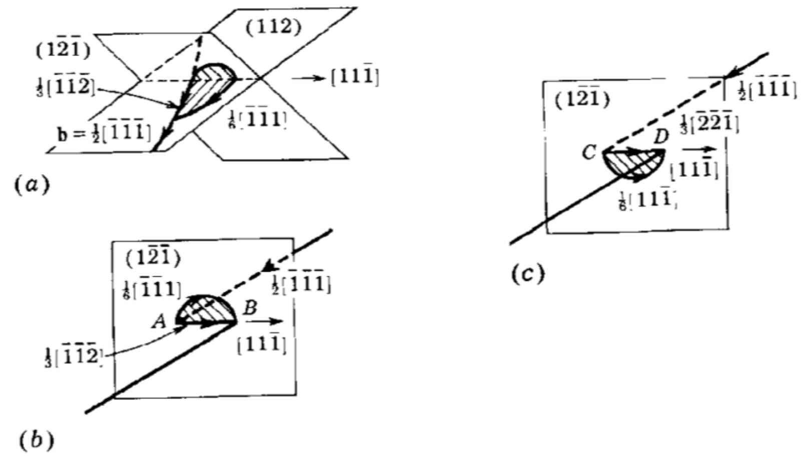
(1$\bar{2}\bar{1}$)
(112)
$\frac{1}{3}[\bar{1}\bar{1}\bar{2}]$
[11$\bar{1}$]
b = $\frac{1}{2}[\bar{1}\bar{1}\bar{1}]$
$\frac{1}{6}[\bar{1}\bar{1}1]$
(a)
(1$\bar{2}\bar{1}$)
$\frac{1}{6}[\bar{1}\bar{1}1]$
$\frac{1}{2}[\bar{1}\bar{1}\bar{1}]$
A
B
[11$\bar{1}$]
$\frac{1}{3}[\bar{1}\bar{1}\bar{2}]$
(b)
(1$\bar{2}\bar{1}$)
$\frac{1}{2}[\bar{1}\bar{1}\bar{1}]$
C
D
$\frac{1}{3}[\bar{2}\bar{2}\bar{1}]$
[11$\bar{1}$]
$\frac{1}{6}[11\bar{1}]$
(c)

Fig 1.22: (a) The Cottrell-Bilby ratchet-pole mechanism in a bcc crystal. (b) Jog version of (a). (c) Alternate pole mechanism [129].

Pirouz et al [130] proposed a twinning mechanism for silicon based on the presence of a pinned segment of a twining partial (Burgers vector b_t). The original model assumed the dissociation of a perfect srew dislocation segment (Burgers vector b) into a twinning partial (Burgers vector b_t) and a 'stationary' (or slow-moving) partial (Burgers vector b_s). The twinning partial can bow out under the application of a shear stress, forming an expanding faulted loop in a similar manner to a Frank-Read source for perfect dislocations, and regenerating the original perfect screw segment in the process. The model is based on well-established dislocation physics involving Frank-Read sources, with the difference that the expanding dislocation segment is a partial dislocation rather than a perfect dislocation. Then Lagerlöf et al [131] discussed the nucleation and growth of deformation twins based on the double cross slip mechanism postulated by Pirouz. Whether slip or twinning dominates depends on whether the dislocation can dissociate and on the relative mobility of the partial dislocations, b_t and b_s. It is possible to find conditions for which the leading partial may become glissile whereas the trailing partial is not moving (or moving very slowly), that is twinning may be nucleated. As the radius of the expanding loop increases, the applied stress will only need to overcome the lattice resistance involved in forming the stacking fault and the Peierls stress. After the expanding loop has been formed, the twinning partial and the less mobile partial react to reform the initial perfect dislocation segment b. In as much as the perfect dislocation segment is assumed to be in screw orientation, the dislocation segment can undergo cross-slip onto a suitable cross-slip plane. In this case, the dislocation segment moves to a plane parallel to a plane containing the faulted expanding loop. After cross-slip, the segment could again dissociate into a twinning and a sessile partial, and the twinning partial would bow out to form a second expanding loop. Thus double cross-slip accounts for thickening of the twin (or vertical twin growth) as shown in Fig.1.23. This double-cross-slip mechanism requires that the original screw segment forms a threading dipole connected to the twinning dislocations at the twin boundary.

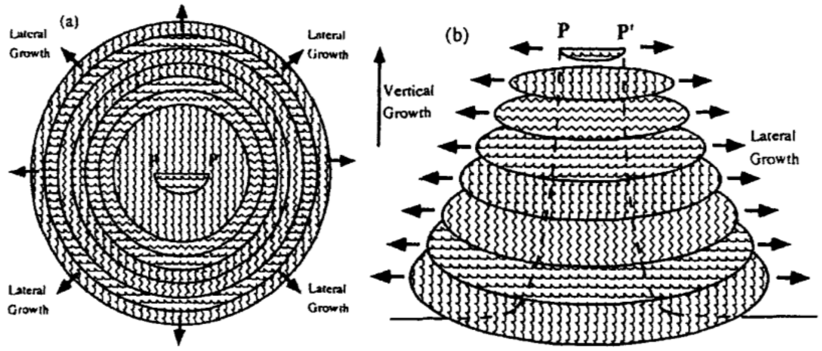

Fig 1.23: Schematic view of twin growth via the double-cross-slip mechanism [131].

According to the classical view, the nucleation of deformation twinning has strong relation with stacking fault energy. For the high stacking fault energy materials such as α-iron, aluminum and tungsten and so on, deformation twinning dominates deformation mechanism only in some extreme conditions like low temperature and high strain rate [113, 114, 116-118, 120, 132-136]. However, in recent years, deformation twinning has also been observed in nanocrystalline metals such as Al, Mo and W [126, 127, 137, 138]. Grain size effect serves as another important parameter for deformation twinning. However, deformation twinning also exhibits reversed crystal size effect in certain condition such as HCP metal [139]. So far, the deformation twinning is considered to have relation with intrinsic factors such as SFE, crystallographic orientation, and grain size and extrinsic factors such as applied stress, strain rate and testing temperature. Chen et al [137] observed deformation twinning in nanocrystalline Al and they propose a dislocation-based model as shown in Eq. 1.5 and 1.6 to explain the preference for deformation twins and stacking faults in nanocrystalline materials. The transition of deformation mechanisms from normal slip to those controlled by partial dislocation activity can be expected when grain size decreases to tens of nanometers.

$$\tau_N=\frac{2\alpha\mu b_N}{D} \tag{1.5}$$

and

$$\tau_P=\frac{2\alpha\mu b_P}{D}+\frac{\gamma}{b_P} \tag{1.6}$$

Where τ_N and τ_P is the critical shear stress needed to nucleate a perfect dislocation and Shockley partial twinning dislocation respectively, μ is the shear modulus, γ is the stacking fault energy, b_N and b_P are the magnitudes of the Burgers vectors of the perfect dislocation and the Shockley partial dislocation respectively, D is the source size of perfect dislocation or twinning dislocation which is equal to crystal size here. When the grain size becomes smaller than a critical value D_c determined by equating Eq. 1.5 and 1.6, τ_P becomes smaller than τ_N. In addition, Han et al [140] also observed microtwins and stacking faults in plastically deformed aluminum single crystal and they conclude that the occurrence of these microtwins and stacking faults is directly related to the specially designed crystallographic orientation. A developed universal dislocation-based model is proposed to judge the preference or not for the nucleation of deformation twins and stacking faults as shown in Eq 1.7.

$$\tau_{\text{required}} = \frac{1}{m}\left(\frac{\mu b_P}{D} + \frac{\gamma}{b_P}\right) \tag{1.7}$$

Where D, μ, γ and b_P are same as in Eq 1.5 and 1.6, m is the shear factor whose value varies from 0 to 1, depending on the relation between shear plane or shear direction and twinning plane or twinning direction. This model indicates that crystallographic orientation has a remarkable influence on the behavior of deformation twinning in aluminum. More recently, Rodney et al [141] provides a newfound orientation-based explanation for the grain size effect: as grain decreases the applied stress needed for further deformation increases, thereby allowing more orientations to reach the threshold stress for twinning.

In general, people assumed that twinning is often to be correlated with low stacking-fault energy, D.H.Warner et al [142] claimed that the correlation is not strong. The reason is that both Ir with highest stable stacking fault energies (480 mJ m^{-2}) and Ag with lowest (21 mJ m^{-2}) are twin fairly readily. They solved the discrepancy between theory and experiment on twinning nucleation through a new model guided and validated by extensive multiscale siumulations. Both the analytic model and simulations reveal a transition from crack-tip twinning at short times to full dislocation formation at long times. They consider the thermally activated nature of both twinning and dislocation slip to solve the discrepancy between theory and experiments. The extended two-dimensional (2D) analytic Peierls model of Rice and Beltz analytic model predicts that, in a wide range of f.c.c metals, the activation energy for full dislocation emission becomes lower than that for twinning with decreasing load, corresponding to longer times or slower strain rates. Besides, a multiscale modelling (finite-temperature concurrent multiscale coupled atomistic dicrete dislocation method) of Al crack tip also indicates that twin formation dominates at high loads KI>0.185eV Å-2.5 and very short times t<100ps at 300 K. As the load decreases, instances of trailing dislocation nucleation become dominant at the lowest loads and longest times t>10 ns. There is thus a transition from twinning to full dislocation emission with decreasing load or increasing time. This result can explain why cracks in Al are therefore not predicted to twin at room temperature except under the most extreme conditions of shock loading. For the high strain-rate test, J. Marian et al [135] present a new mechanism of dislocation motion by using atomistic simulations in iron. They observed that dislocation motion at high strain rates becomes rough, resulting in spontaneous self-pinning and production of large quantities of debris. Then, at still higher strain rates, the dislocation stops abruptly and emits a twin plate that immediately takes over as the dominant mode of plastic deformation.

Moreover, deformation twinning is also often observed in front of crack tip in high stacking fault energy materials from both experiment and simulation [138, 143-147]. Hai et al [143] found that for certain combinations of loading mode and orientation, deformation twinning does occur at aluminum crack tips from simulation. For bcc metals, Liu et al [144] demonstrate a twin-crack relation whereby (a) twins nucleate cracks and define a preferred cracking path and (b) a propagating crack facilitates twinning by in situ TEM observation in molybdenum thin film. Alena et al [145] observed crack induced twins extend toward the crystal in the <111> directions with the speed above the velocity of the shear waves in the <111> $\{112\}$ slip systems in bcc iron by free 3D atomistic simulations. Borodin et al [146] also observed multilayer stacking fault formation on $\{112\}$ planes for <110> propagation direction at temperature below 300 K by MD simulations. Besides, Li et al [147] reported the twinning and spontaneous detwinning phenomenon with unloading at the Al crack tip by in situ tensile straining under TEM observation. More recently, Wang et al [138] also observed that the deformation twinning is pseudoelastic, manifested through reversible detwinning in nanocrystalline tungsten during unloading in the in situ nanomechanical testing with high-resolution TEM (HRTEM).

1.7 Objective of this PhD research

As already mentioned,Ferritic/martensitic (FM) steels are considered as potential candidate materials for target structures of high power spallation neutron sources and structural materials for fusion reactors, because they possess higher mechanical strength at ≤500 ℃, better thermal mechanical properties and lower irradiation induced swelling as compared with annealed austenitic steels. However, high levels of irradiation-induced displacement damage and of helium (He) concentration can be produced in these materials. Fusion reactor neutron spectra produce both atomic displacement damage (dpa) and helium by transmutation at a relatively high rate as characterized by a He/dpa ratio of 10-15 appm He/dpa, while that ratio is even higher, up to 100 appm He/dpa, in spallation targets like SINQ. Up to now, although a number of experimental results show that irradiation displacement damage and helium cause a significant embrittlement effect on FM steels, there is still no clear understanding of the fundamental embrittlement mechanism of FM steels after irradiation. Furthermore, even the fracture micro-mechanisms including the nucleation and propagation of crack under brittle fracture condition are also not well understood.

In this PhD thesis work, the main issues proposed to be addressed for FM steels irradiated in SINQ (STIP-irradiation) are:

1) Characterization of microstructures (size and density of defects or helium bubbles) and their influence on the mechanical properties for FM steels irradiated in STIP.

2) Investigation on brittle fracture mechanisms (how the crack initiates and propagates) of FM steels irradiated in STIP.

3) The effect of the distribution of Helium bubbles in terms of size, density studied on intergranular and transgranular fracture mechanisms.

4) Understanding of deformation mechanism of FM steels irradiated in STIP (dislocation channeling observation).

5) Investigate the deformed microstructures underneath the fracture surfaces to gain insight into possible mechanism of crack initiation/propagation.

2. Experimental Methods

The chapter presents detailed information of the investigated materials, the irradiation conditions, the mechanical testing methods and the sample preparation techniques for mechanical properties and microstructural investigations. The main techniques and procedures are described in this chapter for the implementation throughout the whole thesis data analysis and result discussion. In this work, different kinds of mechanical testing methods including hardness measurement, tensile testing and small punch testing were employed to characterize mechanical properties, such as hardness, yield stress total elongation and to study the micro-cracking behavior. Conventional transmission electron microscopy observations were utilized to study the microstructure of the investigated materials, such as martensitic microstructures, precipitates and carbides, dislocations, irradiation-induced defect clusters, dislocation loops and helium bubbles, and to understand deformation-induced modification of the deformed unirradiated and irradiated microstructures.

2.1 Investigated materials, specimens and irradiation

2.1.1 Materials

Four different body centered cubic (bcc) ferritic/martensitic steels were studied after spallation neutron source irradiation. The investigated materials are F82H, Eurofer97, MANET II and T91. The main chemical compositions of these steels are listed in Table 1.

Table 2.1: Composition of the investigated materials in wt% (Fe in balance) [148].

Steel	Cr	Ni	Mo	Mn	Ti	V	Nb	W	Ta	Cu	C	Si	P	S	B	N
F82H	7.87	0.02	0.003	0.1	0.004	0.19	.0002	1.98	0.03	0.01	0.09	0.07	0.003	0.001	0..007	0.007
Eurofer97	8.93	0.007	<0.001	0.44	0.009	0.19	<0.001	1.10	0.14	0.022	0.12	0.07	<0.005	0.004	<0.001	0.017
MANET II	10.3	0.65	0.58	0.85	-	0.19	0.14	-	-	-	0.11	0.18	0.005	0.004	0.030	0.030
T91	8.63	0.23	0.95	0.43	0.003	0.21	0.09	-	-	0.046	0.1	0.31	0.02	0.006	-	0.03

The F82H steel, IEA Heat 9741, was obtained from fusion materials community in the form of a 15-mm-thick plate. The steel was normalized at 1040 °C for 38 min followed by air cooling, and then tempered at 750 °C for 1 h and followed by air cooling.

The Eurofer97 steel was received from FZK, heat No E83699, in the form of a 100-mm-diameter cylinder. The steel was normalized at 979 °C for 1 h 51 min followed by air cooling, and then tempered at 739 °C for 3 h 42 min and followed by air cooling.

The MANET II steel was obtained from the fusion materials community as a piece of 25-mm-thick plate. The steel was normalized at 1040 °C for 30 min followed by air cooling, and then tempered at 750 °C for 2 h and followed by air cooling.

The T91 steel was obtained from CEA, France. The heat number was 36224. The as-received material was a 15-mm-thick plate. The steel was normalized at 1040 °C for 1 h and followed by air cooling, and then tempered at 760 °C for 1 h and followed by air cooling.

Metallography images showing the prior austenite grain (PAG) and martensite lath structures of the investigated materials are presented in Figure 2.1.

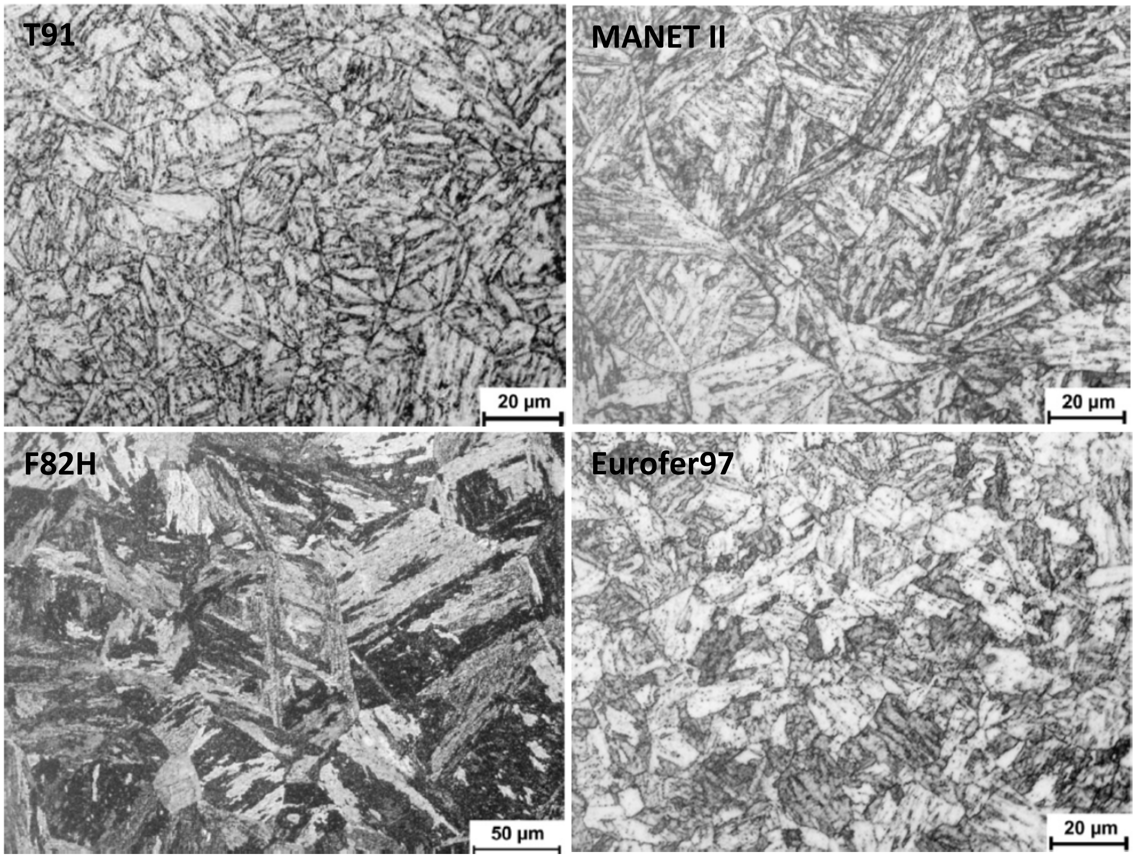

Fig 2.1: Optical micrographs of different F/M steels [148].

For a comparison, the heat treatment parameters and the resulting PAG size are presented in Table 2. The results of the micro-hardness ($HV_{0.05}$) of as-received materials after heat treatment were also added in the Table.

Table 2.2: Heat treatment conditions, mean PAG size and micro-hardness measurement results of the tempered martensitic steels [148].

Materials	**Heat treatment conditions**		**PAG size**	**Micro-hardness**
	Normalization	Tempering	(µm)	($HV_{0.05}$)
F82H	1040 °C/38min	750 °C/1h	85±20	220±5
Eurofer97	979 °C/1h51min	739 °C/3h42min	16±2	237±5
MANET II	1075 °C/30min	750 °C/2h	32±2.5	268±5
T91	1040 °C/1h	760°C/1h	15±1.5	264±5

2.1.2 Irradiation conditions of the F/M steels irradiated at SINQ

All the tensile test specimens were irradiated in the Swiss spallation neutron source (SINQ) Target 4, within the 2nd SINQ Target Irradiation Program (STIP) II performed in 2000 and 2001. The aim of this program is to gain insight into the relation between microstructures and mechanical properties of irradiated structural materials in spallation targets.

In the SINQ target, the specimens were irradiated with a mixed spectrum of 570 MeV protons and spallation neutrons of a wide energy spectrum from 0 to 570 MeV. The irradiation was started on the 20th of March, 2000 and interrupted on the 23rd of December. It was resumed on the 15th of May and finally ended on the 23rd of December, 2001. The total irradiation period was about 16 months with total proton charge of 10.03 Ah. The beam profile on the SINQ target was fit as a 2D Gaussian distribution. The proton and neutron fluences, irradiation dose, helium and hydrogen production for STIP-II samples were calculated with the MCNPX code which is based on Monte-Carlo method. The irradiation temperature was influenced greatly by the proton beam current and frequent beam trips. Since the beam current fluctuated in about ±15% range, relatively large variation of irradiation temperature should be considered. The temperature calculation of each individual specimen relied on the simulation using the ANSYS code, which was based on the energy deposition values obtained from the MCNPX calculation. Further detailed information about STIP-II experiment can be found in [149]. It must be noted that the tensile specimens exhibit a dose and temperature gradient along the length direction due to the Gaussian distribution profile of the proton beam, giving rise to a higher dose side and a lower dose side at each tensile specimen. The detailed irradiation parameters of the investigated samples are given in Table 2.3.

Table 2.3: Detailed irradiation parameters of investigated materials.

Material	**Specimen**	**Irradiation dose [dpa]**	**Irradiation temperature [°C]**	**Helium Concentration [appm]**
F82H	K24-L	6.1	106	450
	K24-H	8.7	140	690
	K23-L	9.5	151	760
	K23-H	12.9	201	1085
	K18-L	9.2	133	715
	K18-H	12.3	175	1015
	K19-L	13.2	231	1305
	K19-H	17.2	241	1505
	K22-L	13.9	216	1180
	K22-H	17.7	273	1550
	K20-L	18.1	281	1600
	K20-H	20.4	317	1795
Eurofer97	IJ10-L	18.5	279	1635
	IJ10-H	20.4	309	1795
MANET II	O17-L	18.5	279	1635
	O17-H	20.4	309	1795
F82H	K24	7.4	122	565
	K23	11.1	174	910
	K18	10.7	166	850
	K19	15.2	236	1305
	K22	15.8	245	1370
	K20	19.6	304	1740
Eurofer97	IJ10	19.8	299	1750
MANET II	O17	19.8	299	1750

N.B. Upper part of Table: L and H refer to low- and high-dose specimen side.
Lower part of Table: average values.

2.1.3 Preparation of the tensile specimens for mechanical testing

The surfaces of the irradiated tensile specimens were slightly polished using grinding papers of 2400 grit to obtain smooth surfaces. In order to reduce the radioactive dose exposing to body, the operation had to be done quickly and carefully inside of lead-shielded ventilation chamber in the hot lab of PSI. After mechanical polishing the specimens were rinsed twice in Ethanol and followed by electro-polishing to remove the residual and hardened surface scratches and obtain good surface quality before hardness measurement and tensile test. An electrolyte with 2% Perchloric acid and 98% ethylene glycol monobutyl ether was used for final polishing. The electrolyte was cooled down to 0 °C, and a 40 V voltage was applied for 20s to 1min to remove 10 -30 µm thickness surface layer of the specimens.

2.2. Mechanical testing

2.2.1 Hardness measurement

Hardness is a useful and straightforward way to characterize the irradiation hardening as it measures the resistance of the material to the penetration of a sharp indenter tip loaded with a given weight. Hardness changes after irradiation can be correlated to the corresponding increase of yield stress [150]. Therefore, hardness measurement was realized on the tensile specimen heads before tensile testing. The measurement was carried out immediately after the final electro-polishing. The hardness value ($Hv_{0.5}$) was evaluated by using a ZWICK hardness tester as shown in Fig.2.2 (a) located in the hot lab with a Vickers indenter tip and a load of 0.5 N applied for 15 s. The horizontal and vertical diagonals of each indent shape as shown in Fig.2.2 (b) were measured under optical microscopy with maximum 60x magnification.

The set-up had to be properly adjusted before tests. The measurement was performed in a stable and anti-vibration situation. The hardness measurement was carried out on each head of a tensile specimen in order to gain the hardness values in both low dose and high dose heads. For the measurement on each head of specimen, 10 points were measured and the average value was calculated for the further comparison and hardening effect analysis.

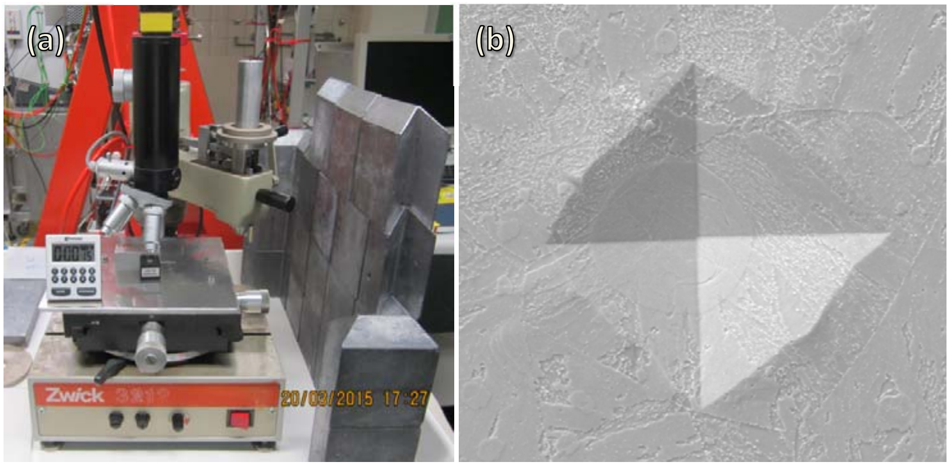

Fig 2.2: Hardness measurement device (a) and SEM image of the indent shape (b).

2.2.2 Tensile tests

Four tensile specimens of the F82H steel (K18, K19, K22 and K20) irradiated in STIP II in at different irradiation and test conditions as shown in Table 2.3 were selected to determine the change of the tensile properties such as yield stress, ultimate tensile stress (UTS), uniform elongation and total elongation after irradiation. Miniaturized dog-bone shaped flat tensile specimens with the dimensions of 12×2.5×0.4 mm^3 and gauge section of 5×1×0.4 mm^3 (Figure 2.3) were used.

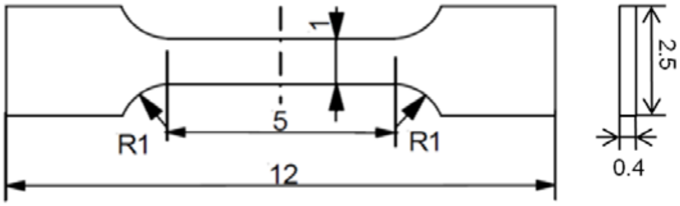

Fig 2.3: The dimensions of tensile test specimen used in this work.

The tests were done with a MTS testing device (Figure 2.4 (a)). Tensile tests at a norminal strain rate of 1×10^{-3}/s were performed at different testing temperatures in argon (Ar) environment. The temperature calibration was conducted before the test. Two thermal couples, one fixed on the lower specimen grip and the other fixed in the middle position of reference test specimen, were utilized to obtain the temperature relationship between two thermal couples in order to set the correct temperature values for high temperature tests. Home-made grips as presented in Figure 2.4 (b) were used to apply mechanical load on the shoulders of the specimens, so that the heads of the specimens were kept undeformed during tensile testing. The gauge section was marked by ink before test, which was employed for elongation measurement. The elongation value was obtained from a CCD camera extensometer as shown in Figure 2.4 (c). The specimen was preloaded to 40 N and the distance between the two blue lines was recorded from the CCD camera extensometer, then the testing was conducted at a constant cross-head speed of 0.3 mm / min up to failure.

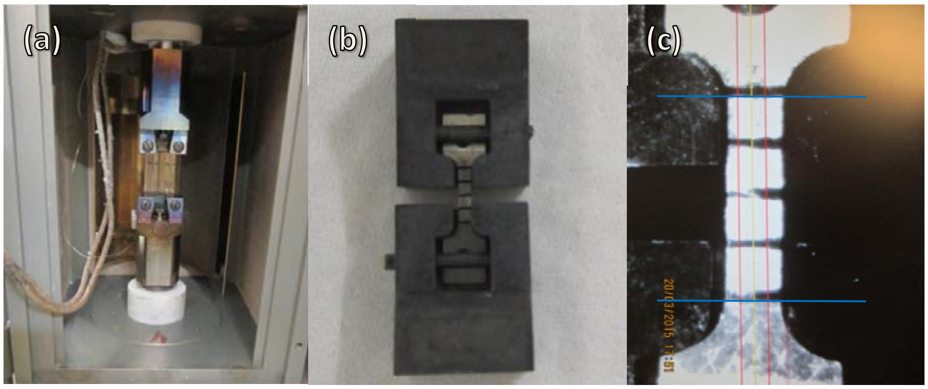

Fig 2.4: Pictures of tensile test device (a), sample grips (b) and CCD camera extensometer (c).

2.3 Investigation on the micro-crack initiation and propagation

2.3.1 Successive small punch testing with SEM observation

In order to investigate the cause of embrittlement, fast cracking behavior needs to be studied. Generally, the fast cracking behavior can be divided in 2 stages: the crack initiation stage and the crack propagation stage. Smooth specimens are commonly used in slow strain rate test (SSRT) or constant load/strain test for the crack initiation process study. Crack initiation can be detected by potential drop, compliance or electrochemical method to detect very small crack. In-situ optical observation systems were developed also, but the resolution is usually too low (detection by CCD camera) to observe the roots of crack initiation. The crack propagation was widely investigated using pre-cracked specimens based on the fracture mechanism with aim the quantification of the crack growth rate. In recent work, successive small punch (SP) test and tensile test combined with SEM observation were employed to investigate the micro-crack initiation and propagation. In order to investigate the micro-cracking, SEM observations were done to monitor the micro-crack initiation and propagation in the course of SP experiments. The SP test experimental configuration is presented in Figure.2.5. It consists of a clamped, center-loaded disk specimen. The SP specimen holder involves an upper and lower die, and four clamping screws. Using this sample holder, the samples are protected from cupping upward during punching. Therefore plastic deformation is concentrated in the punch contact region (1 mm ball). The SP test was conducted in Zwick mechanical testing machine, with a maximum load capacity of 20 kN. The displacement was measured by extensometer as indicated in Fig.2.5 during tests. A unique tank as low temperature device was designed to obtain test temperatures from liquid nitrogen temperature to room temperature. For this research, room temperature and liquid nitrogen temperatures were considered for tests. The temperature was measured with a thermocouple set into the specimen die 0.5 mm away from the specimen.

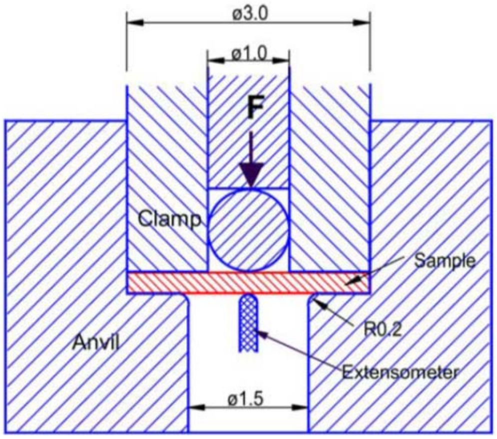

Fig 2.5: The schematic of Small Punch test set-up [77].

In order to observe grain boundaries and lath boundaries, the mirror polished specimens with 0.25 mm in thickness and 3 mm in diameter were etched in the solution (45 ml HCl+20 ml HNO_3+35ml H_2O) before testing. The testing was performed with a constant crosshead speed of 0.1 mm min^{-1}. The load-displacement curve was measured during tests.

The test procedure of successive SP test is described as follows:

1. Stop testing in certain deformation levels.
2. Take out the specimen from SP set-up carefully for SEM observation.
3. Inspect the micro-crack on the surface of the deformed specimen.
4. Place the specimen back to the SP set-up in the same position to continue the test for further deformation. Then repeat the step 1-3 for 4-5 times to monitor the crack initiation and propagation.

Five load-displacement curves were fit and merged into one curve after 5 times of deformation. Since the yield load was clearly increased after the previous deformation, only the part after yielding in the curve was extracted to attach to the previous curve. Finally, a merged load-displacement curve can be obtained.

2.3.2 Successive tensile testing with SEM observation

Successive tensile testing was employed to investigate micro-crack initiation and propagation behavior. The testing was performed with the same crosshead speed of 0.3 mm min^{-1}. The three F82H (K24, K23 and K22) and two MANET-II specimens (O16 and O19) shown in Table 2.3 were used for the tensile tests at room temperature.

The test procedure of successive tensile testing and SEM observation is described as follows:

1. Start a tensile test in the same way as described in section 2.2.2
2. Stop the testing at a desired deformation level, for instance the point 1 as shown Figure 2.6
3. Take out the specimen from the tensile machine carefully.
4. Inspect the micro-crack on the surface the specimen with SEM.
5. Place the specimen back to the tensile machine in the same position to continue the test to the next desired deformation level. Then repeat the above steps 4-5 times to monitor the crack initiation and propagation.

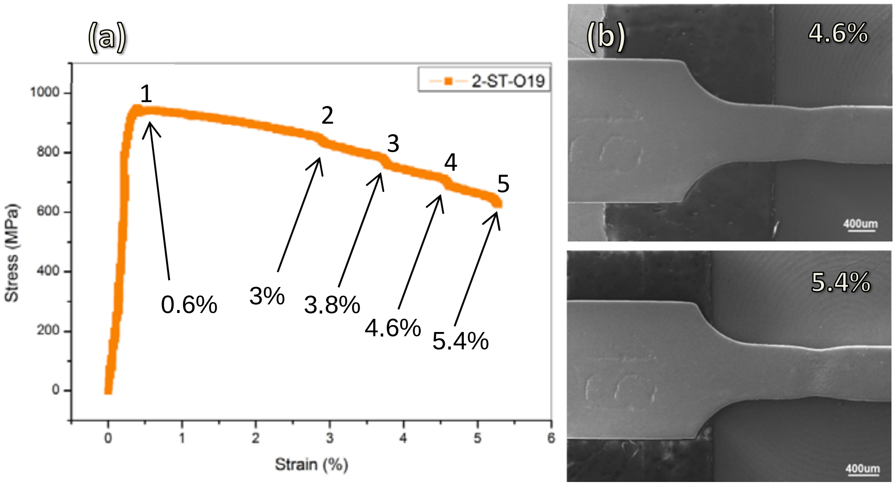

Fig 2.6: Illustration of successive tensile tests, (a) tensile curve and different unloading points (b) SEM images in different unloading points under low magnification.

In order to investigate the crack initiation and propagation, SEM observations of tensile samples taken at different deformation levels were performed as shown in Figure 2.6 (b).

2.4. Microstructure investigation with TEM technique

In this research work, the characterization of as-irradiated microstructure and deformed microstructure were used with a JEOL-2010 transmission electron microscope operated at 200 keV. A double tilt stage is applied for TEM observation. The purpose of specimen tilting is tilting specimens by fractions of a degree to gain optimum contrast such weak beam dark field (WBDF) diffraction conditions. The images were acquired with a slow scan CCD camera or on classical photographic negatives.

The contrast of small defect clusters varies greatly in the contrast conditions. The image quality and the visibility of nano-meter sized defect clusters depend strongly on proper focusing and correction of objective astigmatism.

The diffraction-contrast method is used in present work to characterize radiation-induced defects. The image characteristics depend sensitively on the diffraction conditions chosen.

Generally, for the characterization of tiny helium bubbles (1-2nm), the ‘two-beam’ conditions together with over-focused or de-focused technique were employed to take images as indicated in Fig. 2.7 (a).

Weak-beam dark-field conditions at z=111, (g, 5g) =110 were exploited to investigate irradiation-induced small defect clusters and dislocation loops as indicated in Fig. 2.7 (b) in recent work.

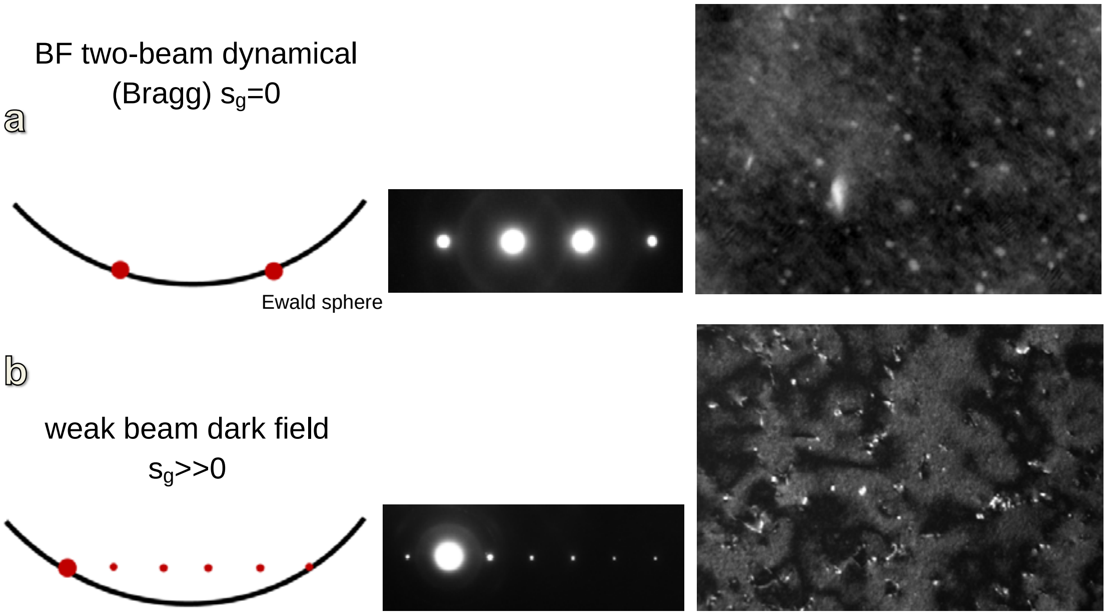

Fig 2.7: Schematic representation of imaging conditions employed in recent work. (a) bright field two-beam dynamic or exact Brag condition. (b) weak beam dark field (WBDF) condition. For each case the Ewald sphere is sketched in the left with the corresponding experimental diffraction pattern illustrated in the center. Representative TEM images are presented in the right.

2.4.1 Thickness Measurement

In order to evaluate volume number density of defect clusters and helium bubbles, it is necessary to measure the thickness of sample precisely.

2.4.1.1 Determination of specimen thickness via thickness fringes under WBDF conditions

The foil thickness was estimated using two different methods. A simple way is to count the number of thickness fringes from foil edge under the weak-beam dark-field conditions. Since the intensity I_g of the diffracted and I_0 of the transmitted beams oscillate in a complementary manner depending only on the sample thickness t if s_{eff} is constant, giving rise to a number of thickness fringes at the edge of a specimen with a wedge shape as shown in Fig.2.8. In a case corresponding to a weak-beam dark-field imaging condition, where $\mathbf{S_g} \neq 0$, the minimum for intensity I_g (dark fringe) occurs when $t=n\xi_g^{\mathrm{eff}}$, with the effective extinction distance ξ_g^{eff} introduced by equation (1.2) [55]. Therefore, thickness of the sample is directly proportional to ξ_g^{eff}. In this work, the thickness evaluation was carried out in the edge or boundaries region of specimen under WBDF conditions at z=111, (g, 5g) =110.

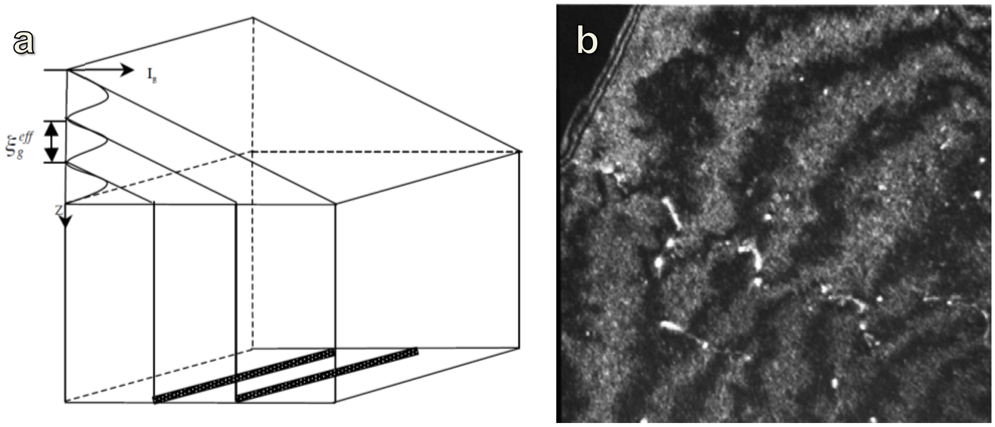

Fig 2.8: Schematic (a) and corresponding WBDF image of the thickness fringes formed in diffraction contrast by a wedged specimen (b), where Z is the thickness of specimen and I_g is the intensity of the transmitted beam.

2.4.1.2 Determination of specimen thickness via EELS

In the electron energy loss spectroscopy (EELS), a material is exposed to a beam of electrons with a known, narrow range of kinetic energies. Some of the electrons undergo inelastic scattering, which means that they lose energy and have their paths slightly and randomly deflected. The amount of energy loss can be measured via an electron spectrometer as shown in Fig.2.9 and interpreted in terms of what caused the energy loss. EELS allows a quick and reliable measurement of local thickness in transmission electron microscopy, with ±10% accuracy. The most efficient procedure is the following:

1. Measure the energy loss spectrum in the energy range about -5-200 eV. Such measurement typically lasts few milliseconds and thus can be applied to materials unstable under electron beam.
2. Analyse the spectrum: (i) extract zero-loss peak (ZLP) using standard routines; (ii) calculate integrals under the ZLP (I_0) and under the whole spectrum (I).
3. The thickness t of TEM specimen can be calculated as:
   $t= \lambda \cdot \ln (I/I_0)$, where λ is the mean free path of electron inelastic scattering dependent on the chemical composition of the sample, the incident energy of the electron beam and the collection semi-angle, which has been tabulated for most elemental solids and oxides. [151, 152].

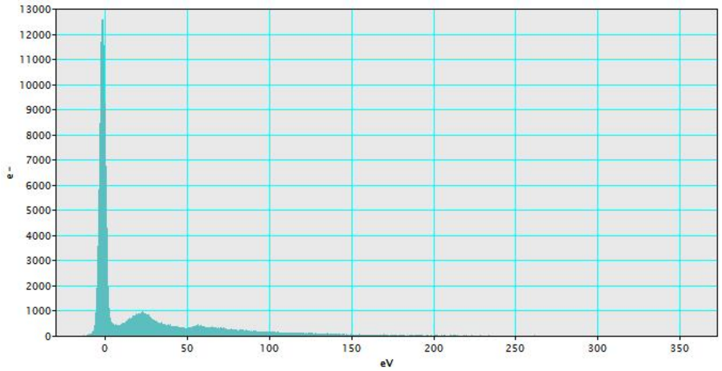

Fig 2.9: typical image of Electron energy loss spectrum.

In this work, a built-in option which is available in Gatan Digital Micrograph software was used to calculate thickness from the EELS spectrum. The EELS spectrometer ENFINA of Gatan is installed on the JEOL-2010 at PSI.

2.4.2 Data Analysis

For the small defect clusters and dislocation loops, the micrographs at Magnification from 200K× to 300K× under WBDF (g, 5g) were selected to evaluate the volume number density. For the small helium bubbles, magnification between 300K× to 500K× were used.

To obtain quantitative information, the defect clusters and dislocation loops were counted and measured from different areas of each sample under exactly the same WBDF condition. In general, for each sample, more than 300 small defect clusters and 100 dislocation loops were measured to determine the size distribution and the mean size. The number density of defect clusters was counted by using the imaging software 'Fiji Is Just ImageJ' [153] as shown in Fig.2.10. With Fiji a JPEG digital format micrograph was used.

The data obtained on different types of defects, such as the number of defects and their size were taken to obtain final results on the volume number density of a certain type of defects.

Besides, the width of defect-free channeling and deformation twinning was also statistically measured by using 'ImageJ' software.

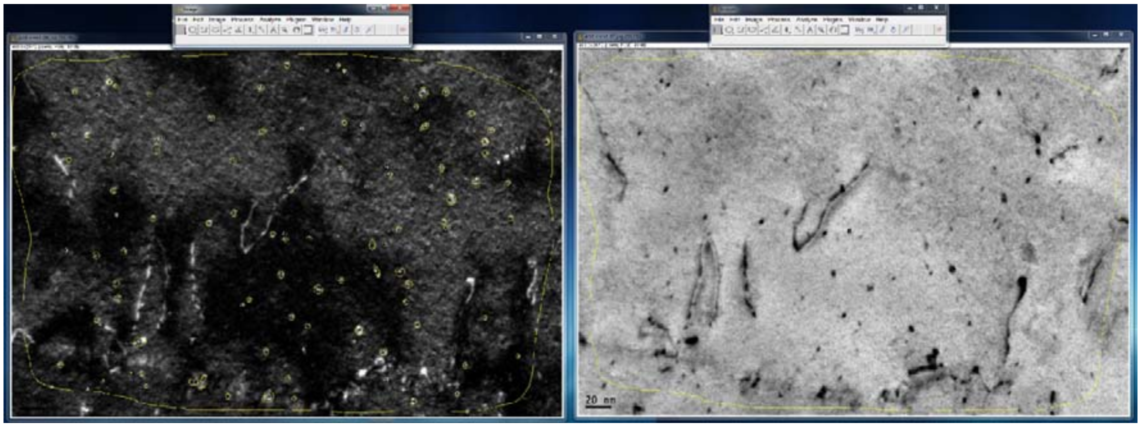

Fig 2.10: Defect clusters counting by comparing BF and WBDF images of the same selected region in ImageJ software.

2.5 TEM-lamella sample preparation with Focused Ion Beam (FIB) technique

Several TEM sample preparation methods can be exploited to produce good quality samples. Ion milling is one of generally these techniques. The advantage of this technique is relatively simple and yields good quality samples. However, this method is time-consuming (several hours to prepare one sample). In addition, the ion-induced displacement damage cannot be avoided, which can be confounded with radiation-induced damage and confuses the result. Another common exploited technique is jet electro-polishing method, which is more efficient than other way since a group of specimens can be prepared simultaneously. And only 1-3 min is utilized for each specimen in the final jet electro-polishing. Nevertheless, for the radioactive FM steel sample, a 0.8 or 1 mm disc of investigated material needs to be punched out and embedded into a 3 mm disc of stainless steel to reduce the radioactivity and magnetism during TEM observation.

When deformed microstructures are to be investigated, such as those in small necking area or even brittle fracture specimen without measurable plastic deformation, TEM lamella sample can be extracted only by using focused ion beam (FIB). FIB technique is commonly used to prepare samples for TEM, which requires very thin samples, typically below 100 nanometers. In addition, the nanometer-scale resolution of the FIB allows the exact thin region to be chosen, e.g. grain boundaries (GBs) and fracture surface.

The FIB facility used is a Zeiss NVision 40 situated in a radioactive lab. This device consists of a SEM and FIB. SEM column is installed upright and FIB column is fixed with 54° to the SEM column in such a way that electron and ion beams are crossing at the specific working distance (5.1 mm in this work) as shown in Fig. 2.11. Automatized specimen stage with tilt and rotation options is allowed to move the sample with nanometric precision. The NVision 40 at PSI operates between 1 keV and 30 keV Ga^+ with currents between 0.1 pA and 45 nA. The highest spatial resolution of the ion beam is 4 nm at 1 pA. Usually, the FIB is operated at 30 keV for rough milling and thinning of the lamella to the required thickness and for final polishing at 2 keV.

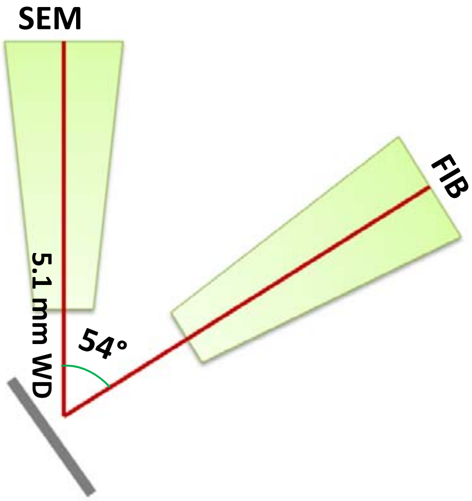

Fig 2.11: Schematic of FIB device together with SEM.

To prepare a TEM lamella sample, the common procedure is described as follows:

1. Protect the sample surface with carbon layer as shown in Fig. 2.12 (a), the area is between 10×2 to 30×2 μm^2 and deposit minimum 1 µm thickness. FIB energy used is 30 kV and FIB current conducted is ranging between 80 to 300 pA which depends on the deposition area.
2. Use trapezoids to mill 3 sides around the deposited quadrangle as shown in Fig. 2.12 (b), FIB energy used is 30 kV and FIB current conducted is 6.5 nA or 13 nA. The milling depth is 25 µm.
3. Cut lamella in transverse direction as shown in Fig. 2.12 (c). Make sure FIB cut had penetrated through the lamella by using visual control.
4. Move the micromanipulator needle to approach lamella with the help of SEM and FIB view to the lamella. Then weld the micromanipulator needle to the lamella.
5. After welding the micromanipulator needle to the specimen, do the final cut to be able to lift the lamella out.
6. Move the needle with lamella carefully to the ‘Platinum half-moon grid’. Bring the needle with the specimen in the position of one of the fingers on the ‘half-moon grid’ to weld. Approach the lamella as close as possible, but not really touch the ‘Platinum half-moon grid’ as shown in Fig. 2.12 (d) and (e).
7. After welding the lamella to ‘Platinum half-moon grid’, do very thin cut to disconnect the needle from the specimen.
8. After the lamella is in the safe position on the ‘Platinum half-moon grid’, tilt the sample to 54 ° with SEM column and thin the lamella to 1 µm. The FIB energy used is 30 kV and FIB current conducted is between 300 pA to 3 nA. The thinner the thickness of lamella is cut to, the smaller the FIB current is utilized.
9. Further tilt the lamella to 56 ° with SEM column and thin the lamella to the final thickness between 120-150 nm for flash electropolishing as shown in Fig. 2.12 (f). The FIB energy used is 30 kV and FIB current conducted is between 40 pA to 300 pA.

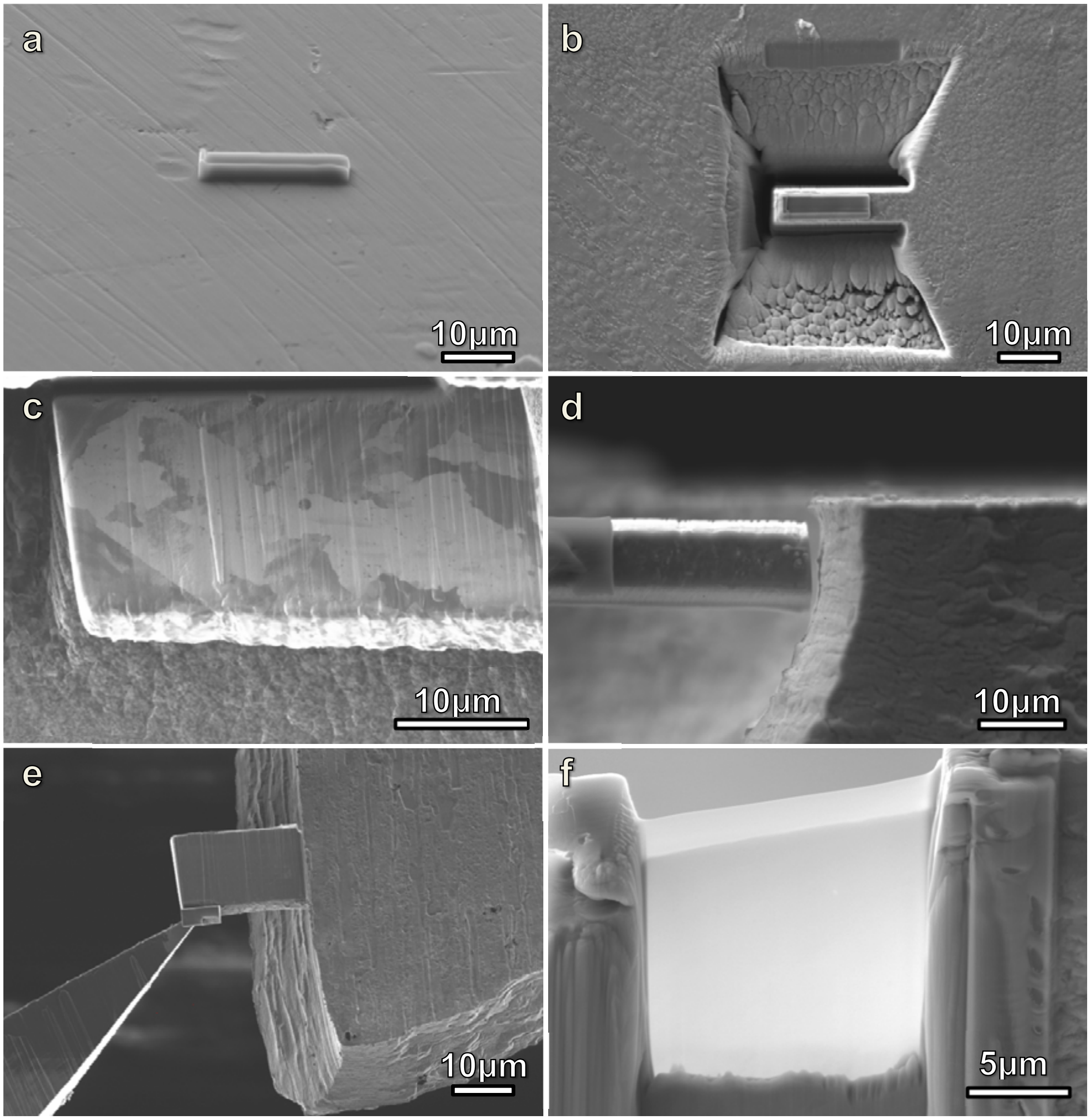

Fig 2.12: The basic procedure of TEM lamella sample preparation by FIB: carbon deposition (a) coarse cutting (b) transverse direction cutting (c) welding to platinum grid (d) and (e) lamella image after final polishing by FIB (f).

In recent work, TEM lamella sample preparation was exploited in 3 kinds of typical sites as shown in Fig.2.13 (a)-(c) on the specimens: un-deformed area, deformed area and brittle fracture surface area.

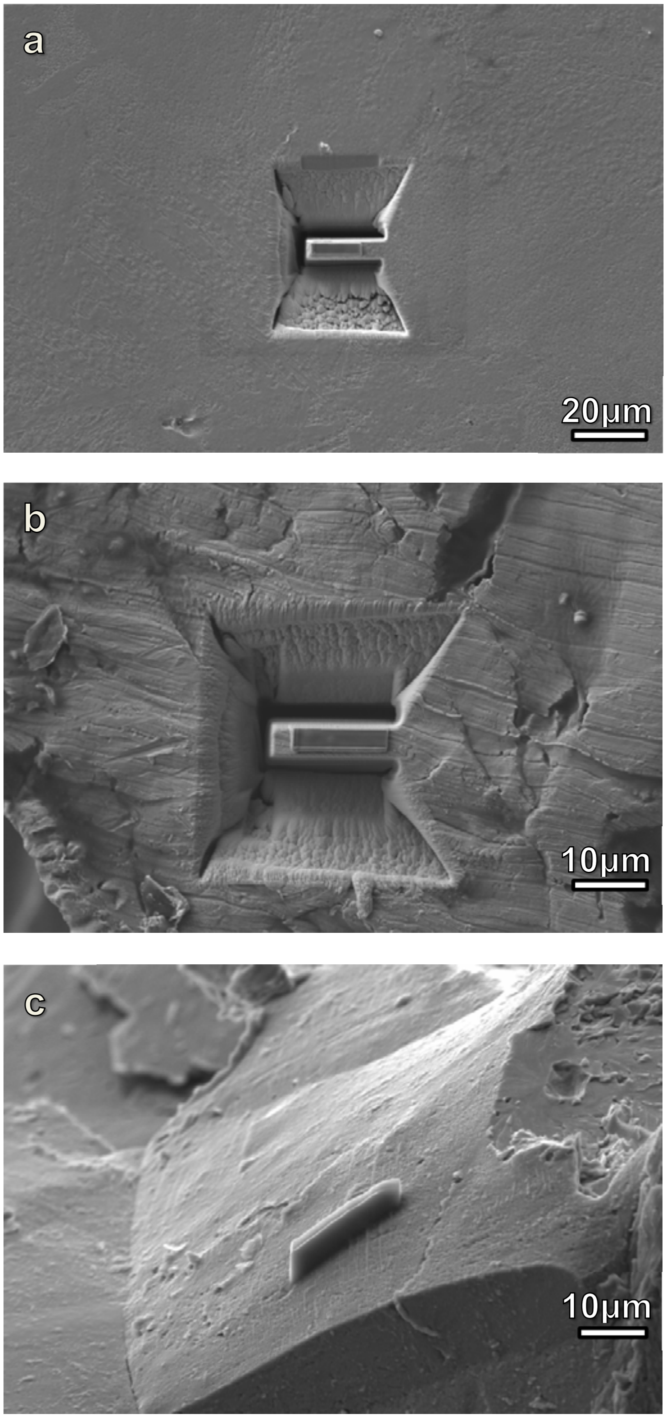

Fig 2.13: TEM-lamella sample preparation in three typical sites: un-deformed area (a) deformed area (b) and brittle fracture surface area (c).

Although the pros of FIB TEM lamella technique is obvious, the drawbacks to FIB sample preparation are the surface damage by Gallium ion, which produce noticeable effects when using techniques such as high resolution “lattice imaging” TEM or electron energy loss spectroscopy (EELS) or investigation on irradiation induced defects. This damaged layer can be minimized by FIB milling with lower beam voltages, or by further milling with a low-voltage argon ion beam after completion of the FIB process. As a matter of fact, 30 keV ions severely damage the surface of the lamella. And the defects produced by FIB intervene with the radiation induced defects and confuse the investigation in TEM. According to “Stopping Range of Ions in Matter” (SRIM) calculations thickness of the layer damaged by 30 keV Ga ions in FIB is up to 20 nm [154]. Thus a final polishing with 2 keV Ga ions help reduce the number of FIB defects to some extent, however, the surface damage cannot be fully removed because of the damage of the Ga ions.

2.6 Flash electropolishing

In order to completely remove the damage layer by FIB, a so-called flash electropolishing method was developed. The flash electropolishing set-up is shown in Fig. 2.14 (a), a tweezer as anode clamping the grid with a lamella is immersed in electropolishing solution of perchloric acid in ethanol. The solution consists of 3%-7% perchloric acid depending on which kinds of materials electropolished. A 1 mm thick stainless plate is bent to a circle shape as cathode. The voltage can be applied for a much shorter time with millisecond precision control by using a time relay connected to the power supply as shown in Fig. 2.14 (b). The common used parameters for flash electropolishing is:

- The 20-23 V applied voltage
- 0.2-0.5 seconds polishing time depending on the initial thickness of sample.
- -20 to -30 °C of electropolishing solution
- 120 to 200 nm initial thickness of TEM lamella sample fabricated by FIB

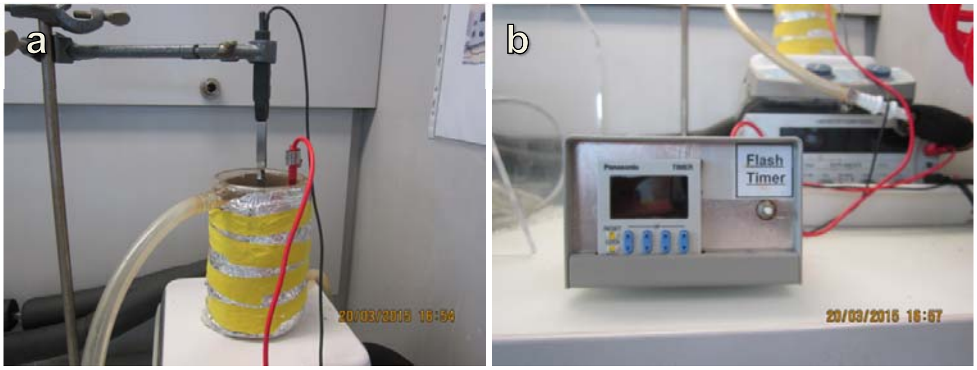

Fig 2.14: Home made electropolishing set-up (a) and the time relay to control electropolishing time (b).

Fig. 2.15 presents TEM pictures of lamella of irradiated F82H before and after flash electropolishing. We can see that the high density of FIB-induced defects completely cover the image, so that irradiation induced defects are impossible to be distinguished in Fig. 2.15 (a), while in Fig. 2.15 (b) FIB induced damages are removed after electropolishing and the investigation on the radiation induced defects and defect-free channeling is feasible from such high quality specimen, irradiation-induced small defect clusters, dislocation loops and pre-existing dislocation lines are able to be distinguished.

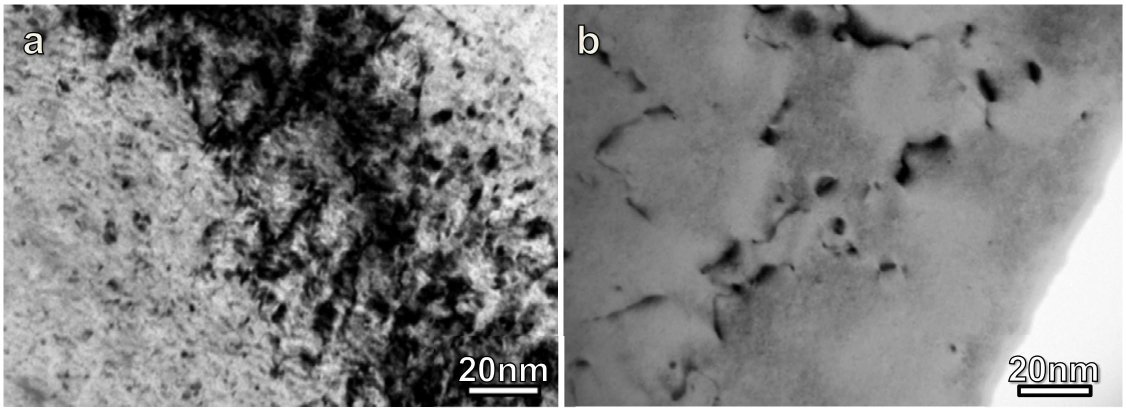
a
20nm
b
20nm

Fig 2.15: TEM images of TEM lamella sample before (a) and after (b) flash electropolishing.

3. Results

3.1 Mechanical testing

The results of the performed mechanical tests are presented below. The results are divided into tensile testing and hardness measurement. Three different FM steels, F82H, Eurofer97 and MANET II, irradiated under various irradiation conditions ranging from 10.7 to 19.8 dpa were tensile tested at different temperatures. The tensile stress-strain curves and the corresponding SEM images of fracture surface are shown in this section. Vickers hardness was measured on the electropolished tensile specimens before tensile testing. The hardness results ($H_{v0.5}$) on F82H, Eurofer97 and MANET II in different conditions are given.

3.1.1 Tensile tests and SEM observations of fracture surface

Since the goal of the present work is to understand the deformation mechanisms of martensitic steels irradiated in spallation neutron sources, four F82H specimens with different irradiation conditions (see Table 2.3) were selected and tested at different temperatures. The choice was based on previous tensile test results of martensitic steels irradiated in STIP [78, 155, 156]. Figure 3.1 presents the engineering stress-strain curves of these specimens. Although all the specimens exhibit significant hardening and loss of ductility as compared with the unirradiated specimens, they manifest different deformation behavior under different irradiation and test conditions. The specimen with the lowest dose of 10.7 dpa possesses pretty large total elongation at RT, although uniform elongation decreased to less than 1%. However, at the higher irradiation dose of 15.8 dpa, the specimen tested at RT failed in elastic regime without any plastic deformation, which implies very brittle fracture. The two specimens demonstrate a clear irradiation dose and He concentration dependence of fracture behavior of the steel. It is also known that the fracture behavior of materials depends strongly on test temperature. For example, it can be seen in Figure 3.1 that the other specimen at a similar irradiation dose of 15.2 dpa shows a small amount of ductility at 250 °C. At a high dose of 19.6 dpa, F82H steel was found to be brittle when tested at even higher temperatures.

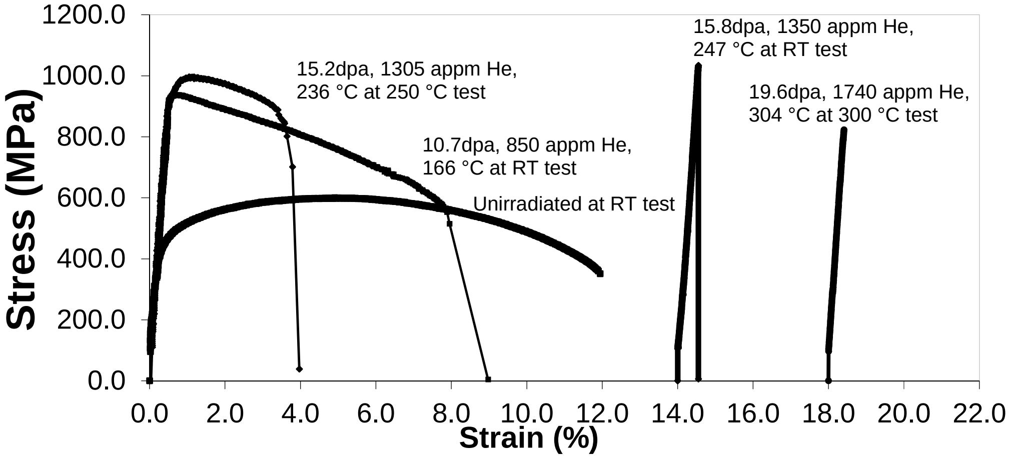

Fig 3.1: Tensile engineering stress-strain curves of F82H specimens in different irradiation and test conditions as indicated.

The fracture surfaces of the irradiated specimens are shown by SEM micrographs in Figs. 3.2 and 3.3 Figs. 3.2(a) – 3.2(d) are for the specimen of 10.7 dpa and tested at RT. It can be seen that the specimen developed a strong necking before breaking. A reduction of area of 61.5% was deduced from the micrograph in Fig. 3.2(a). On the fracture surface many large dimples were observed (Figs. 3.2(b) and 3.2(c)), which indicates a ductile fracture mode of this specimen. However, quasi-cleavage fracture was also observed (Fig. 3.2(d)). The fracture surface of the specimen of 15.2 dpa and tested at 250 °C exhibits a mixed ductile and quasi-cleavage fracture mode (Figs. 3.2(e) – 3.2(h)). Fig. 3.2(e) shows a 25% reduction of the cross-section, less reduction as compared to the 61.5% of the 10.7 dpa specimen. Although the middle part of the specimen presents dimple ductile fracture (Fig. 3.2(f)), both the right and left edge parts were fractured in a quasi-cleavage mode (Figs. 3.2(g) and 3.2(h)). It was observed that the failure of tensile tested specimens started with crack propagation from edge surfaces where micro-cracks were produced by EDM cutting. This implies that cleavage cracks were developed first from the edges, while the middle part was torn due to reduced cross- section. However, the dimples are smaller and shallower as compare to that of the 10.7 dpa specimen (Figs. 3.2(b) and 3.2(c)). Both the specimens of 15.8 dpa/tested at RT and 19.6 dpa/tested at 300 °C show brittle fracture without necking and area reduction (Figs. 3.3(a) and 3.3(c)). However, their fracture surfaces look slightly different. The specimen of 15.8 dpa/tested at RT failed in a mixed transgranular cleavage and interguranular fracture mode (Fig. 3.3(b)). Although the specimen of 19.6 dpa/tested at 300 °C also failed in a mixed transgranular cleavage and interguranular fracture mode, the fracture is dominant in intergranular mode (Fig. 3.3(d)).

Fig. 3.4 shows the stress-strain curves of tensile test of Eurofer97 and MANET II and the corresponding fracture surfaces. Fig. 3.4 (a) presents the engineering stress-strain curve for a Eurofer 97 specimen of 19.8 dpa and test at RT. This specimen also exhibits significant hardening and loss of ductility as compared with the unirradiated specimens. The result shows that the total elongation was about 1.5% after yielding but no necking appeared before failure. The fracture surface, as shown in Fig. 3.4 (b), indicates that the fracture mode is dominantly intergranular accompanied with some transgranular cleavage. However, some out-of-plane micro-cracks are observed on the fracture surface. Fig. 3.4 (c) presents the engineering stress-strain curves for MANET II specimen with irradiation condition to 19.8 dpa and test temperatures at 300 °C. This specimen also exhibits significant hardening and loss of ductility as compared with the unirradiated specimens. The result shows that a certain necking level was still kept before failure. However, the stress-strain curve indicates a prompt necking after yielding without obvious work hardening with onset of necking at a strain smaller than 1 %. In Fig. 3.4 (d), the fracture surface of this specimen shows that the fracture mode is dominantly intergranular with transgranular cleavage fracture accompanied and dimple-ductile fracture in a small portion of the fracture surface. In contrast to the result of Eurofer 97 irradiated to 19.8 dpa and tested at RT, this MANET II specimen with similar irradiation conditions exhibits a small part of dimple-ductile fracture besides intergranular and transgranular cleavage fracture after 300 °C tensile test. The 2% total elongation is deemed to be from the dimple-ductile fracture part.

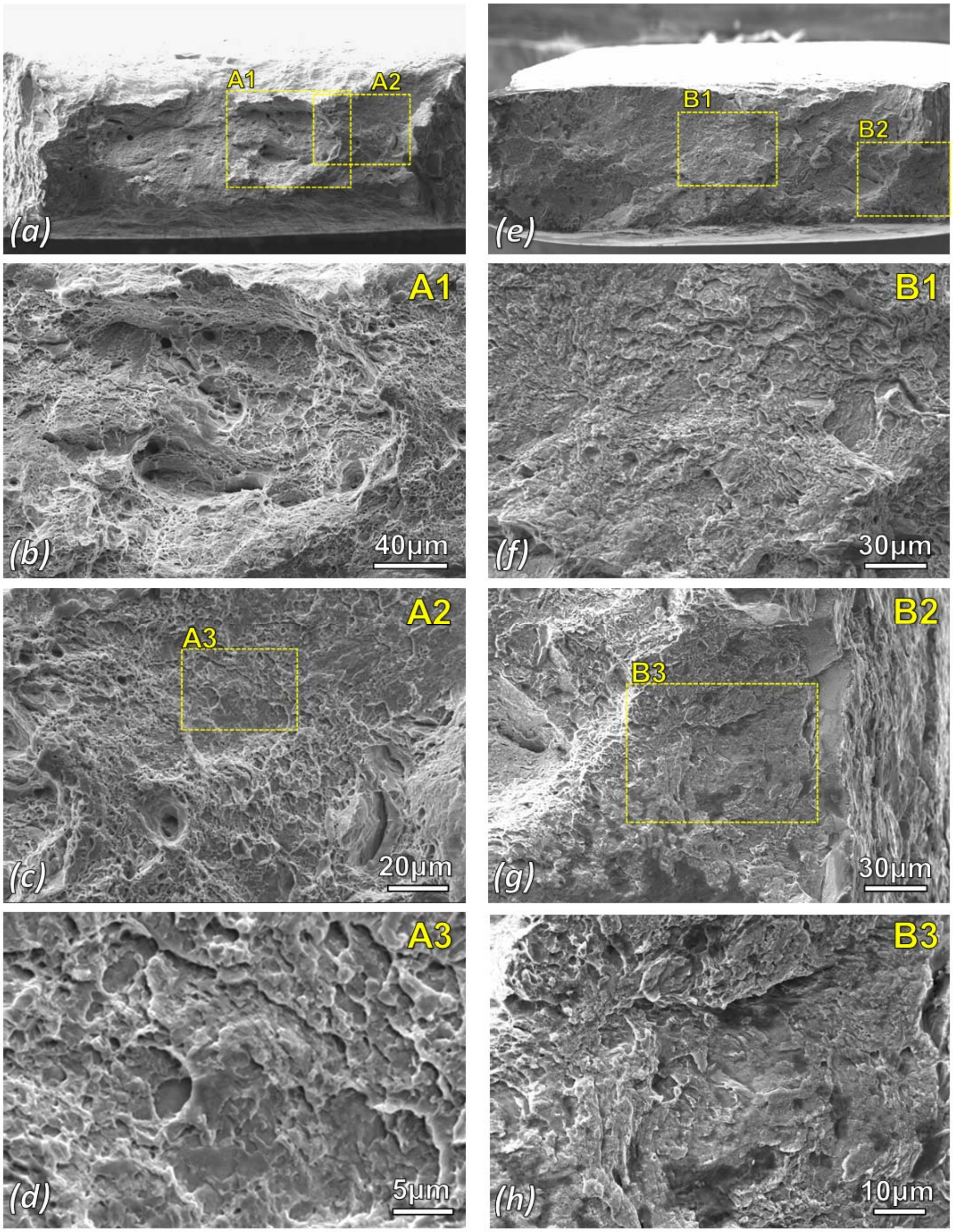
(a)
A1
A2
(e)
B1
B2
A1
(b)
40μm
B1
(f)
30μm
A2
A3
(c)
20μm
B2
B3
(g)
30μm
A3
(d)
5μm
B3
(h)
10μm

Fig 3.2: SEM images of fracture surfaces of F82H specimens in different irradiation and test conditions: (a) – (d) 10.7 dpa and tested at RT, (e) – (h) 15.2 dpa and tested at 250 ℃. (b) and (c) are areas A1 and A2 in (a), respectively. (d) is area A3 in (c). (f) and (g) are areas B1 and B2 in (e), respectively. (h) is area B3 in (g).

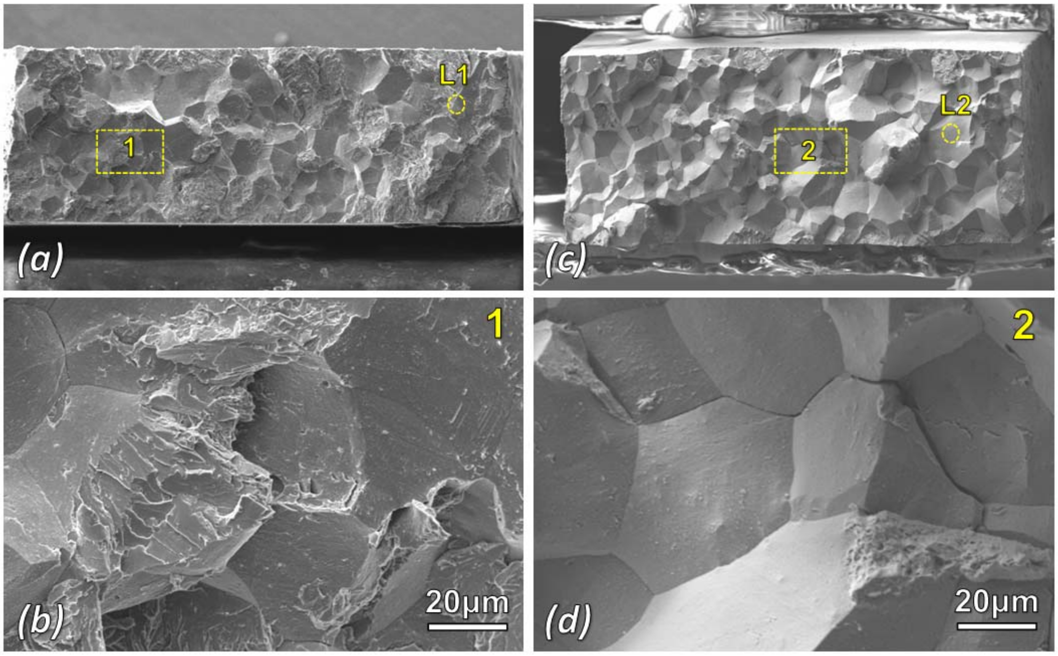

Fig 3.3: SEM images of fracture surfaces of F82H specimens in different irradiation and test conditions: (a) and (b) 15.8 dpa and tested at RT, (c) and (d) 19.6 dpa and tested at 300 ℃. (b) and (d) are areas marked in (a) and (c), respectively. Spots L1 and L2 indicate the locations where TEM lamellas were extracted for microstructural analysis.

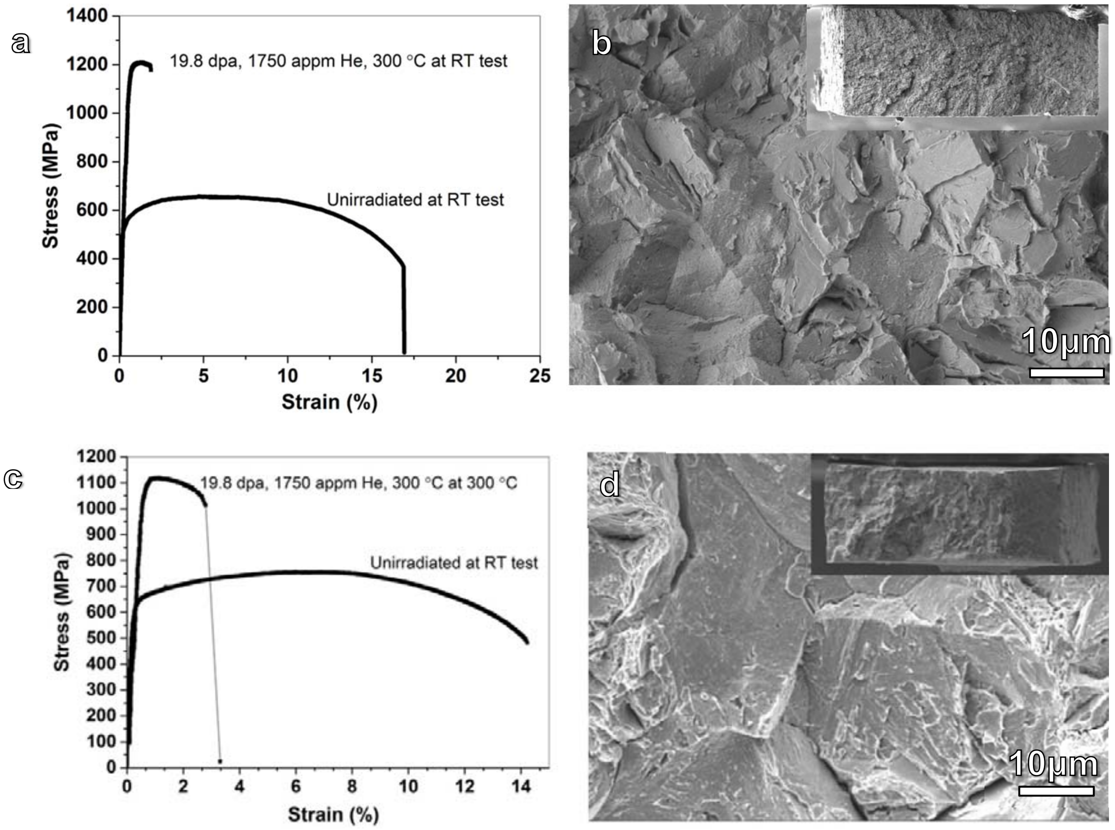

Fig 3.4: Stress-strain curves and corresponding fracture surfaces of Eurofer 97 (a) and (b) irradiated to 19.8 dpa and tested at RT and MANET II (c) and (d) irradiated to 19.8 dpa and tested at 300 °C. The inset shows the fracture surface in low magnification.

3.1.2 Hardness Measurement

Vickers hardness of the irradiated F82H, Eurofer97 and MANET II specimens was measured at 500 g ($H_{v0.5}$) load. All the specimens were mechanically polished and electro-polished as illustrated in experimental methods 2.1.3 before hardness measurement. Irradiation dose difference along the specimen gage length needs to be considered due to the Gaussian distribution profile of the proton beam. Therefore, the values of hardness are given on low dose and high dose ends respectively. The results of hardness measurement are listed in Table 3.1 and presented in Fig. 3.5. In Fig. 3.5, the hardness values are plotted as a function of irradiation dose. It can be seen that hardness values of both F82H and MANET II increase with increasing irradiation dose.

Table 3.1 The results of hardness measurement of F82H, MANET II and Eurofer 97 in different irradiation conditions.

Sample	Number	H_v0.5 (Low Dose side)	H_v0.5 (High Dose side)	H_v0.5
F82H	Inactive	-	-	208
	2-ST-K24	296 (6.1dpa)	309 (8.7dpa)	-
	2-ST-K23	320 (9.5dpa)	353 (12.9dpa)	-
	2-ST-K22	362 (13.9dpa)	379 (17.7dpa)	-
	2-ST-K20	394 (18.1dpa)	401 (20.4dpa)	-
Manet-II	Inactive	-	-	263
	2-ST-O16	351 (6.1dpa)	364 (8.7dpa)	-
	2-ST-O19	360 (9.5dpa)	382 (12.9dpa)	-
	2-ST-O17	437 (18.5dpa)	446 (20.4dpa)	-
Eurofer97	Inactive	-	-	227
	2-ST-IJ10	407 (18.5dpa)	489 (20.4dpa)	-

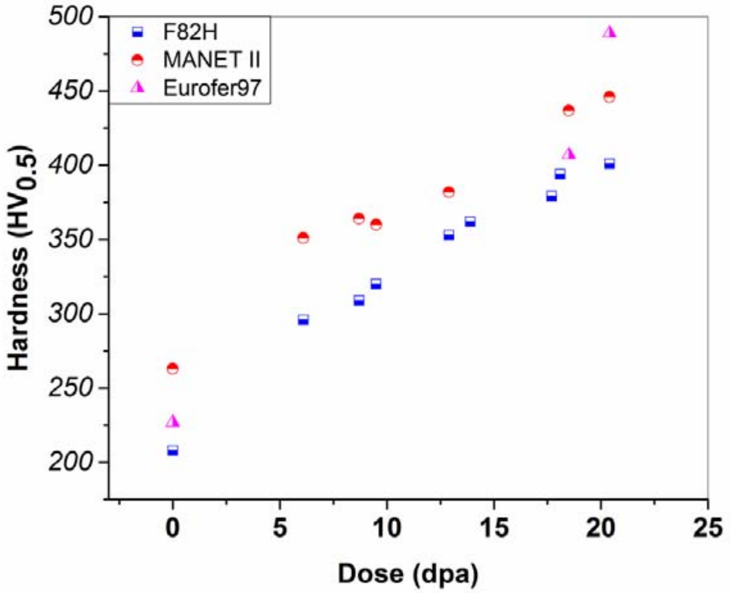

Fig 3.5: Hardness versus dose of irradiated F82H, MANET II and Eurofer97 specimens.

A distinct trend for all three FM steels (F82H, MANET II and Eurofer97) can be observed, the hardness for the specimens continuously increases with dose and helium contents. There is no saturation in the increase of hardness value up to the highest irradiation dose (20.4 dpa). For F82H specimens, the trend of increase of hardness values (ΔH_V) corresponds to the increase of yield stress ($\Delta\sigma_y$) from tensile test.

3.2 Micro-crack initiation and propagation

The results of crack initiation and propagation of unirradiated SP specimens tested at RT and liquid nitrogen (LN2) temperature are presented in &3.2.1. The results of crack initiation and propagation of irradiated tensile specimens in different irradiation conditions and tested at RT are shown in &3.2.2.

3.2.1 Successive small punch tests and SEM observations

Small punch (SP) samples of T91 steel were used for successive SP tests at RT and liquid nitrogen (LN2) temperatures. SEM fractography observations of SP samples taken at different deformation levels were performed. Fig. 3.6 (a) and (b) shows the load-displacement curves of test at RT and LN2 temperature respectively. The unloading points are marked in the figure. The fracture surfaces of specimens tested at RT and LN2 temperature are presented in fig. 3.6 (c) and (d). The fracture mode of specimen tested at RT is dominant with ductile-dimples as shown in fig. 3.6 (c), while the specimens tested at LN2 is dominant with transgranular-cleavage as shown in fig. 3.6 (d). Figure 3.7 shows the micro-cracks on the surface of the SP sample at the unloading point 4 of Fig. 3.6 (a). In Fig.

3.7, we can observe that cracks initiate from the micro-voids, which occasionally contain inclusion particles.

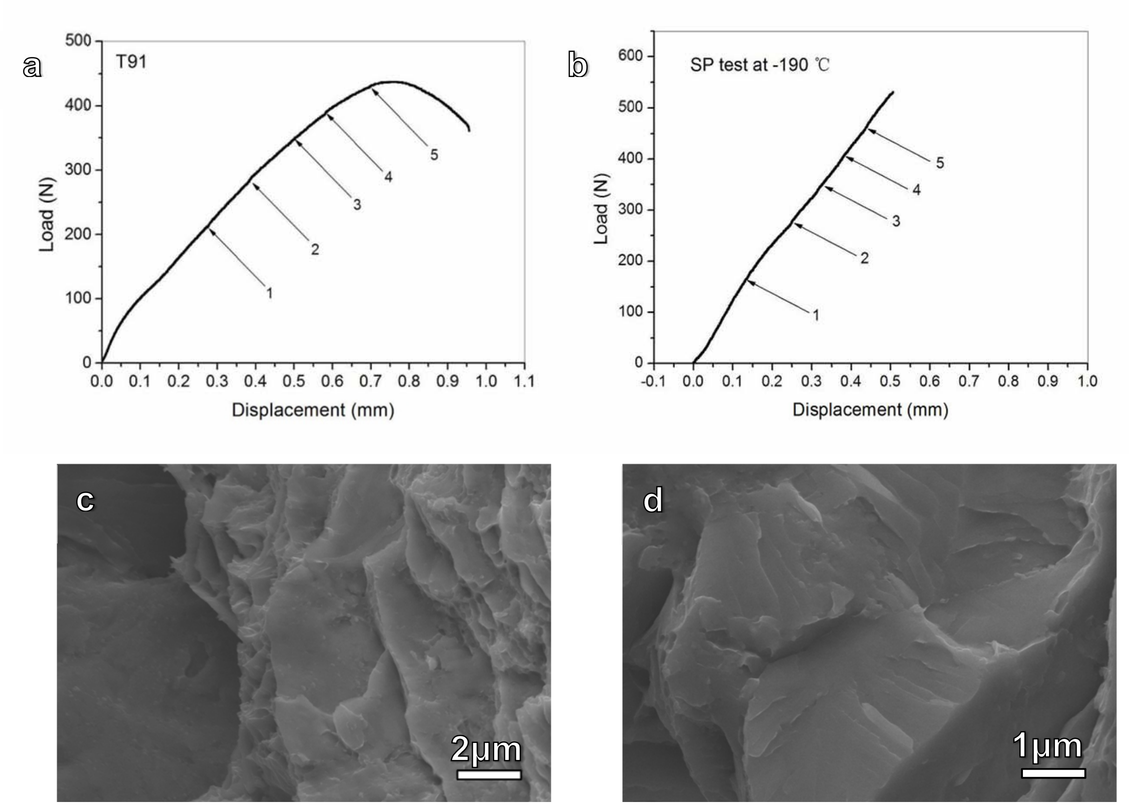

Fig. 3.6: The load-displacement curves of SP tests at RT (a) and -190 °C (b).

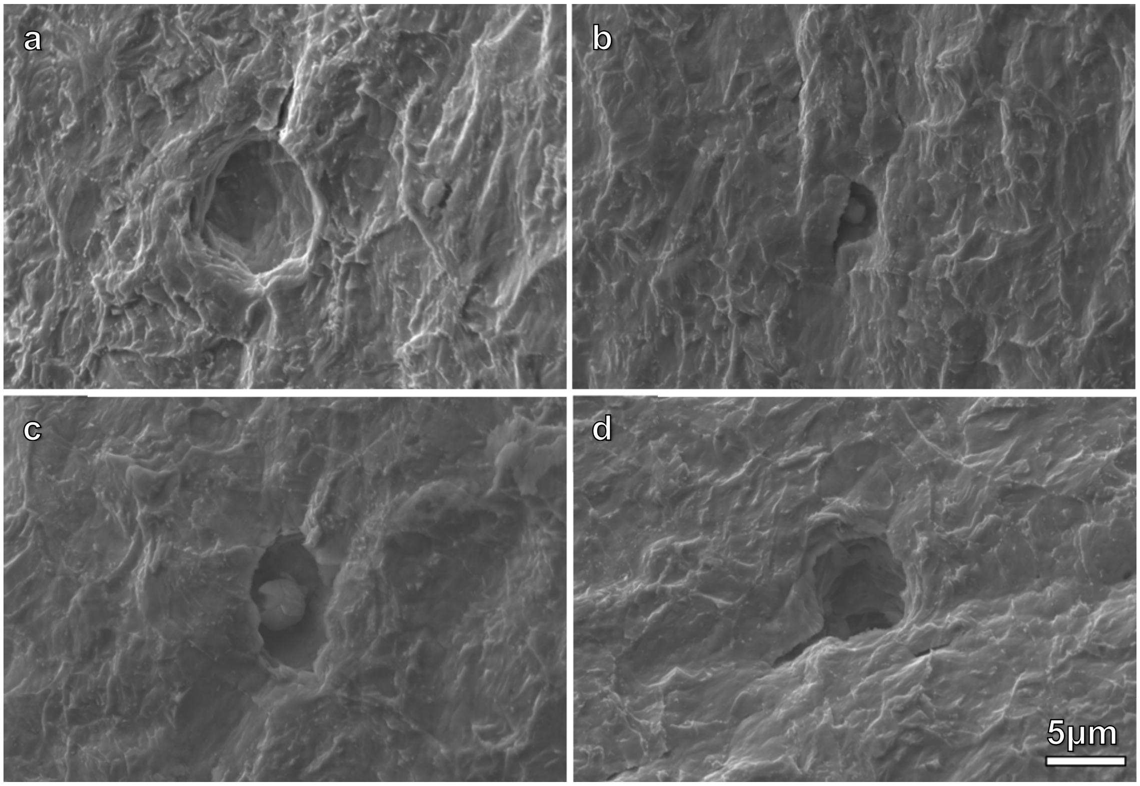

Fig.3.7: Micrographs of T91 at unloading point 4 of Fig 3.6 (a).

Figure 3.8 presents the micro-crack SEM images of SP sample at the unloading points 3-5 of Fig 3.6(a). From this figure, we can see a micro-crack initiating on the top and bottom of a micro-void and propagating along slip bands. The crack propagated along two ends simultaneously and the crack opened as the micro-void enlarged during test.

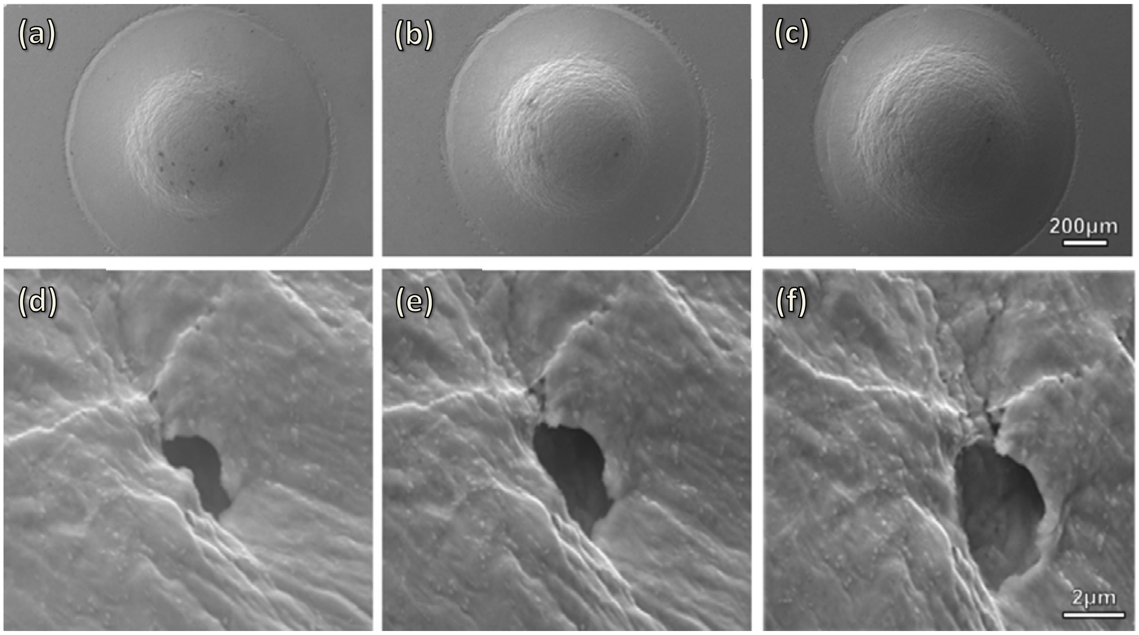

Fig 3.8: Illustration of SEM observation at different interrupted points 3-5 (a)-(c) in low magnification and (d)-(f) in high magnification in the successive SP test of Fig 3.6 (a).

The fracture mode of specimens tested at low temperatures is brittle fracture. Fig 3.6(b) shows the load-displacement curve of SP sample tested at -191℃. The unloading points are marked as shown in the figure. Figure 3.9 presents the micro-crack SEM images of the SP sample in the unloading points 3-5 of Fig 3.6(b). It seems that cracks initiate mostly at grain boundaries. The crack propagation behavior at different unloading points is illustrated in Figure 3.9. From this figure, we can see that the micro-crack initiates from boundary area and propagated along boundary in both directions simultaneously. The crack opening displacement becomes wide during propagation.

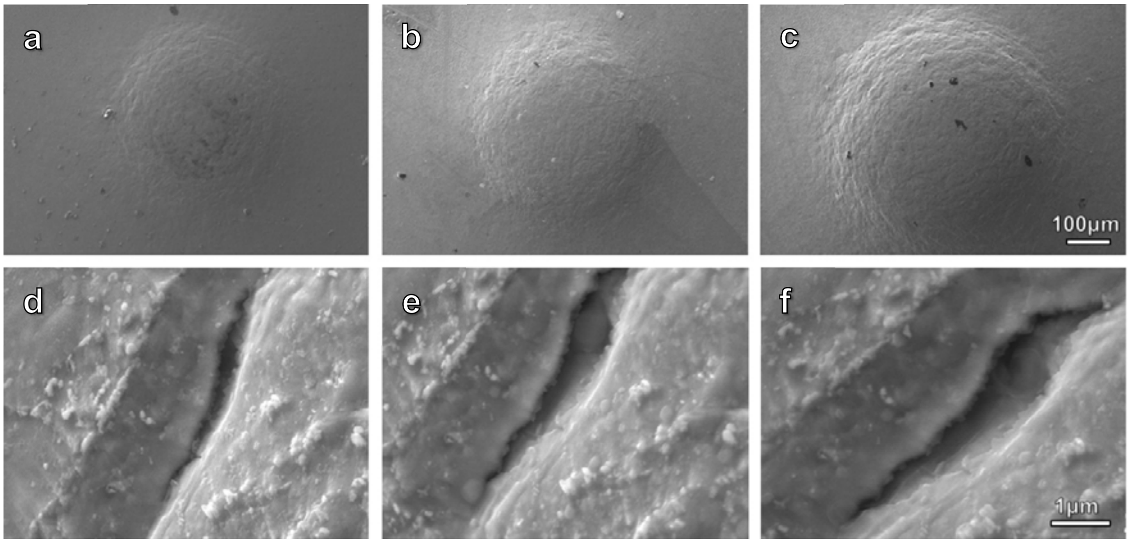

Fig. 3.9: The crack micrographs of T91 at different unloading points 3-5 (a)-(c) in low magnification and (d)-(f) in high magnification of Fig 3.6(b).

3.2.2 Successive tensile tests and SEM observations

The previous successive SP tests and SEM observations were carried out as a tentative experiment on unirradiated specimens to gain insight on the micro-crack initiation and propagation behavior. Nevertheless, a successive SP test was difficult to resume because the specimen position in the clamping system should be always kept the same. In addition, the surface strain level at different unloading points, particularly at the positions of the observed cracks, is difficult to be precisely determined. Therefore, successive tensile tests were preferentially employed to investigate micro-crack behavior.

F82H

Crack initiation and propagation were investigated by SEM observations on F82H and MANET II, with small irradiated tensile specimens, in three irradiation conditions for F82H and two irradiation conditions for MANET II at RT. Experimental procedures were presented in 2.3.2. Fig. 3.10 illustrates the front and side surface in tensile specimen as well as the tensile stress-strain curve of a specimen of F82H irradiated to 11.1 dpa, 910 appm He at 174 °C. The tensile test was interrupted five times at strains of 0.3, 0.9, 2.2, 3.8 and 6% for SEM observations.

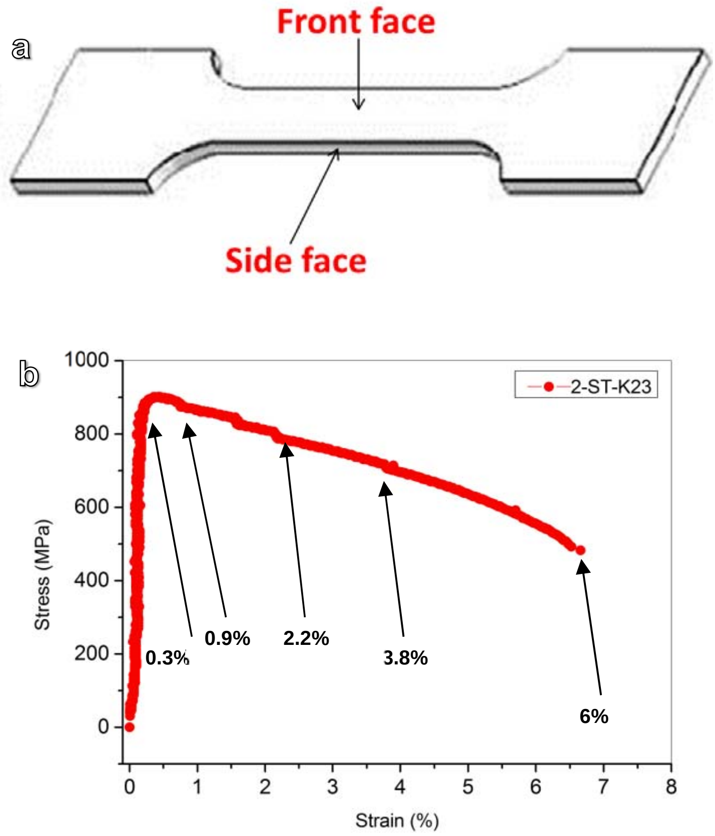

Fig. 3.10: (a) Illustration of front face and side in tensile specimen; (b) Successive tensile curve of F82H (Specimen 2-ST-K23) irradiated to 11.1 dpa, 910 appm He at 174 °C.

At 0.3% strain, slightly after yielding, grain boundaries micro-cracks were observed on the front face and near the edges, as shown in Fig.3.11.

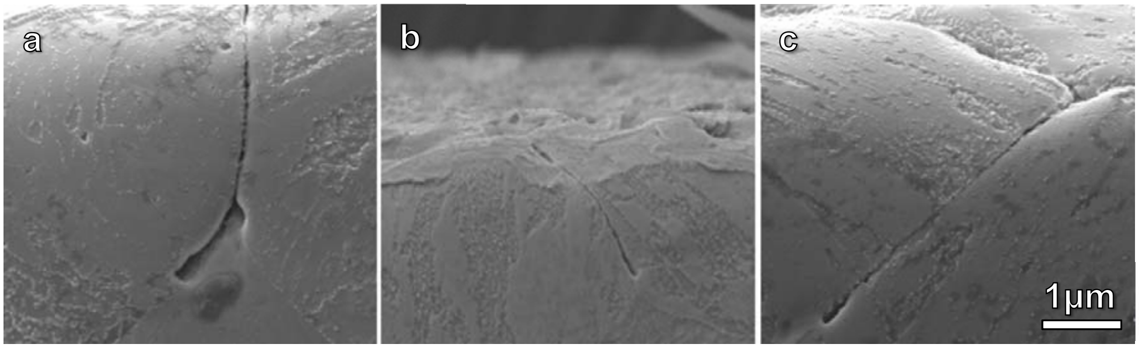

Fig. 3.11: SEM images showing intergranular cracks on front surface after 0.3% strain in F82H specimen 2-ST-K23, irradiated at 11.1 dpa.

Observations showed that these intergranular cracks occur on the side surface of both unirradiated and irradiated specimens; Fig 3.12 (a) and (b) correspond to irradiated and unirradiated specimen respectively. This crack initiation is attributed to the brittle layer produced by Electrical Discharge Machining (EDM) of the specimen.

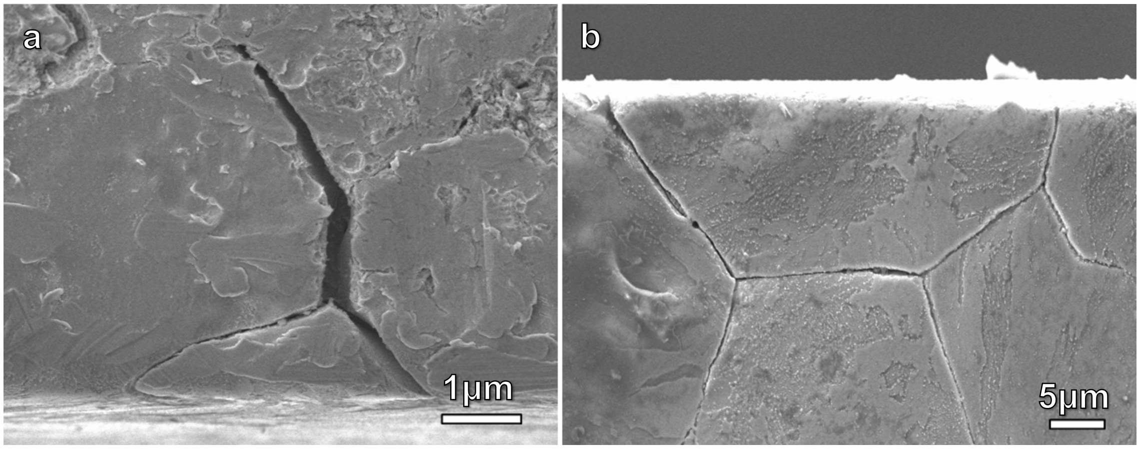

Fig. 3.12: Intergranular cracks observed on the side surfaces of (a) F82H specimen 2-ST-K23, irradiated at 11.1 dpa and (b) an unirradiared F82H specimens.

Fig. 3.13 presents the crack initiation and propagation behavior on different strain levels as marked in Fig. 3.10 with focus on one typical crack in edge region as shown in Fig. 3.13 (a). It should be noted that this crack developed within the necking region. The strain levels indicated in Fig. 3.10 are not the actual strains within the neck. From this figure, we can see that the micro-crack initiated in the edge area and propagated along a grain boundary with narrow crack opening displacement as shown in Fig. 3.13 (b). With the increase of strain level, the sharp crack tip reached grain boundary triple point (GBTP) junction as seen in Fig. 3.13 (c). The crack was arrested at GBTP, where it blunts under increasing deformation up to failure.

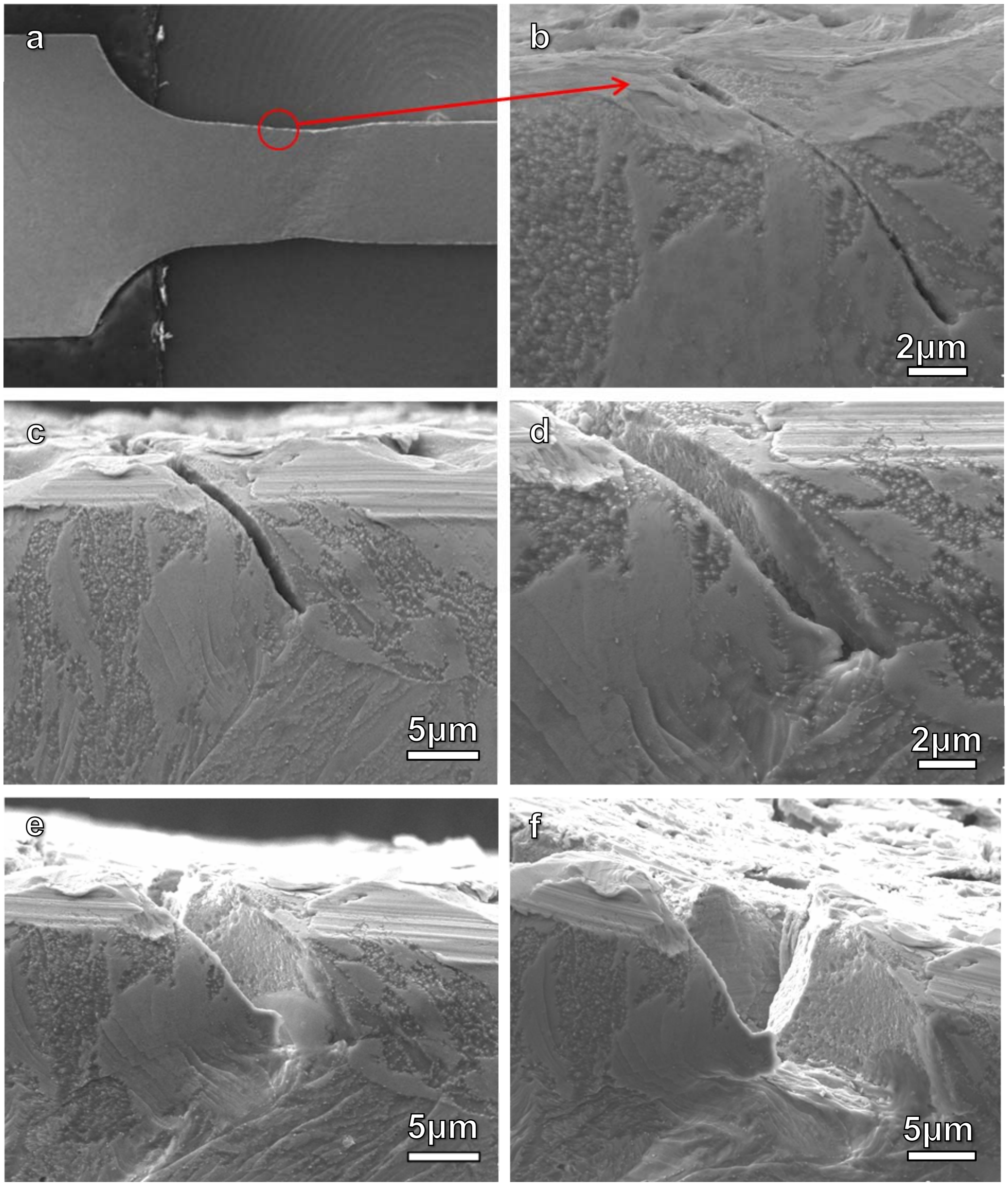

Fig 3.13: SEM images of evolution of micro-crack after different strains in F82H specimen 2-ST-K23, irradiated at 11.1 dpa.

The fracture surface and specimen front face are shown in figure 3.14 after failure. The crack described in figure 3.13 is indicated with a red circle in Fig.3.14 (a), which means that the final fracture was not induced by this crack. Figure 3.14 (b) shows the specimen surface image of edge area close to fracture surface. Figure 3.14 (c) and (d) present the fracture surface image in the edge area. The intergranular fracture region was observed in the edge area, while the ductile fracture surface was observed at a distance of about 5-10 µm away from the edge.

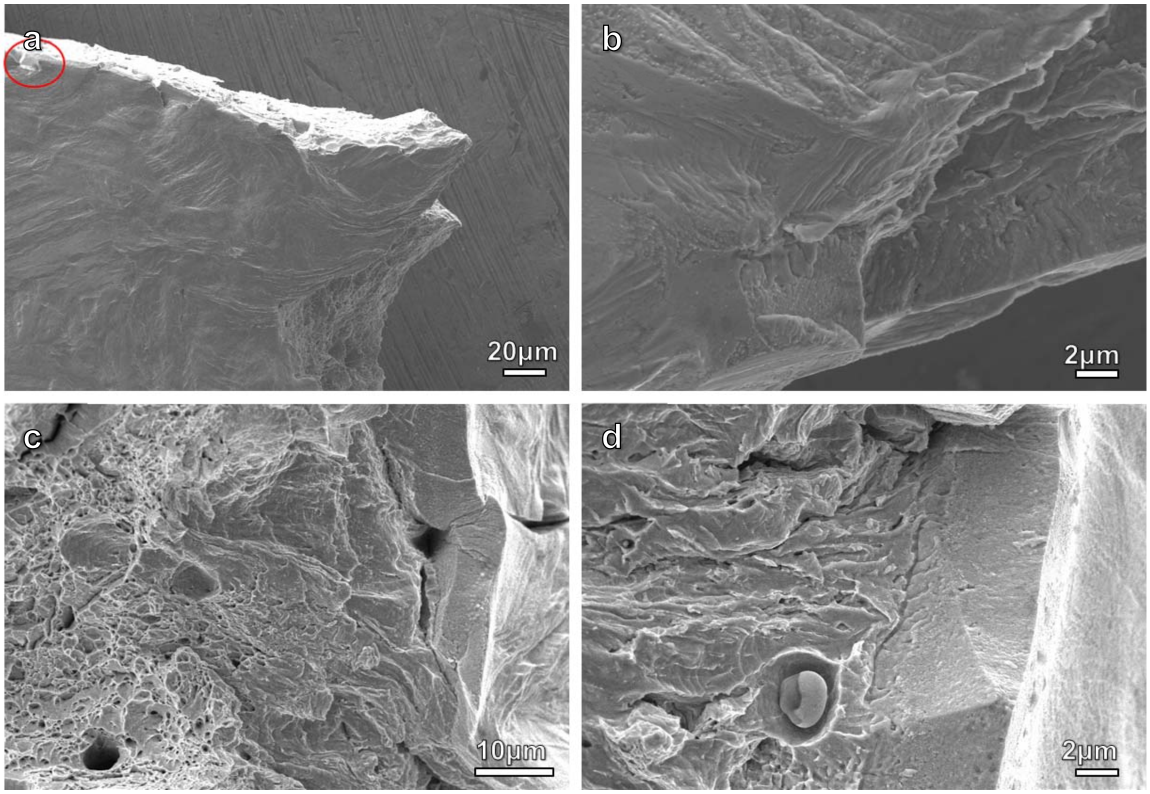

Fig 3.14: SEM images of specimen surface close to fracture surface (a)-(b) and fracture surface in the edge area (c)-(d) after fracture in F82H specimen 2-ST-K23, irradiated at 11.1 dpa.

With regard to the F82H specimen irradiated to 15.8 dpa in a successive tensile test, the specimen was so brittle that it fractured in the elastic regime. Therefore, for such kind of completely brittle sample, the crack initiation and propagation assessment cannot be investigated by successive tensile test. Fig. 3.15 presents the microstructures of fracture surface and sample surface. From Fig. 3.15 (a), it can be seen that the fracture mode is a mixture of intergranular and transgranular cleavage. No necking was observed. Fast crack propagation without blunting occurred during tensile test. Fig. 3.15 (b) presents a surface image of the specimen after fracture, few sharp intergranular cracks were observed in the edge area of the specimen around 100 µm away from the fracture surface.

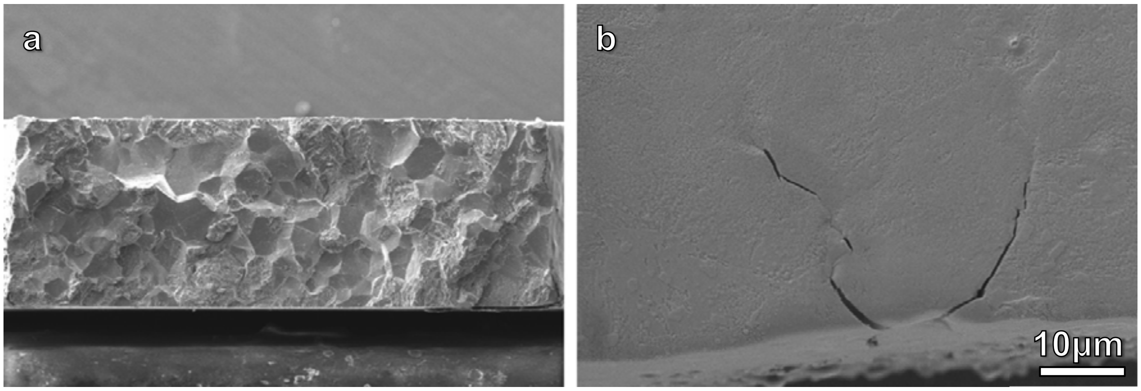

Fig 3.15: SEM images of fracture surface (a) and sample surface (b) of fractured F82H irradiated to 15.8 dpa.

MANET II

Since many intergranular cracks observed in the side surface layer in the F82H specimen initiated in brittle layer produced by EDM cutting, the surface layers of irradiated MANET II specimens were electro-polished before successive tensile test. Around 15-20 µm surface layer on each side were removed. The successive tensile tests and SEM observations were thereafter performed. Fig. 3.16 presents the results of MANET II irradiated up to 11.1 dpa / 910 appm He at 160 °C and tested at RT. The stress-strain curve of successive tensile test is shown in Fig. 3.16 (a). The interrupted points at different strain levels are indicated in the figure. Fig. 3.16 (b)-(e) present the macro-shape change on different strain levels. From the figure, one can see that the necking deformation appears in a small area.

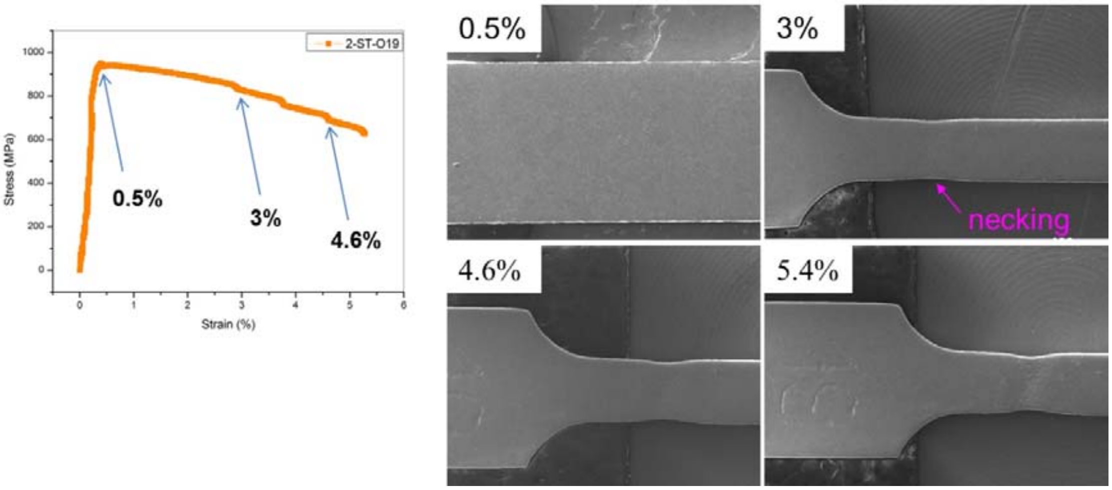

Fig 3.16: SEM images showing the shape of a MANET II specimen irradiated to 11.1 dpa at different tensile strain levels.

After straining to 3%, the side surface of the MANET II specimen was observed carefully, the microstructure is shown in Fig. 3.17. Interestingly, no micro-crack was observed, which supports the explanation of the origin of the micro-crack in the EDM-induced brittle layer.

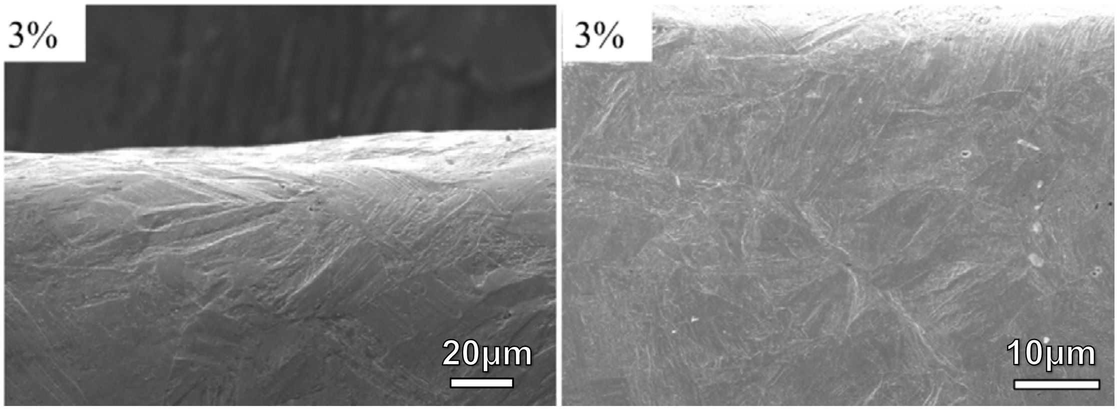

Fig 3.17: SEM images of side surface layer of MANET II irradiated to 11.1 dpa at 3% strain level.

At 4.6% strain, the side face of the specimen is as shown in Fig. 3.18. Micro-cracks were observed on this deformation level and their direction seems parallel to one direction of slip bands as indicated by dashed yellow lines.

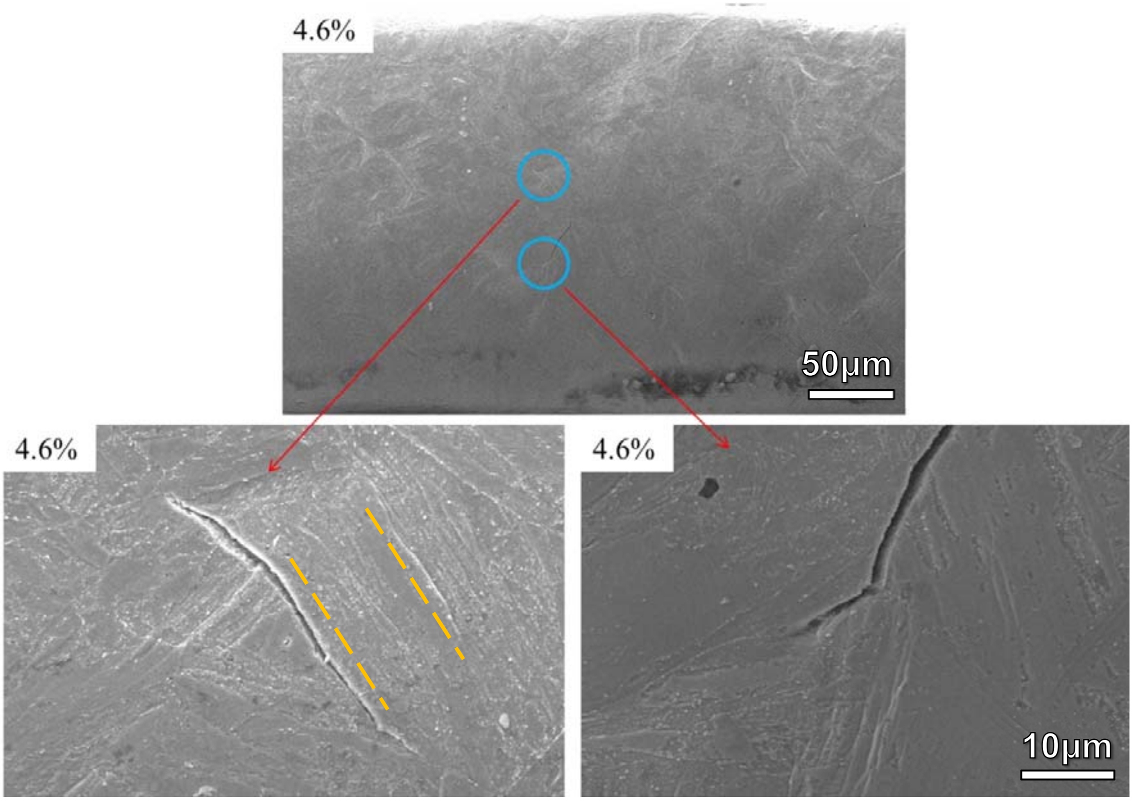

Fig 3.18: SEM images of side surface layer of MANET II irradiated to 11.1 dpa after 4.6% strain level.

3.3 Microstructure Evolution

3.3.1 Microstructures of as-irradiated F82H, Eurofer97, MANET-II

To study the effect of dose and helium concentration at different irradiation temperatures on the change of microstructures after irradiation and to gain insight into the materials response to mechanical loading on microscopic length scale, detailed microstructural analysis by transmission electron microscopy (TEM) was carried out for all fractured specimens in the as-irradiated state and after tensile test.

F82H

The microstructure of F82H prior to irradiation has the typical tempered martensitic laths containing dislocations with a density of approximately 1 × 10^{14} m^{-2} [157]. The average size of prior austenite grains (PAGs) is about 86 μm. $M_{23}C_6$ precipitates appear to be densely distributed and mostly located along the PAG and lath boundaries. The microstructure after irradiation to 12.3 dpa is presented in Fig. 3.19. A couple of lath boundaries are shown in Fig. 3.19 (a) and (b) as well as a prior austenite grain boundary is seen in Fig. 3.19 (a). In addition, a high density of precipitates and dislocation lines are observed in the microstructures.

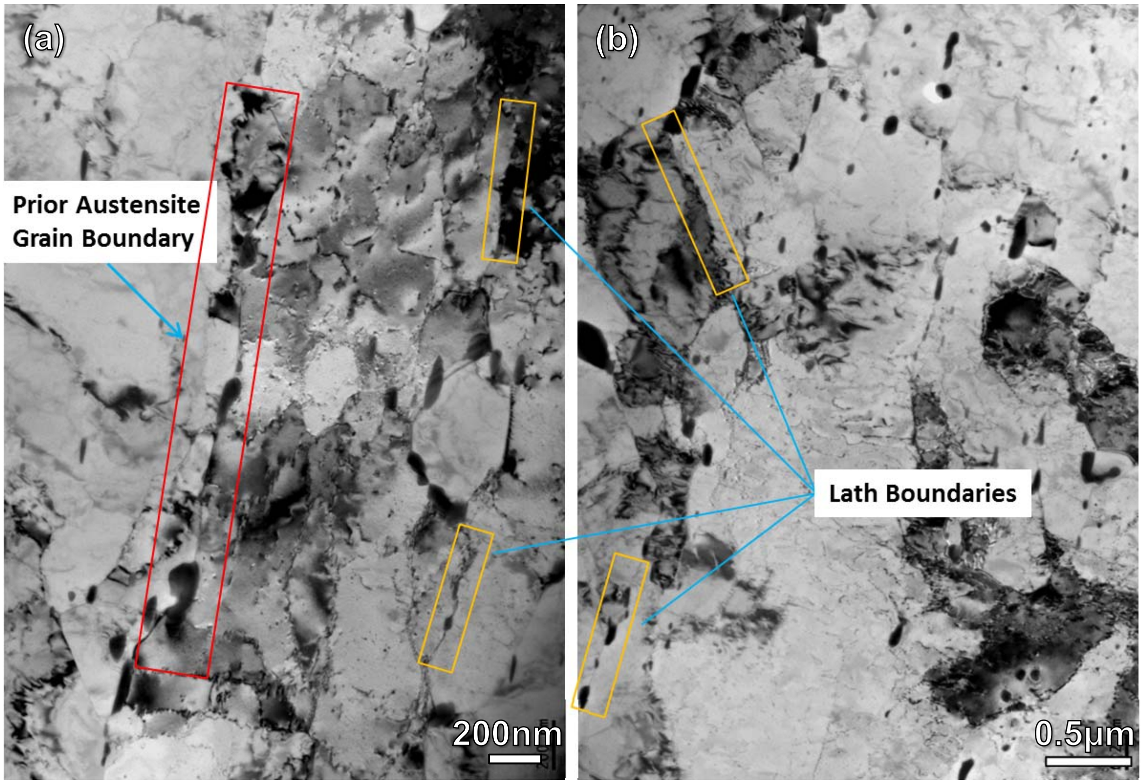

Fig.3.19: Martensitic microstructures of F82H irradiated to 12.3 dpa in low magnification.

Figure 3.20 depicts representative TEM micrographs of as-irradiated F82H specimens under different irradiation conditions. Small defect clusters and dislocation loops, appearing as black dots in BF images, produced by irradiation are shown in Figure 3.20 (a), (c), (e) and (g) for 12.3, 17.2, 17.7 and 20.4 dpa, respectively. These small defect clusters and dislocation loops, the black dots in the BF images and the white dots in the WBDF images, were observed in all four cases. It should be noted that many very small white dots in the WBDF images, which are not seen in the BF images, are small helium bubbles. In the specimen irradiated to 12.3 dpa, small defect clusters (the black dots in Fig. 3.20 (a) and white dots in Fig. 3.20 (b)) were observed, but large defect clusters with loop-shape were very few. In the specimens irradiated to higher doses of 17.2 dpa (Fig 3.20 (c)-(d)), 17.7 dpa (Fig 3.20 (e)-(f)) and 20.4 dpa (Fig 3.20 (g)-(h)), a large number of loops were visible.

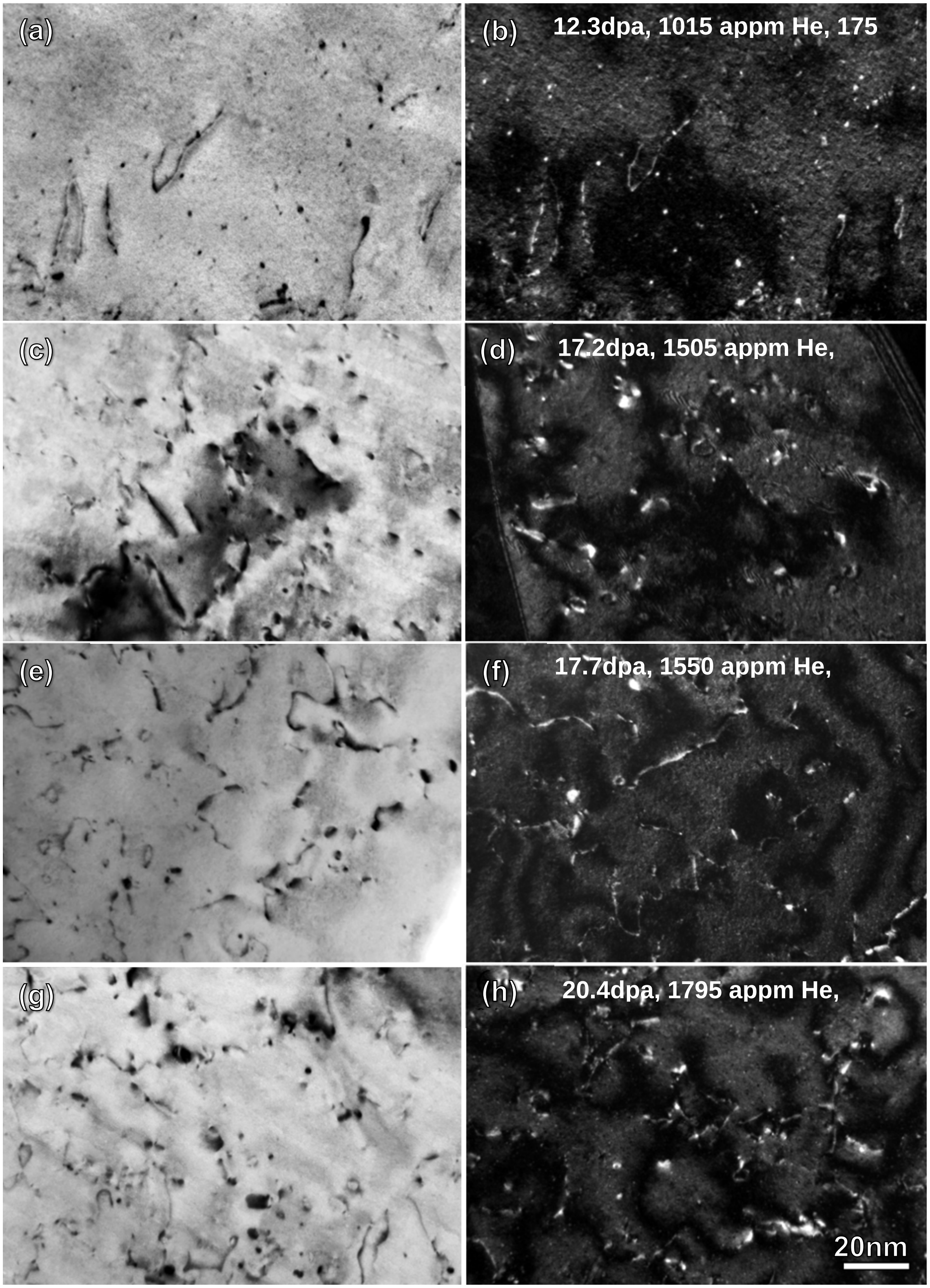
(a)
(b)
12.3dpa, 1015 appm He, 175
(c)
(d)
17.2dpa, 1505 appm He,
(e)
(f)
17.7dpa, 1550 appm He,
(g)
(h)
20.4dpa, 1795 appm He,
20nm

Fig 3.20: BF and WBDF (g, 5g), g=[110], z=[$\bar{1}$11], TEM images of defect clusters of F82H irradiated to 12.3 dpa (a)-(b), 17.2 dpa (c)-(d), 17.7 dpa (e)-(f) and 20.4 dpa (g)-(h).

Helium bubble structure of these specimens is presented in Fig. 3.21. High density of very tiny helium bubbles of ~1 nm were observed in the specimen irradiated to 12.3 dpa. Slightly larger bubbles with sizes of 1-2 nm were observed in specimens irradiated to 17.2 and 17.7 dpa as shown in Fig. 3.21 (b) and (c). With increasing of irradiation dose to 20.4 dpa, larger helium bubbles up to 3 nm were observed as well as shown in Fig 3.21 (d).

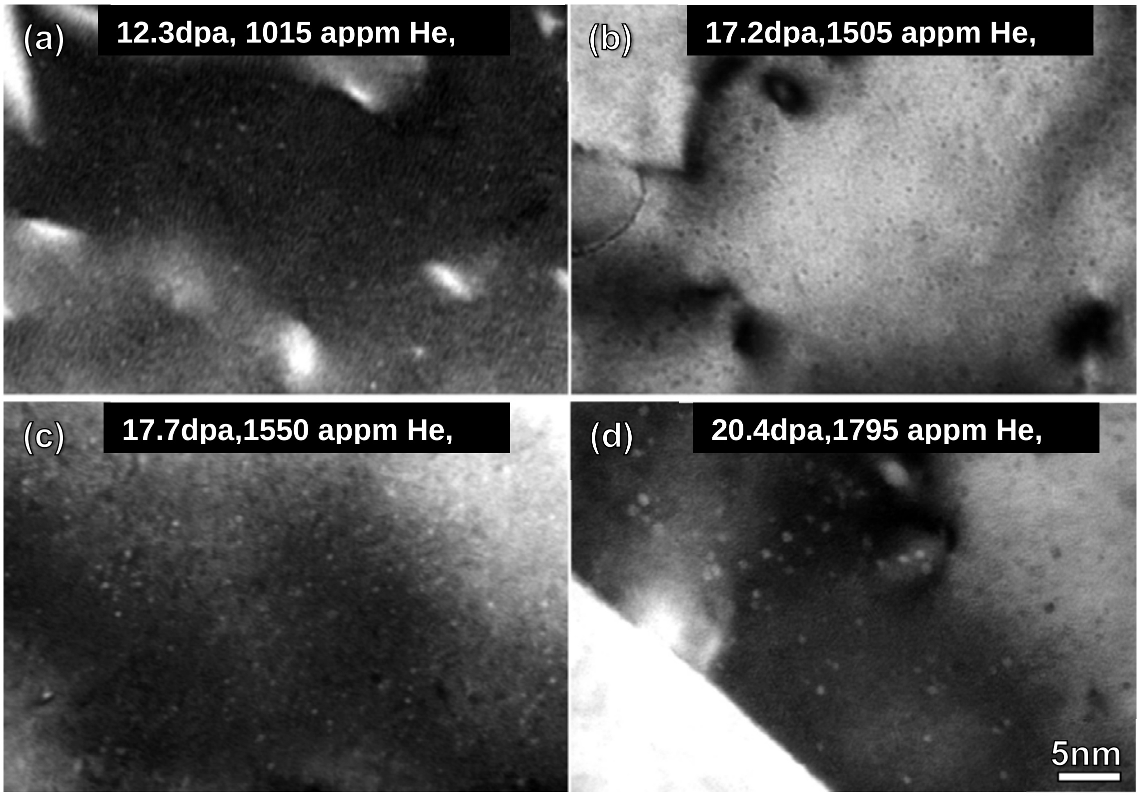

Fig 3.21: BF images of Helium bubbles of F82H irradiated to 12.3 dpa (a), 17.2 dpa (b), 17.7 dpa (c) and 20.4 dpa (d). (a), (c) and (d) are in under-focus condition, (b) is in over-focus condition.

The quantitative evaluation of number density and size of defect clusters and helium bubbles in a specimen was performed by counting them on several pictures taken from different regions. The counting of defect clusters and dislocation loops was realized in the images taken at a magnification of 240000 times. The counting of helium bubbles was done in the images taken at a magnification of 500000 times. The average size and number density of defect clusters were determined by counting approximate 300 defects in different micrographs under the same image condition ((g, 5g), g=[110], z=[$\bar{1}$11],) for each irradiation condition. The average size and number density of helium bubbles was determined by counting approximate 200 bubbles in different micrographs under the same dual beam image condition for each irradiation condition. The thickness of images selected for defects counting is in a range of 30-50 nm, while the thickness of images selected for helium bubble counting is in a range of 15-30 nm. The average size and density of defect clusters and helium bubbles are given in Table 3.2. The distribution of defect clusters in the investigated 12.3, 17.2, 17.7 and 20.4 dpa specimens is presented in Fig.3.22 (a)-(d) with average sizes of 4.24, 9.56, 10.15 and 11.87 nm respectively. The corresponding number densities of defect clusters are 2.11×10^{22}, 2.22×10^{22}, 1.48×10^{22} and 1.85×10^{22} m^{-3} respectively. The distribution of helium bubbles is presented in Fig.3.22 (e)-(h) with average sizes of 1.03, 1.15, 1.35 and 1.93 nm respectively. The number densities of helium bubbles are 0.35×10^{24}, 0.62×10^{24}, 1.25×10^{24} and 1.07×10^{24} m^{-3} respectively. A general trend is that the sizes of defect clusters and helium bubbles increase with increasing irradiation dose, while the density varies depending on irradiation dose and temperature.

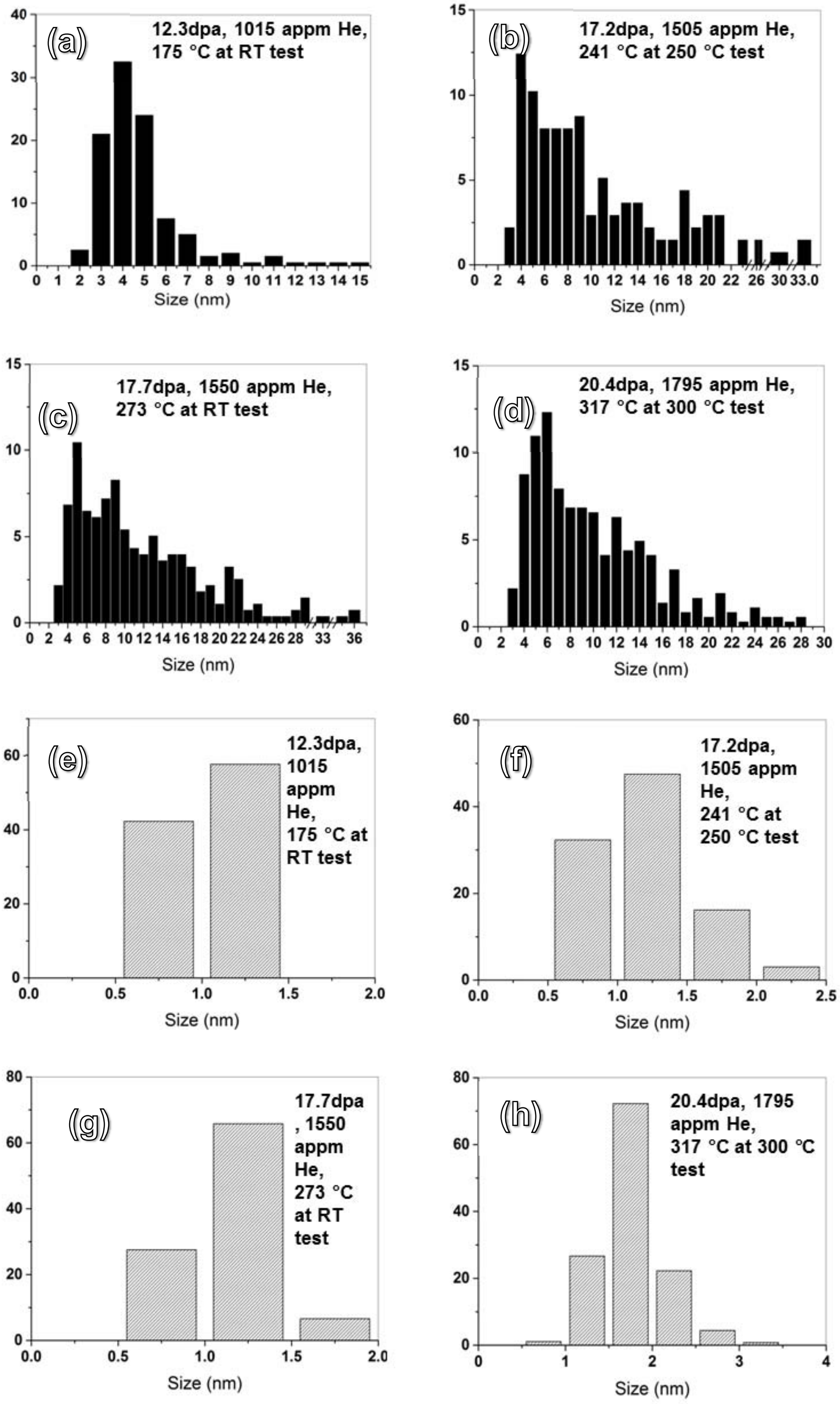

Fig 3.22: Size distributions of defect clusters (a)-(d) and helium bubbles (e)-(h) in different irradiation conditions as indicated.

Table 3.2: Average size and number density of defect clusters, helium bubbles of the F82H specimens irradiated in STIP II.

Sample	Defect cluster		Helium bubble	
	Size (nm)	Density E+22 (m^{-3})	Size (nm)	Density E+24 (m^{-3})
K18 (12.3 dpa)	4.24	2.11	1.03	0.35
K19 (17.2 dpa)	9.56	2.22	1.15	0.62
K22 (17.7 dpa)	10.15	1.48	1.35	1.25
K20 (20.4 dpa)	11.87	1.85	1.93	1.07

__Eurofer97__

Figure 3.23 depicts representative TEM micrographs of Eurofer 97 specimen irradiated to 20.4 dpa/1795 appm He at 309 °C under different image conditions. Small defect clusters and dislocation loops are shown in Figure 3.23 (a). Helium bubble microstructure of the specimen is presented in Fig. 3.23 (b), in which high-density of very tiny helium bubbles of ~1-2 nm as black dots were observed under the over-focus condition.

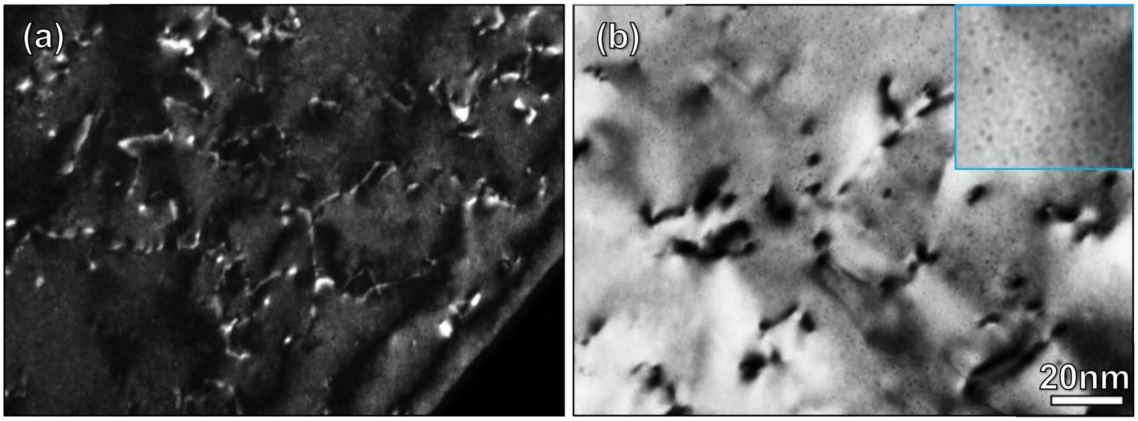

Fig 3.23: WBDF TEM images of Defect clusters (a) and BF TEM images of Helium bubbles (b) of Eurofer97 irradiated to 20.4 dpa, 1795 appm Helium at 309 °C. The inset is the helium bubbles image in high magnification.

__MANET II__

Similar to that of the Eurofer97 specimen, Figure 3.24 presents representative TEM micrographs of a MANET II specimen irradiated to 20.4dpa/1795 appm He at 309 °C. Small defect clusters and dislocation loops are shown in Figure 3.24 (a) Helium bubble microstructure of this specimen is shown in Fig. 3.24 (b). High-density of helium bubbles of ~2 nm were observed in the under-focus condition. The dynamical dual-beam TEM image condition was used for observation in this image.

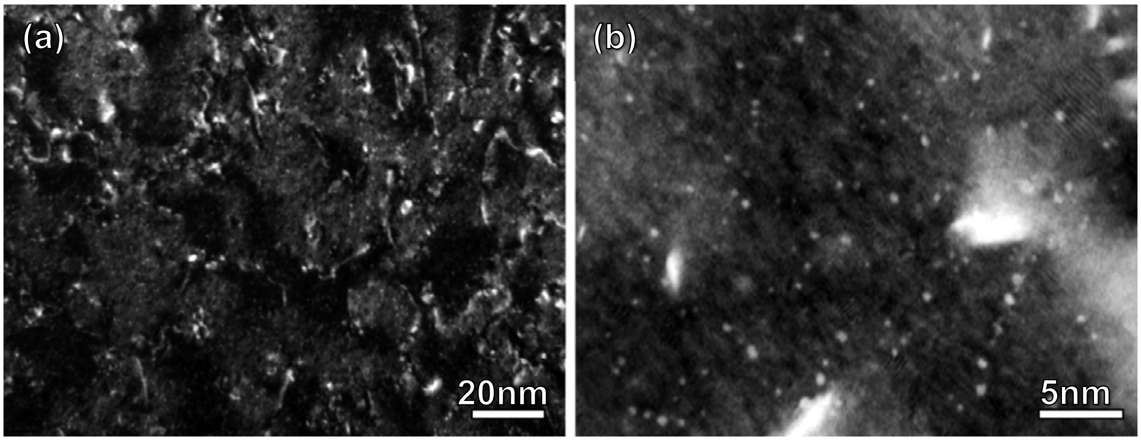

Fig 3.24: WBDF TEM images of Defect clusters (a) and BF TEM images of Helium bubbles (b) of MANET-II irradiated to 20.4 dpa, 1795 appm Helium at 309 °C.

3.3.2 Deformed microstructures of as-irradiated F82H and MANET-II

In this section, the results of the investigation of the microstructures of irradiated specimens after tensile testing at different temperatures are presented. Microstructures in either deformed area of specimens after fracture or in the deformation region just after yielding were observed.

For the fractured F82H specimen of 15.2 dpa tested at 250 °C, TEM lamellas were extracted by FIB from the slightly deformed area very close to the grip section as shown in Fig 3.25 (a). Fig 3.25 (b) is a micrograph of the lamella extracted from the position as indicated in Fig. 3.25 (a). Defect-free channels were observed in this sample as shown in Fig. 3.25 (c)-(h). Point defects are absent in the channels, whereas numerous defects are still visible in the other parts. This implies that plastic deformation is not homogenous in the specimen but localized within these bands. Some dislocation lines were observed along the channel boundaries, which were likely dislocation debris resulted from the deformation of channel area. The dislocation channels were generally, but not always, straight in the deformed F82H sample. These defect-free channels were blocked by lath boundaries or grain boundaries. The width of channels is about 100 nm. The slip planes of channel were identified along two $\{110\}$ at 120° as shown in Fig. 3.25 (c)-(f), which correspond to the former observation in neutron irradiated F82H by Hashimoto et al [106]. In addition, a channel with (112) slip plane was observed as shown in Fig. 3.25 (g) and (h). This channeling direction was also observed in irradiated iron by Zinkle et al [46]. Besides the channeling deformation mode, tangled dislocations were also observed. But the dislocation network here cannot be distinguished between the pre-existing dislocations in martensite structure and the deformation dislocations. Defect-free channel induced plastic flow localization is suspected to result in loss of ductility and premature failure.

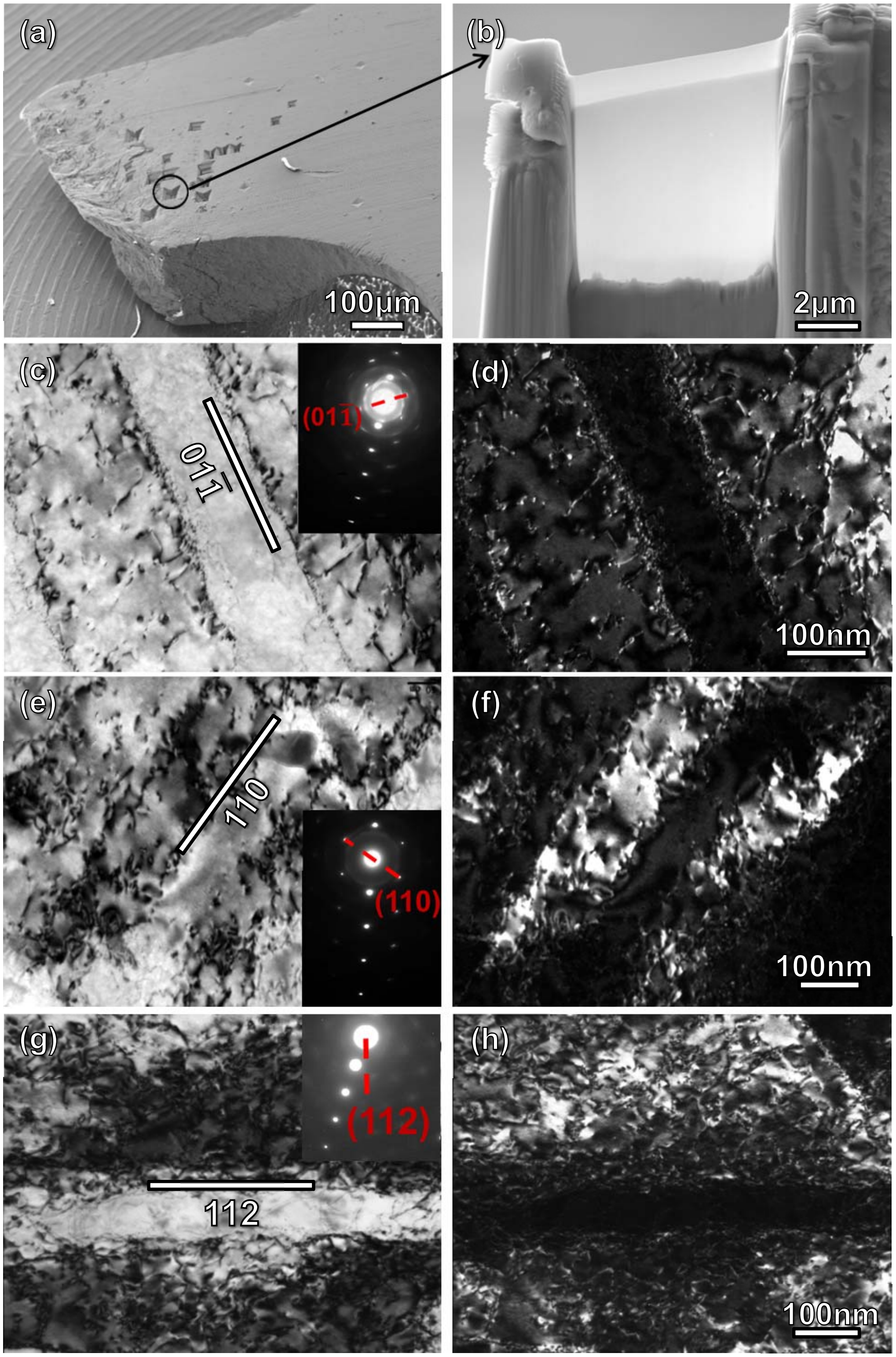
(a)
(b)
100μm
2μm
(c)
(01$\bar{1}$)
01$\bar{1}$
(d)
100nm
(e)
110
(110)
(f)
100nm
(g)
(112)
112
(h)
100nm

Fig 3.25: (a) a picture showing a part of of F82H irradiated to 15.2 dpa at 236 °C and tensile tested at 250 °C after extracting many TEM lamellas with FIB; (b) a SEM micrograph showing a TEM lamella extracted from the position indicated in (a); (c) and (d), (e) and (f), (g) and (h) showing BF and WBDF images of three different dislocation channels observed in the TEM lamella. The slip planes of the corresponding channels are indicated in the figure. The channels presented in (c)-(f) were observed in the same TEM-lamella sample, while the channel presented in (g)-(h) was observed in another TEM-lamella sample.

In addition to the deformed F82H specimen, defect-free channeling was also observed in the deformed MANET-II specimen. Unlike the investigation in F82H, TEM-lamella sample was extracted directly from the slip bands area shown in Fig. 3.26 (a), on the surface of specimen at a strain of 0.5% (see Fig. 3.16). Fig 3.26 (b) is a micrograph of the lamella extracted from the position as indicated in Fig. 3.26 (a).

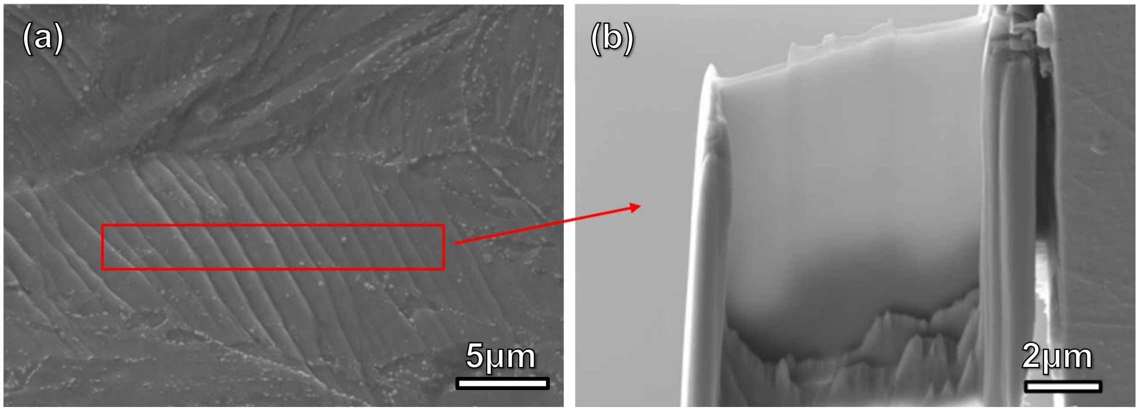

Fig 3.26: TEM lamella specimen of slip bands area fabricated by FIB.

Defect-free channels were observed in this sample as shown in Fig. 3.27 (a)-(d). In defect-free channels, most of the crystal volume is very “clean”, whereas numerous defects and tangled dislocations are visible in the other parts. Particularly, the tangled dislocations that are considered as dislocation debris resulted from the deformation of channel area are found to be located in the channel boundary area. Another interesting characteristic of defect-free channels in MANET-II is that the channels are observed to be located close to the lath boundaries or GBs, decorated with large carbides or precipitates, which act as mobile dislocation sources. The width of channels is also approximate 100 nm. The slip planes of channel were identified along $\{110\}$.

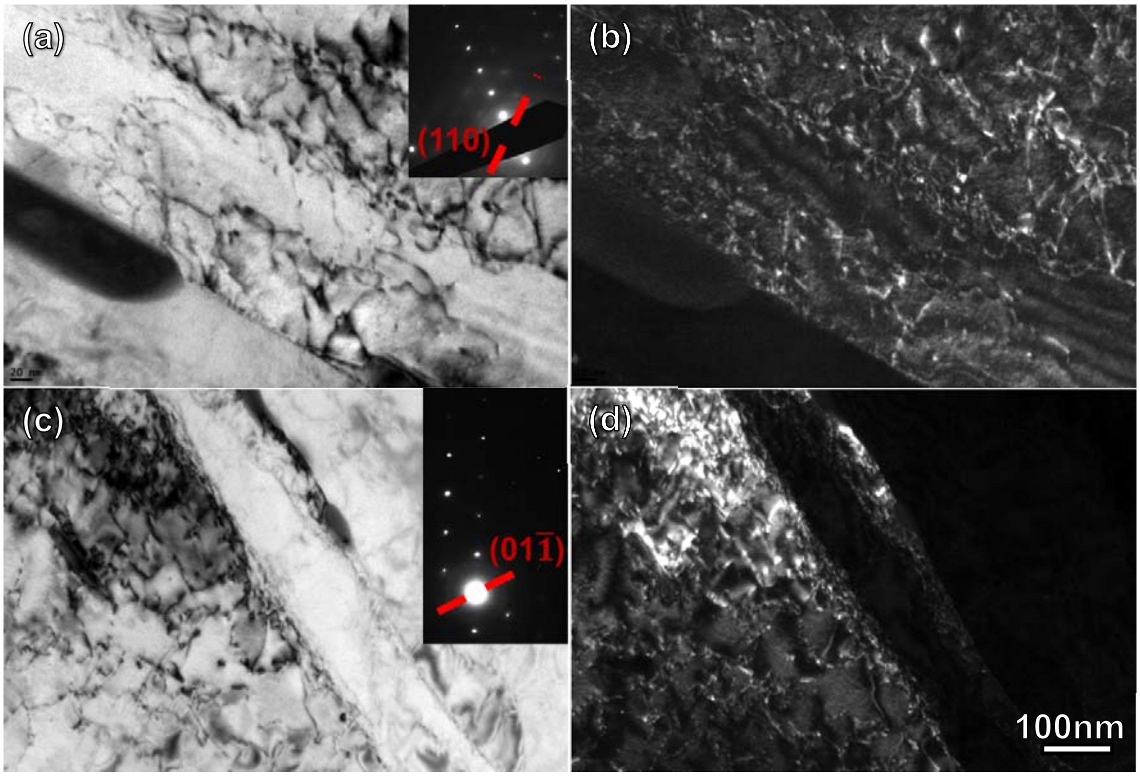

Fig 3.27: Microstructures with defect-free channels in MANET-II irradiated to 11.1 dpa and tested at RT.

3.3.3 Microstructures underneath fracture surfaces of F82H and Eurofer97

As mentioned above, the goal of this work is to study the deformation mechanisms of martensitic steels irradiated in spallation neutron sources. Based on previous tensile test results of martensitic steels irradiated in STIP, all the specimens exhibit significant hardening and loss of ductility as compared with the unirradiated specimens. However, they manifest different fracture behaviors under different irradiation and test conditions. For instance, F82H specimen at irradiation dose of 15.2 dpa shows a small amount of ductility at 250 °C and MANET-II specimen at irradiation dose of 11.1 dpa shows pretty large total elongation at RT. However, F82H specimen at irradiation dose of 15.8 dpa and tested at RT failed in elastic regime without any plastic deformation, which implies very brittle fracture. In this section, the results of the investigations on the fracture surface microstructure of completely brittle fracture specimens are presented. The main investigations regions include the microstructures either underneath intergranular fracture surface or underneath cleavage surface. TEM lamella samples were cut directly from these regions.

3.3.3.1 Brittle fracture of Irradiated F82H and Eurofer 97

Strikingly, deformation twinning as the main feature was observed underneath the fracture surface of three irradiated specimens: F82H at 15.8 dpa/1370 appm Helium at 247 °C and tested at RT; F82H at 19.6 dpa/1740 appm Helium at 304 °C and tested at 300 °C; Eurofer 97 at 19.8 dpa/1750 appm He at 300 °C and tested at RT, respectively.

For the specimens broken in a brittle manner as shown in Fig. 3.2 (c), TEM observations were performed to investigate the microstructure directly underneath the fracture surfaces by employing lamellas extracted from the fracture surfaces. Fig. 3.28 (a) shows the representative region where TEM lamellas of the observations were cut from the F82H specimen irradiated to 15.8 dpa and tested at RT. Interestingly, the deformation twinning rather than dislocation channeling was unexpectedly observed. If being viewed edge-on in TEM, the twinning bands appear as straight bands with sharp boundaries, as seen in Fig. 3.28 (b). The twinning bands can be seen as white or black strips (Figs. 3.28 (c) and (d)) depending on the imaging conditions. In WBDF images as shown in Fig. 3.28 (d), small defect-clusters and dislocation loops can still be seen inside of the twinning band. This implies that the twins were not formed by dislocation motion. In the same PAG it seems only one twinning system was activated because the twins were parallel to each other. The twinning plane was identified as (112) by diffraction pattern together with electron microscopic imaging as shown in Fig. 3.28 (c), which is the typical twinning plane in BCC metals [118, 128].

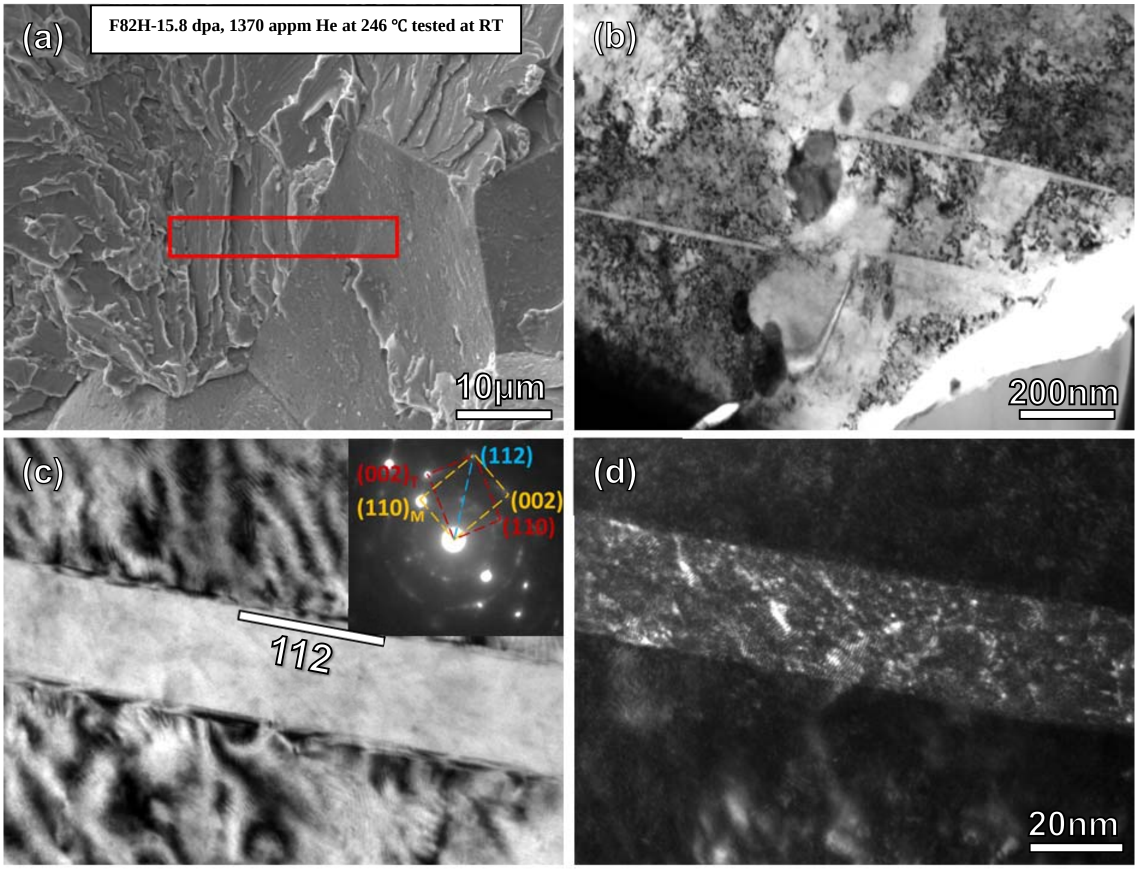

Fig 3.28: (a) Illustration of the area on fracture surface of the F82H specimen of 15.8 dpa and tested at RT where a TEM lamella extracted; (b) an edge-on view of deformation twins in the lamella; (c) and (d) a closed view of a twin in BF and DF imaging conditions.

Since it is the first time that deformation twinning is observed in bcc FM steels, some typical features of deformation twinning are also reported in Fig. 3.29. These TEM observations were done with lamella extracted from a different region from that indicated in Fig. 3.28 (a). The twinning bands can penetrate through martensitic lath boundaries (Fig. 3.29 (a) and (b)), which can be clearly seen under WBDF condition. Small mis-orientation lath boundaries as dislocation walls normally serve as barrier for the dislocation motion, which is a completely different characteristic from our recent observation of interaction between deformation twinning and lath boundaries. However, twinning bands were arrested in the vicinities of grain boundaries in Fig.3.29 (c) and (d) and large precipitates, carbides Fig.3.29 (e) and (f), where it could not propagate to the adjacent grain. Micro-crack formation was also observed in the matrix, few microns below the fracture surface, as shown in Fig. 3.30 (a) and (b), initiated in the intersection position between twins and precipitates along lath boundaries. From Fig. 3.30 (b), a large carbide/precipitate located between two deformation twins can be seen. Furthermore, there is a large cracking gap between this carbide/precipitate and the thick deformation twinning in the right side, while there is a minor cracking gap between this carbide/precipitate and the thin deformation twinning in the left side.

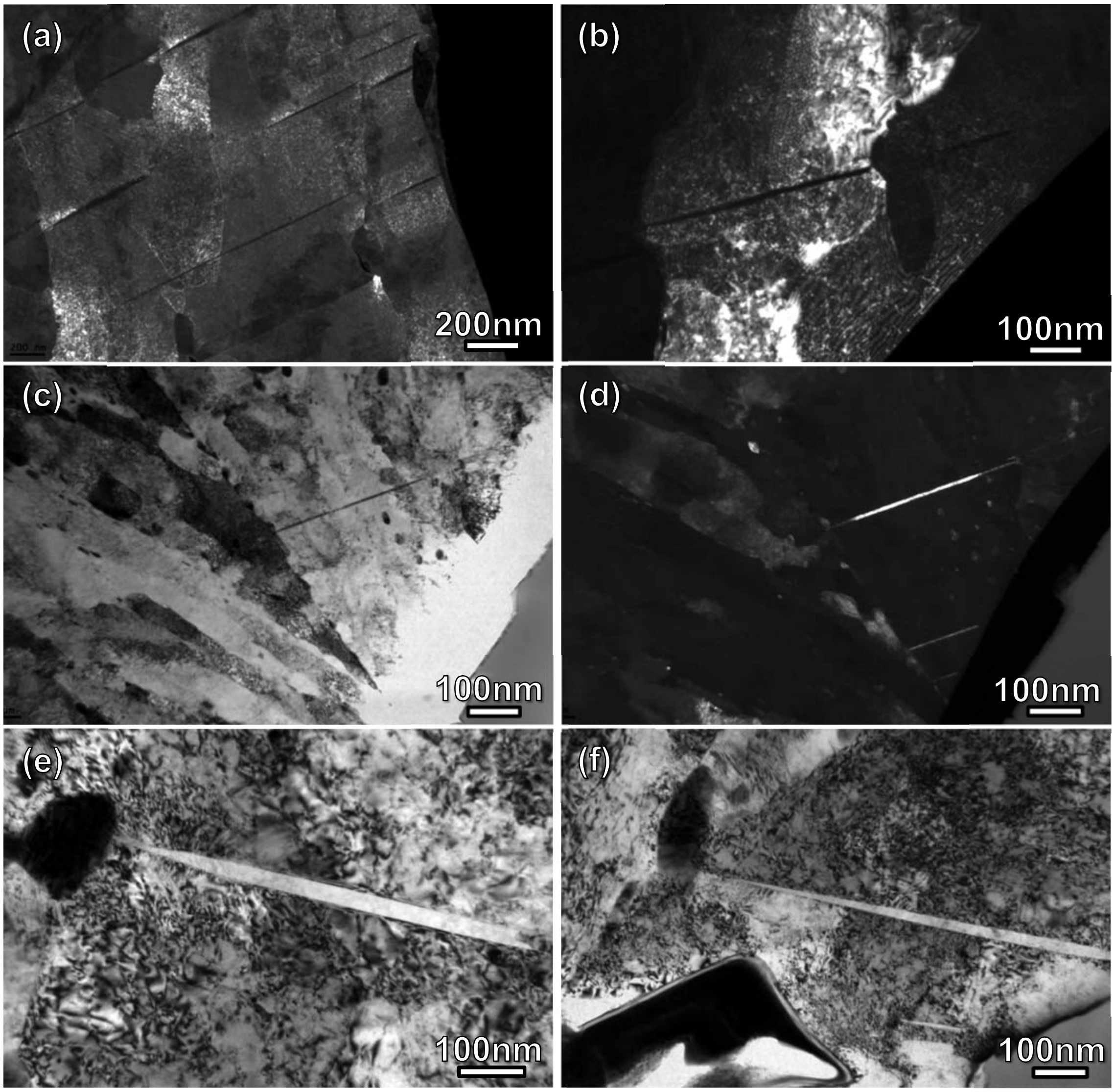

Fig 3.29: Typical features of deformation twinning in brittle fracture F82H irradiated to 15.8 dpa and tested at RT.

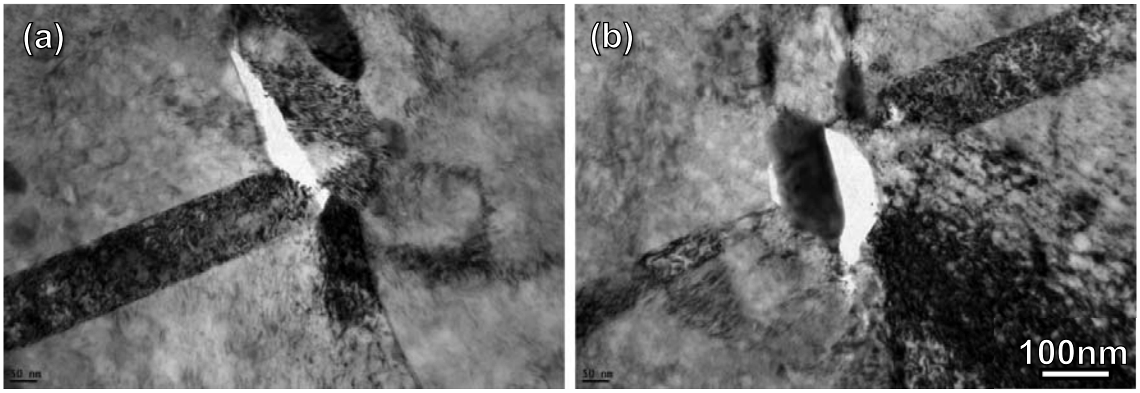

Fig 3.30: Micro-crack induced by deformation twinning in F82H irradiated to 15.8 dpa and tested at RT.

The thickness of deformation twinning was analyzed by statistical counting. The thickness distribution of deformation twinning in F82H irradiated to 15.8 dpa and tested at RT is illustrated in Fig. 3.31, and the average thickness is 34 nm.

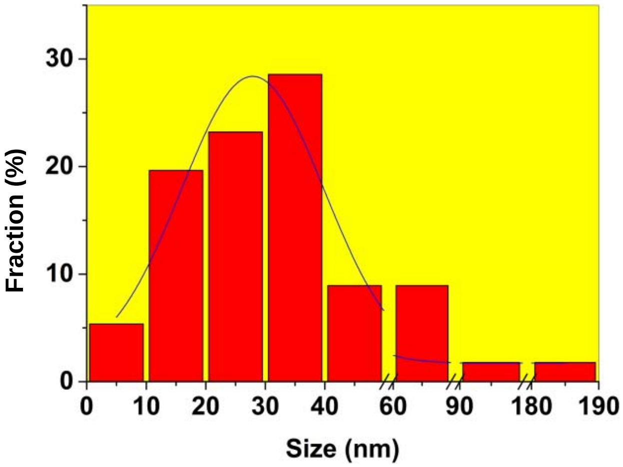

Fig 3.31: Thickness distribution of deformation twinning in F82H irradiated to 15.8 dpa and tested at RT.

As shown in Fig. 3.28 (a), the TEM lamella sample seen in Fig. 3.28 (b) was cut from the typical intergranular and transgranular-cleavage fracture surface. From Fig. 3.28 (a), we can see that one grain fractured in transgranular-cleavage mode and another grain fractured in intergranular mode. As a matter of fact, the deformation twinning was observed in the region underneath transgranular-cleavage fracture surface. However, in the region underneath intergranular fracture surface, no deformation twinning was observed in TEM image as presented in Fig. 3.32. A high density of dislocation lines can be seen underneath intergranular fracture surface in Fig. 3.32 (b), but the dislocation lines induced by deformation cannot be distinguished from pre-existing dislocation lines of martensitic structure in FM steels. Hence, it is hard firmly conclude that there is dislocation-slip deformation underneath such intergranular fracture surface during tensile testing.

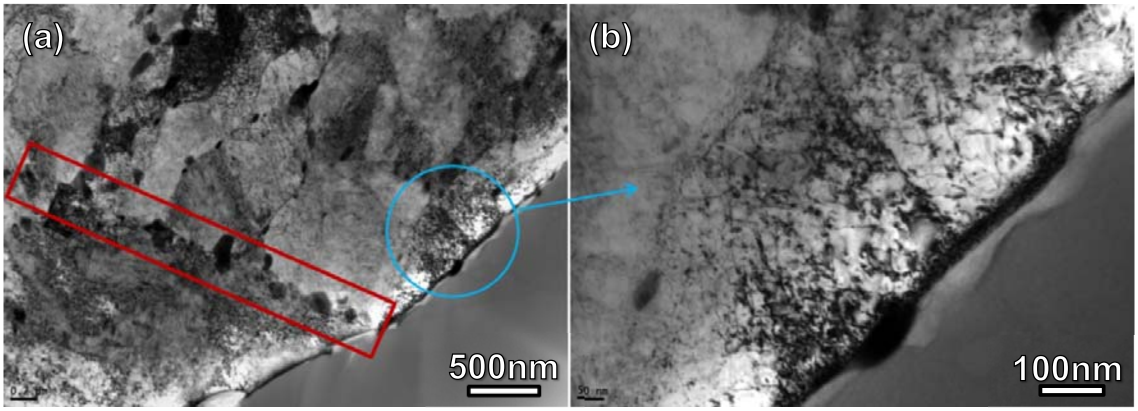

Fig 3.32: TEM microstructure underneath intergranular fracture surface in TEM lamella (Fig. 3.28 (a)) of F82H irradiated to 15.8 dpa and tested at RT.

From SEM image in Fig. 3.28 (a), we can see that there are obvious steps on the transgranular-cleavage fracture surface. The microstructure underneath these steps was carefully examined. Fig. 3.33 (a) presents an image of the microstructure in low magnification. The deformation twinning was observed either close to the steps on the transgranular-cleavage fracture surface or a couple of micrometers away from the fracture surface. Fig. 3.33 (b) shows the microstructure nearby a typical large surface step, one typical deformation twinning with about 40 nm thickness and one quite thin deformation twinning with about 10 nm thickness were observed close to this surface step. If being viewed in larger magnification in Fig. 3.33 (c), this typical deformation twinning was not indeed originated from the fracture surface but still with several tens nanometers away from it. The surface step region was also inspected as shown in Fig. 3.33 (d), besides the typical deformation twinning with straight boundaries, some broad bands with similar direction as typical deformation twinning were also observed. From the selected area (SA) diffraction pattern, no other phase could be identified. In order to gain more precise results, the nano-diffraction pattern combined with atomic resolution image should be investigated.

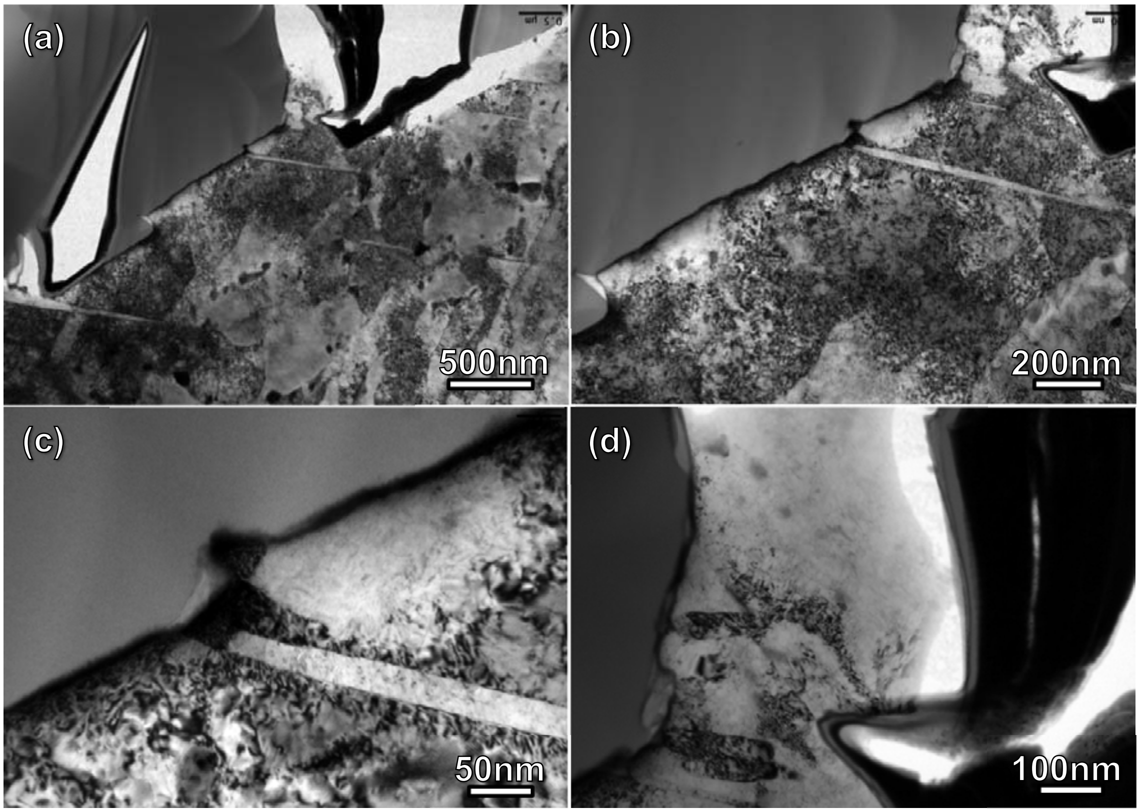

Fig 3.33: Deformation microstructures underneath cleavage fracture surface in F82H irradiated to 15.8 dpa and tested at RT.

On the intergranular fracture surface in the F82H specimen, parallel strips appeared as shown in Fig. 3.34 (a). The parallel strips indicated in the SEM image correspond to the surface steps in TEM image Fig. 3.34 (b), which is the characteristic of deformation twinning underneath the intergranular fracture surface. It can be seen from Fig. 3.34 (b), this typical deformation twinning was indeed originated from the fracture surface, and the thickness becomes narrow with distance away from the fracture surface

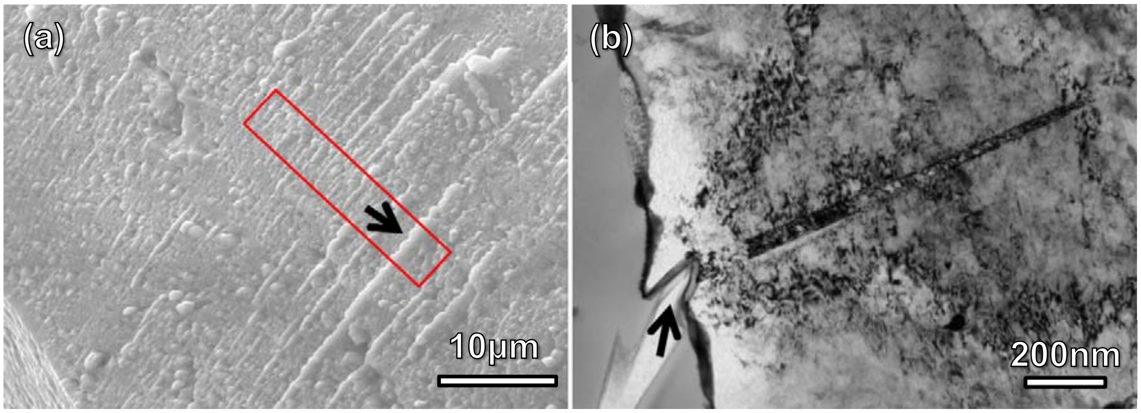

Fig 3.34: Deformation Twinning underneath Intergranular Fracture surface in F82H irradiated to 15.8 dpa and tested at RT.

In addition, another F82H specimen irradiated to 19.6 dpa, 1740 appm at 305 °C and tested at 300 °C was studied. For this specimen broken in a fully brittle manner, which is dominantly intergranular fracture mode as shown in Figs. 3.2 (g) and (h), TEM observation was performed to investigate the microstructure directly underneath the intergranular fracture. Fig. 3.35 (a) shows the representative region where TEM lamellas were cut from the specimen irradiated to 19.6 dpa and tested at 300 °C. Parallel strips were also observed on the fracture surface. Once again, the deformation twinning was expectedly observed underneath these parallel strips. The parallel strips indicated in the SEM image Fig. 3.35 (a) correspond to the surface steps in TEM image Fig. 3.35 (b) In the same PAG only one twinning system was activated because the twins were parallel to each other. The twinning plane was also identified as (112) by diffraction pattern together with electron microscopic imaging as shown in Fig. 3.35 (b).

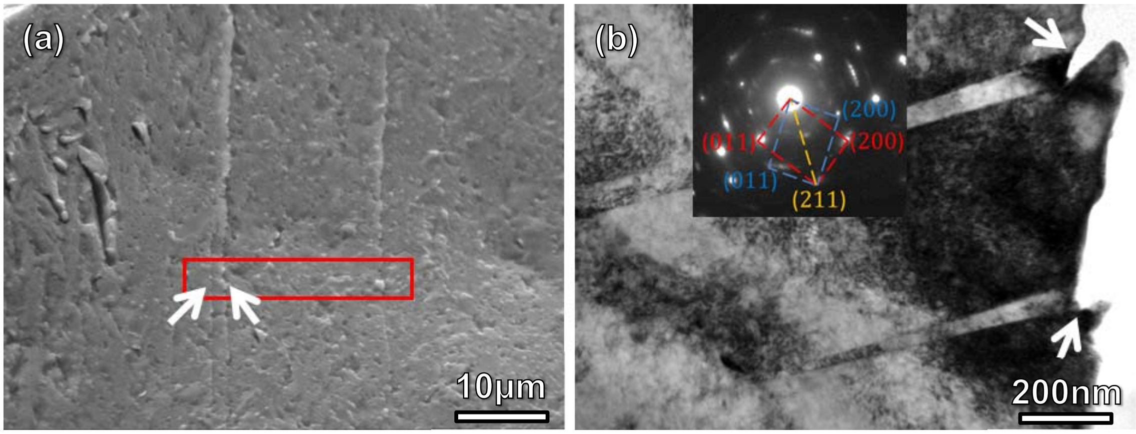

Fig 3.35: Illustration of TEM lamella region on fracture surface (a); deformation twinning in TEM image (b) underneath surface steps correlating to the parallel strips in SEM image (a); The F82H specimen was irradiated at 304 °C to 19.6 dpa and 1740 appm Helium and tested at 300 °C.

The twinning bands can be seen as white or black strips (Figs. 3.36 (a) and (b)) depending on the imaging conditions. In BF image as shown in Fig. 3.36 (a), dense small helium bubbles can still be observed inside of the twinning band in the F82H specimen irradiated to 19.6 dpa, 1740 appm at 305 °C and teste at 300 °C. The average size and number density of helium bubbles inside of the twinning band are approximately the same as those in the undeformed region according to the statistically counting. In WBDF images as shown in Fig. 3.36 (b), small defect-clusters and dislocation loops can still be seen inside of the twinning band. This implies that the twins were not formed by dislocation motion. Nevertheless, the detailed information about the average size and number density of defect clusters as well as the nature of defect clusters (eg. Burgers vector and loop type) inside of the twinning band is difficult to be evaluated due to the very small thickness of the bands. In addition, the microstructures of helium bubbles, defect clusters and dislocation loops in the F82H specimen irradiated to 15.8 dpa/1370 appm He at 247 °C and tested at RT are added for comparison as shown in Fig. 3.36 (c) and (d). Fig. 3.36 (c) and (d) indicate the microstructures of helium bubbles and defect clusters respectively. The high dense tiny helium bubbles as seen in the BF TEM image and small defect clusters and dislocation loops as seen in the WBDF TEM image still can be observed inside of the twinning band, which is alike those in the as- irradiated 19.6 dpa F82H specimen.

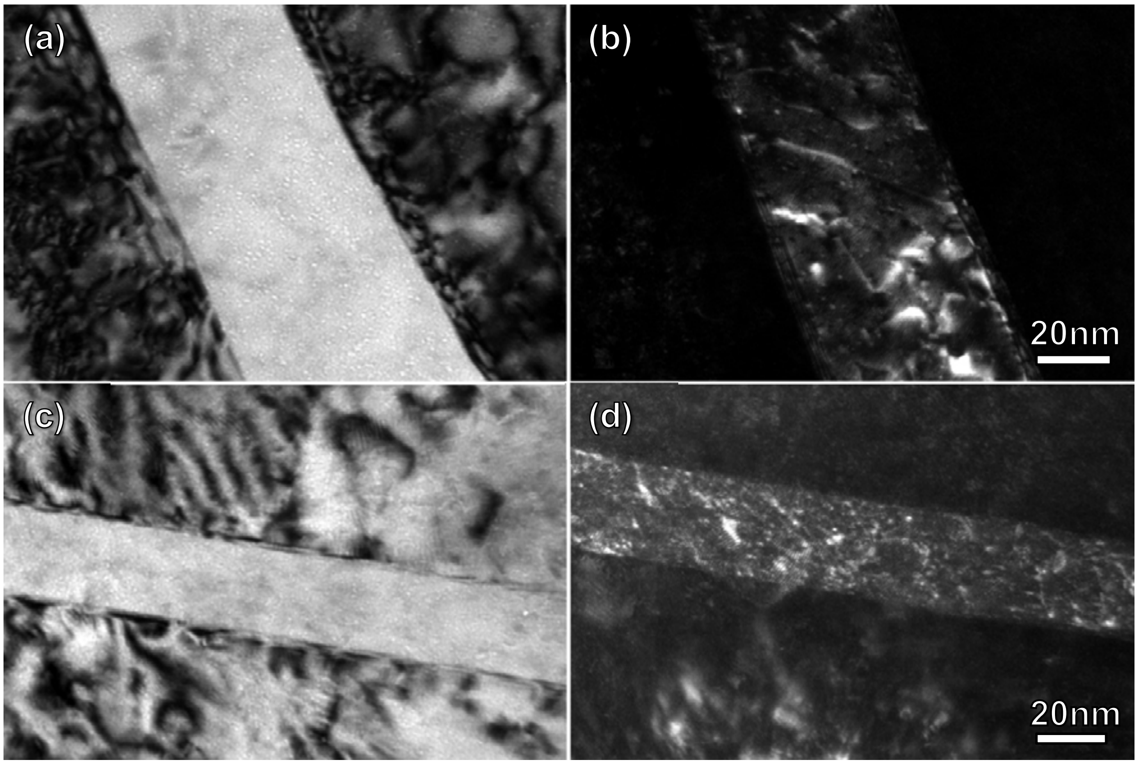

Fig 3.36: TEM images of Helium bubbles (a) and (c) and defect clusters (b) and (d) inside twinning bands. The F82H specimen was irradiated at 304 °C to 19.6 dpa and 1740 appm Helium and tested at 300 °C (a) and (b) and irradiated at 246 °C to 15.8 dpa and 1370 appm Helium and tested at RT (c) and (d) respectively.

It should be pointed out that the twinning phenomenon was also observed in another martensitic steel, Eurofer 97, which has a much smaller grain size (16 µm). A specimen of Eurofer97 was irradiated to 19.8 dpa/1750 appm He at 300 °C and tested RT. The tensile curve of this specimen and the corresponding fracture surface are shown in Fig. 3.3. From Fig. 3.3 (b), we can see that the fracture surface is dominant with intergranular and transgranular-cleavage. TEM observation was performed to investigate the microstructure directly underneath an intergranular fracture area. Fig. 3.37 (a) shows the representative region where TEM lamellas were cut. Surface strips could be seen on the fracture surface. As mentioned before, parallel strips on such an intergranular fracture surface could be related to deformation twinning bands. Although there is only one obvious strip observed on this intergranular fracture surface as shown in Fig. 3.37 (a), once again, a deformation twin was observed underneath this surface strip. The surface strip indicated in the SEM image Fig. 3.37 (a) corresponds to the surface step in TEM image Fig. 3.37 (b), which confirms the conclusion drawn from the observation of the previous F82H specimens. The surface step marked by white arrows in SEM image Fig. 3.37 (a) corresponds to that in TEM image Fig. 3.37 (b). Additionally, the thickness of twinning band becomes thinner gradually with distance away from the fracture surface and stopped in the matrix finally. The TEM image of twinning and surface step at a high magnification is presented in Fig. 3.37 (c), the white contrast part represents the twinning band, while the black contrast part represents the matrix. The twinning band is torn into two parts by the surface step. The twinning plane was also identified as (112) by diffraction pattern together with a BF image of the band as shown in Fig. 3.37 (d).

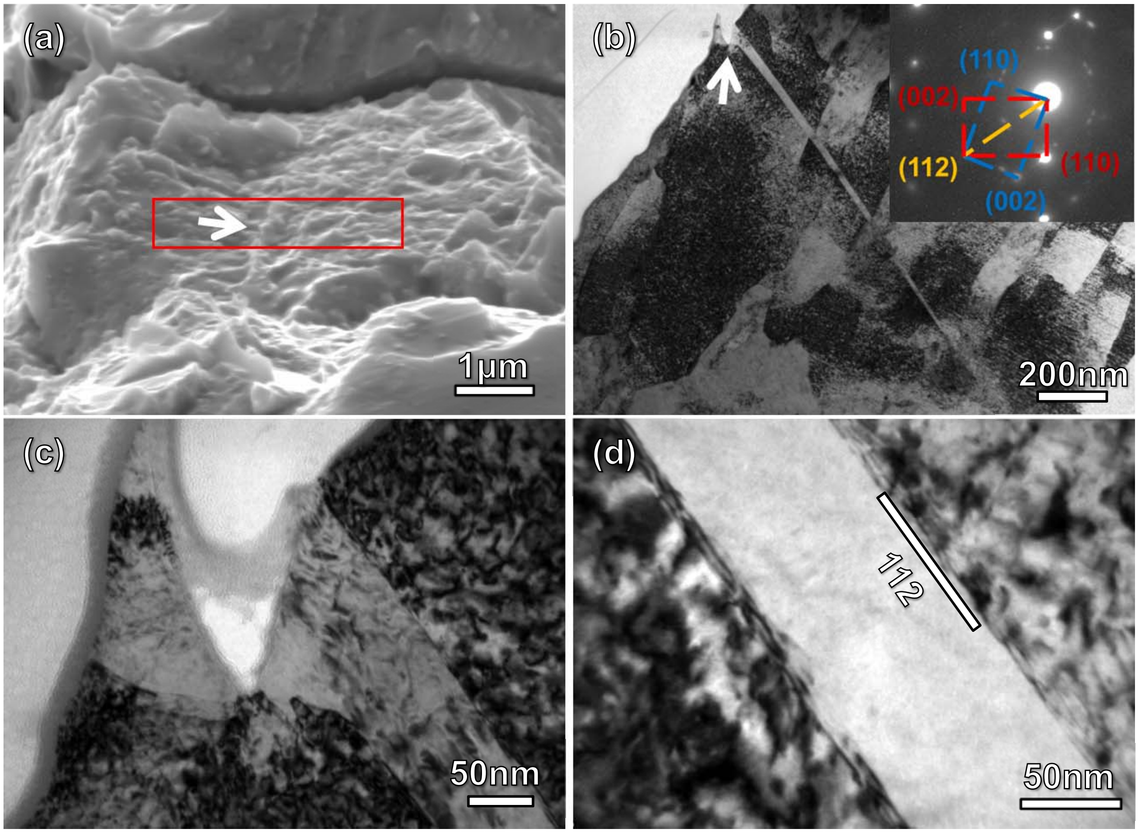

Fig 3.37: Illustration of TEM lamella region on fracture surface (a); deformation twinning in TEM image (b)-(d) underneath surface steps in SEM image (a); The Eurofer97 specimen was irradiated at 300 °C to 19.8 dpa and 1750 appm Helium and tested at RT.

3.3.3.2 Low temperature brittle fracture of unirradiated F82H, ODS-Eurofer 97 and SP T91

In order to further investigate the occurrence of deformation twinning in bcc FM steels, brittle fractured specimens of three unirradiated FM steels (ODS Eurofer97, F82H and T91) tested at liquid nitrogen (LN2) temperature were analyzed by TEM. The TEM observations were done on specimens of ODS Eurofer97 tensile tested, of F82H tensile and Charpy impact tested and of T91 small punch tested.

The ODS-Eurofer97 tensile specimen, which has a 1.5 GPa ultimate tensile stress (Fig. 3.38 (a)), broke in a brittle manner as shown in Fig. 3.38 (b) and (c). The fracture surface is dominated by typical transgranular-cleavage facets, whose dimensions correspond to the grain size [158]. Fig. 3.38 (c) shows the region where TEM lamella was cut from. Unlike in the brittle fractured specimens of irradiated FM steels, no deformation twinning was observed originated from the fracture surface. The F82H specimen tensile tested at -175 °C, which has a 1.1 GPa ultimate tensile stress, broke in a ductile manner as shown in Fig. 3.39 (b)-(e). The fracture surface is dominated by ductile dimples (Fig. 3.39 (b) and (d)) together with transgranular cleavage fracture surface (Fig. 3.39 (c) and (e)). Obviously, as seen from the fracture surface in Fig. 3.39 (a), the typical cleavage fracture surface is only observed in few grains on the right side area while the majority of fracture surface is dominant with ductile-dimples on the left side region. The cleavage facet in this specimen is relatively flat with river pattern as seen in Fig. 3.39 (e). TEM observation was performed to investigate the microstructure directly underneath the fracture surface in the region indicated in Fig. 3.39 (e). The result is alike in ODS-Eurofer 97, no deformation twinning was observed underneath the fracture surface. Another two cases of low temperature brittle fracture of unirradiated FM steels are small punch test of T91 and Charpy impact test of F82H at LN2 temperature. The fracture surfaces of these two specimens are shown in Fig. 3.40. The fracture surface is dominant with transgranular-cleavage facets with dimples rupture seen from the Figure. The cleavage facet of the specimens are relatively flat with river pattern but without surface step. 3-4 TEM lamella samples were cut directly from the cleavage fracture surface in each specimen. However, there is no deformation twinning observed either underneath fracture surface or inside of grains far away from surface.

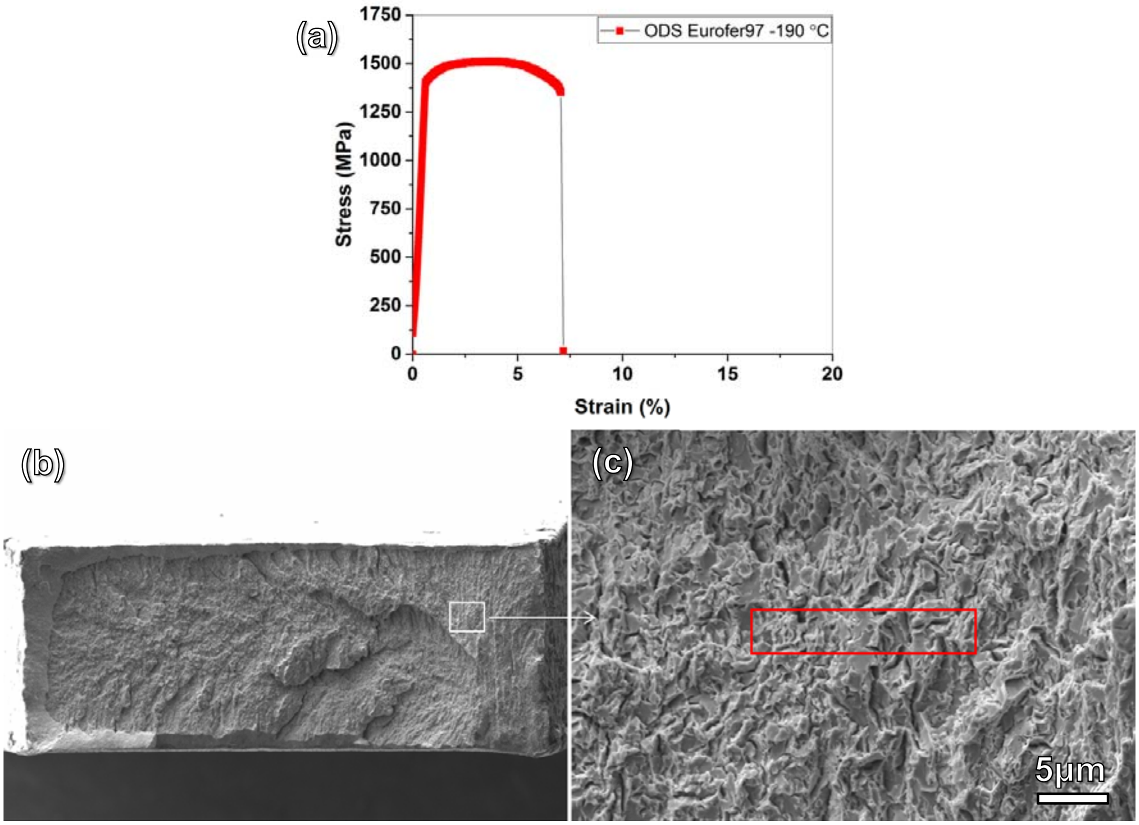

Fig 3.38: Illustration of fracture surface of ODS Eurofer97 tested at LN2 temperatureure in low magnification (a) and TEM lamella region on typical fracture surface in high magnification (b).

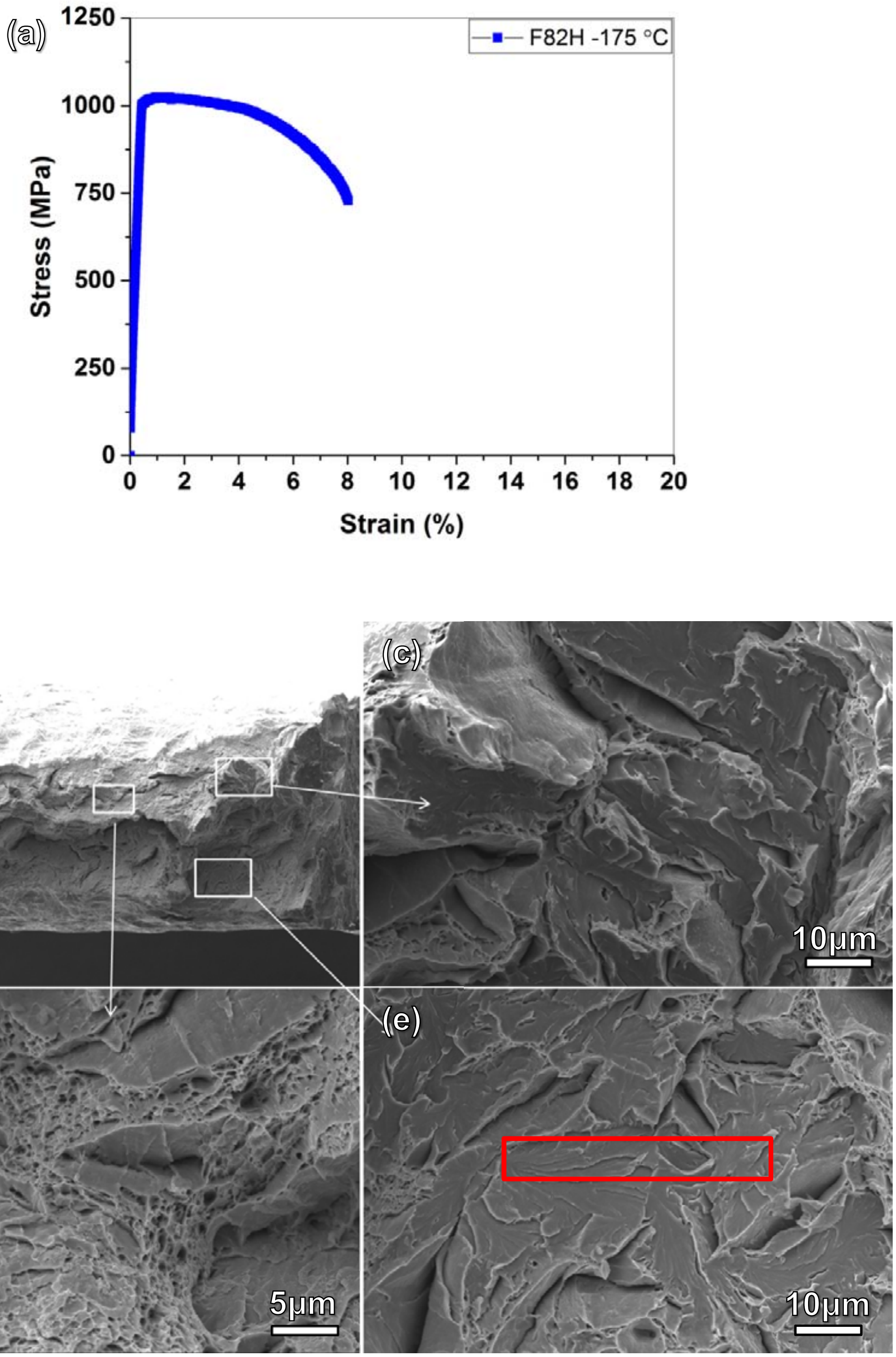

Fig 3.39: Illustration of fracture surface of F82H tested at LN2 temperature (a) in low magnification (b) and transgranular-cleavage fracture surface in high magnification (c); ductile-dimple fracture surface in high magnification (d) and TEM lamella region on typical cleavage fracture surface in high magnification (e).

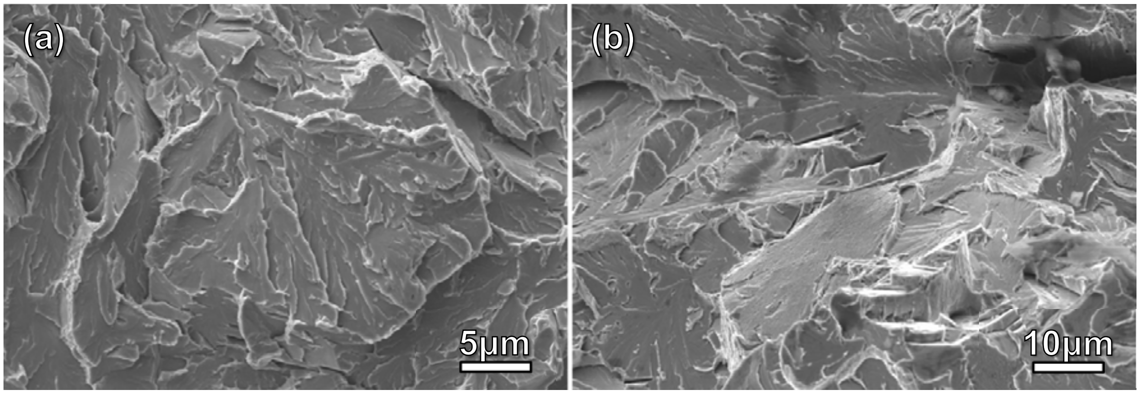

Fig 3.40: SEM image of fracture surface of T91 specimen by small punch test (a) and F82H specimen by Charpy impact test (b) at LN2 temperature.

4. Discussion

4.1 The dose dependence of defect density and size distribution

As shown in Section 3.3, the microstructure of as-irradiated F82H, Eurofer 97 and MANET-II specimens was investigated using TEM. In general the results are in agreement with the data published by Jia [8, 68, 69], Vieh [159] and Zhang et al. [156] obtained from F82H and Eurofer 97 irradiated in STIP-I and STIP-II under similar conditions.

Defect clusters and helium bubbles have been detected in the as-irradiated F82H specimens in this work. The detailed information of number density and size distribution of defect clusters and helium bubbles of irradiated F82H is presented in Table 3.2 and Fig.3.22. The dose dependence of number density and size of defect clusters is given in Fig.4.1. The average cluster size is increasing with dose as shown in Fig.4.1 (a). With increase of size, the morphology of defect clusters changes from small dots to loop shape. The number density of clusters does not change significantly as seen in Fig.4.1 (b). The error bar is the standard deviation for the defect clusters size. For the density of defect clusters, it is the standard deviation combined with accuracy deviation of thickness determination (±10%). The results are in fairly agreement with the data of F82H irradiated in STIP-I and STIP-II obtained by [8, 68, 69] using the same image conditions. For example, at about 10 dpa at irradiation temperature of about 170 °C, the average size and density of defect clusters obtained by Jia are 3.3-4.2 nm and 3-4x10^{22}/m^3, respectively. The average size is about the same as the present one. The density is slightly higher than the present data. It could be due to smaller thickness of the regions used for counting defect clusters by Jia. In his work, the thickness of regions used for counting was around 30 nm and in this work the thickness of lamella samples is about 50 nm. It is known that the measured density of small defect clusters decreases with the thickness of TEM foil because of reduced contrast and increased overlap of defect clusters [21].

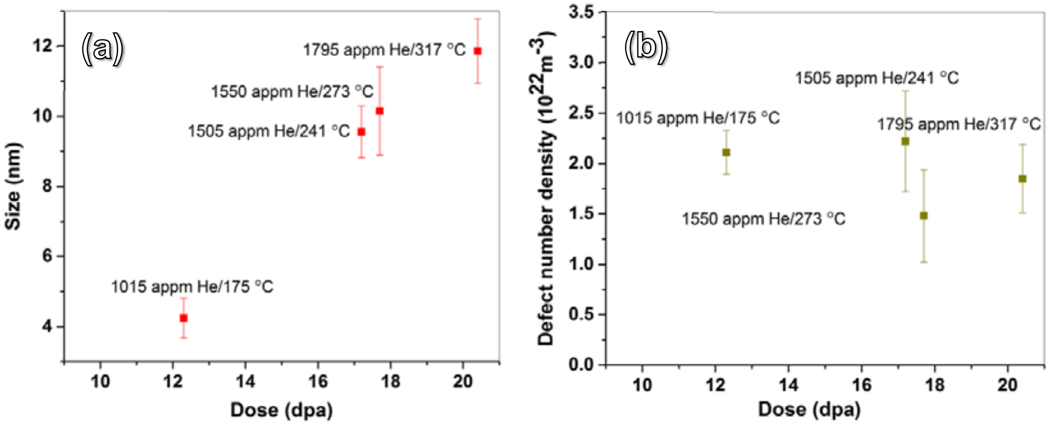

Fig 4.1: Evolution of the average size (a) and number density (b) of defect clusters with dose in irradiated F82H. The irradiation temperature of each specimen is indicated in the figure.

The change of the size and density of defect clusters depends on both irradiation dose and irradiation temperature. The defect clusters grow rather fast at above 250 °C. Meanwhile the density decreases rapidly [68]. At 15-16 dpa, Jia showed a much smaller average cluster size of 4.9 nm and higher density of 3.8×10^{22} /m^3 for F82H irradiated at 165 °C as compared with the corresponding data (≈ 10 nm and 1.8×10^{22} /m^3) of the 17.2 and 17.7 dpa specimens irradiated at around 240 °C. It is clear that the difference can be mainly attributed to the effect of irradiation temperature. Due to the great differences between spallation target and fission reactor irradiation environment, e.g. high helium and hydrogen production, unstable proton and neutron fluxes, unstable irradiation temperature, and so on, it is believed that a comparison of microstructural changes between STIP irradiated and neutron irradiated FM steels at similar dose and temperature would be rather difficult.

The helium bubble structures of the four specimens were shown in Fig. 3.21. In the specimen of 12.3 dpa/850 appm He irradiated at 165 °C, the helium bubbles are very small, around 1 nm in diameter. In this work, lamella samples of 50 nm thickness were used, which is quite thick for observing such small bubbles. In this case, bubbles of sub-nanometer (0.7-1.0 nm) sizes are hardly detected because of weak contrast. Compared to Jia's data, the present data show slightly larger average size but lower density. In Jia's observation of helium bubbles, the thickness of the foil was about 25 nm. If one uses relatively thicker samples, such small bubbles may not be visible, as it is the case in Vieh's work [159]. It is well known that the size of bubbles increases with dose or helium concentration or irradiation temperature. The density of bubbles also increases with dose or helium concentration, but decrease with irradiation temperature [8]. The dose dependence of number density and size of helium bubbles is given in Fig.4.2. No error bar is applied for bubble size due to the relatively homogenous distribution and the error bar for bubble density is the accuracy deviation of thickness determination. For the tiny bubbles with size < 1nm cannot be detected by TEM, hence, the measured number density of bubbles in 12.3 and 17.2 dpa is relatively small. With the increase of irradiation dose, helium concentration and irradiation temperature, the size of bubbles grows distinctly. However, from the trend of number density of helium bubbles given here, it is hard to give a definitive conclusion due to the resolution limit of the TEM observation and deviation from thickness measurement by EELS. Nevertheless, the trend of the size and density increasing with dose reflects a combined effect of irradiation dose, helium concentration and irradiation temperature of the present irradiation conditions.

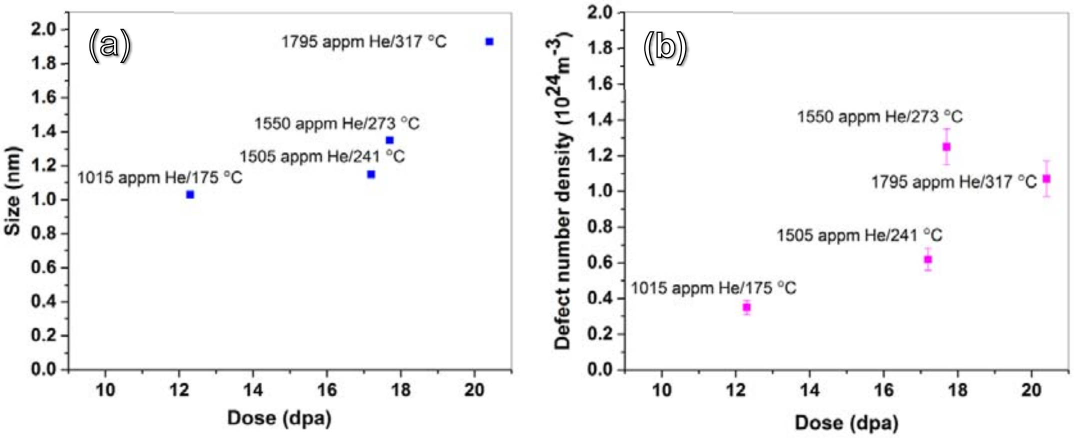

Fig.4.2 Evolution of the average size (a) and number density (b) of helium bubbles with dose in irradiated F82H.

Although the microstructures of the specimen in as-irradiated conditions were investigated in detail, it was not intended to investigate as such the dose dependence or the temperature dependence of the defect clusters or the helium bubbles. The TEM observation of as-irradiated microstructure was aimed at providing the necessary information for the understanding of the mechanical behaviors and deformation mechanisms of the specimens.

4.2 Correlation between irradiation defects and hardening (F82H)

Even if the main purpose of this work is to investigate the embrittlement effects induced by radiation damage and helium, the hardening effect induced by irradiation has a critical role on fracture toughness, as fracture and plasticity are intrinsically linked to each other. Hence, the correlation between irradiation defects and hardening is essential. Generally, this correlation is based on Seeger and Orowan model [160, 161]. The model relates the increase in yield strength to the irradiation-induced defects, described through their defect density (N_i), defect diameter (d_i) distributions as well as through their barrier strength (α) as indicated in Eq.4.1 [162].

$$\Delta\sigma = \alpha M \mu b \sqrt{N_i d_i} \tag{4.1}$$

$\Delta\sigma_y$ represents the irradiation-induced increase of the yield stress, M is the Taylor factor (3.06) that relates the shear stress on a slip plane in a single crystal to the applied uniaxial tensile stress necessary to activate slip in a polycrystal, α is the barrier strength of the type of dispersed obstacle considered (e.g. bubbles/clusters), μ is the shear modulus of the matrix (80 GPa in FM steel) that is a weak function of temperature and not strongly sensitive to irradiation, b is the amplitude of the Burgers vector of the mobile dislocations (2.49 Å for ½ <111> dislocations in bcc FM steels).

Equation (4.1) is strictly valid when only one type of defects contributes to the irradiation-hardening. When more than one type of obstacles with different strengths are present, one has to consider a superposition rule. As a matter of fact, several superposition rules have been proposed, which depend on the character of the obstacles considered. For instance, the presence of long-range (e.g. network dislocations) and short-range obstacles (e.g. bubbles) leads to linear superposition of the contribution of each type of obstacle. In the case of multi-types of short-range obstacles as such irradiation induced defect clusters, loops, bubbles or cavities, precipitates, a root-sum-square is the most appropriate rule [163]. However, in the case of obstacles with different strengths, some authors consider a linear superposition is more justified [32]. In our case, we have to take into account the contributions of the helium bubbles and of the defect clusters. As for the Si-enriched nanometer sized precipitates detected by APT (Atom Probe Tomography) analysis in high dose F82H specimens [164], it seems that they do not contribute much to the hardening effect [4]. The barrier strength value of small (1-1.5 nm) helium bubbles obtained from previous annealing experiments on the FM steels irradiated in STIP is in the order of 0.1 [159, 165], and the strength of clusters in BCC lies in the range 0.25 -0.5 [150, 159, 166-168]. Therefore, we are in the presence of weak obstacles (He bubbles) and rather strong obstacles (defect clusters) so that we consider a linear superposition and write the irradiation hardening $\Delta\sigma_y$ as:

$$\Delta\sigma_y = \Delta\sigma_B + \Delta\sigma_C \tag{4.2}$$

where

$$\Delta\sigma_C = \alpha_C M \mu b \sqrt{N_C d_C} \qquad \text{(defect cluster contribution)} \qquad (4.3)$$

$$\Delta\sigma_B = \alpha_B M \mu b \sqrt{N_B d_B} \qquad \text{(helium bubble contribution)} \qquad (4.4)$$

The values of barrier strength α of the obstacles can be deduced from the measured increase of yield strength $\Delta\sigma_y$ obtained from tensile test and of the N_C, d_C , N_B, d_B determined from TEM observation. In this work, as discussed in the previous section, the density of helium bubbles measured from specimens K18 (12.3 dpa) and K19 (17.2 dpa) is not precise due to small bubble size and thick TEM lamella. The data of these two specimens cannot be used for the hardening analysis. Therefore, the analysis is just performed by using the hardness and TEM data measured from the high-dose ends of specimens K20 (i.e. K20H, 20.4 dpa) and K22 (i.e. K22H, 17.7 dpa) as given in Table 3.1 and Table 3.2.

The increase of yield stress $\Delta\sigma_y$ on these specimens was assessed indirectly by measuring the corresponding Vickers hardness ΔH_v increase, and converting it into the yield stress. The relationship between ΔH_v and $\Delta\sigma_y$ for FM steels has been statistically fitted by Busby et al [150] and reads $\Delta\sigma_y = 3.06\ \Delta H_v$. The calculated yield stress increase, based on the hardness measurement, is presented in Table 4.1. Taking the barrier strength value of 0.1 for small helium bubbles, the contribution of helium bubbles to the hardening of the specimens ($\Delta\sigma_{yB}$) can be calculated using Equation 4.4. The results are given in Table 4.1. Using Equation 4.2 the contribution of defect clusters to hardening can be easily deduced. To calculate the barrier strength of the defect clusters, the density values in Table 3.2 measured under a single WBDF image condition has to be corrected. As mentioned before, the actual density of defect clusters and loops was evaluated only from micrographs with single imaging condition z= [111] and g= (110), in which only up to 40% of the defect clusters and loops could be detected [169]. Hence, a multiplication factor of 2.5 was used to correct the number density of the clusters. Finally the barrier strength of defect clusters obtained for the two specimens K22H and K20H is 0.23 and 0.22, as shown in Table 4.1.

Table 4.1 Calculated $\Delta\sigma_y$ from ΔH_v as: $\Delta\sigma_y = 3.06\ \Delta H_v$

Sample	dpa/He appm	$\Delta Hv_{0.5}$	$\Delta\sigma_y$	$\Delta\sigma_{yB}$	$\Delta\sigma_{yC}$	α_C
K22H	17.7/1550	171	523	250	273	0.23
K20H	20.4/1795	193	591	277	314	0.22

The barrier strength values of 0.22-0.23 for the defect cluster and loops in FM steels seem a little too small, particularly considering the possible contribution of the Si-enriched precipitates was not taken into account. Performing the same exercise by using the root-sum-square superposition (i.e. $(\Delta\sigma_y)^2 = (\Delta\sigma_B)^2 + (\Delta\sigma_C)^2$), we get the barrier strength of defect clusters being **0.37±0.1** for the K20 and K22 specimens. This value is in good agreement with 0.38-0.51 obtained by Liu and Biner [12] through molecular dynamics simulations on screw dislocation-interstial loops interaction in BCC iron at 300K and also the published results. For instance, Bergner et al [168] obtained the values of α_C as 0.4±0.16 based on experimental results of neutron-irradiated Fe-Cr alloys, considering two types of defects including defect clusters and alpha prime α’ precipitates. P.V. Durgaprasad et al [170] determined the barrier strength of loops ranging from 0.32 to 0.75 in irradiated ferritic/martensitic steels by using dislocation dynamic (DD) simulations.

4.3 Fracture mechanisms of FM steel in different irradiation and test conditions

The crack initiation and propagation assessment of unirradiated and irradiated FM steel specimens has been performed by interrupted SP and tensile test accompanying with SEM observation. For the unirradiated T91 under successive SP test, there were two kinds of crack initiation sites: initiation from the inclusions when testing at RT and initiation from grain boundaries (GBs) or lath boundaries (LBs) when testing at LN2 temperature. Initiation at inclusions was accompanied with plastic deformation ahead of crack tip and propagation can be easily captured, while initiation at GBs or LBs was with a small plastic deformation zone ahead of the crack tip and fast crack propagation occurred. For the irradiated F82H under successive tensile test, the intergranular crack initiates from the side surface before yielding. However, there were two kinds of propagation modes: in the specimen irradiated to 11.1 dpa the cracks were arrested by GBs, while in the specimen irradiated to 15.8 dpa fast crack propagation resulted in intergranular or transgranular fracture. For the crack arrested by GB, slip bands were activated in the grains ahead of crack tip and crack propagated along one of the slip band. For the crack with fast propagation, it was not possible to capture the propagation trace and only the final fracture surface could be obtained. With regard to the MANET II irradiated to 11.1 dpa and electro-polished under successive tensile test, the first cracks were observed at 4.6% strain level and the crack direction was parallel to one of slip planes. The crack initiation and propagation assessment will be compared with the fracture surface to further discuss the fracture behavior in different irradiation and test conditions.

Three different FM steels F82H, Eurofer97 and MANETII irradiated in different conditions and tensile tested at different temperatures showed various deformation and fracture behaviors. The four F82H specimens at different irradiation conditions tested at different temperatures exhibit different fracture modes. The low dose specimen at 10.7 dpa possesses pretty large total elongation at RT, although the uniform elongation decreased to less than 1%. However, at a little higher irradiation dose of 15.8 dpa, the specimen tested at RT failed in elastic regime without any plastic deformation, and showed a mixed mode of about 50% intergranular fracture and transgranular cleavage fracture. The two specimens demonstrate a clear irradiation dose dependence of fracture behavior of the steel. The fracture behavior of the irradiated specimens depends strongly on test temperature. The specimen of 15.2 dpa exhibited a significant amount of ductility at 250 °C compared with the 15.8 dpa specimen tested at RT. Meanwhile, its fracture surface demonstrated a mixed mode of ductile and quasi-cleavage fracture. With increasing irradiation dose and helium concentration, the brittle fracture features were greatly enhanced. At a high dose of 19.6 dpa and with 1740 appm He, F82H steel was found to be brittle even at 300 °C. The specimen failed again without any plastic deformation.

The synergistic low-temperature hardening-helium embrittlement (LTHE) was studied by Dai and Odette [171]. As schematically illustrated in Figure 4.3, LTHE may be described as follows. Cleavage fracture can be triggered when the local stress at the tip of a blunting crack, $M\sigma_y$, exceeds a critical local stress σ$_c$* of the order of 2000 MPa in FMS [172]. M is a factor of about 1.5 to 3 depending on the shape of the crack [173]. Similarly, brittle IG fracture occurs when the stress at the crack tip is greater than the critical local stress σ$_{ig}$*, and when it encompasses a sufficient volume for grain boundary decohesion. If transgranular cleavage occurs at the first place, then σ$_{ig}$* is higher than σ$_c$*. However, He accumulation at the grain boundaries results in a decrease of σ$_{ig}$* decreases. When σ$_{ig}$* is lower than σ$_c$*, GB becomes the favored crack path. σ$_{ig}$* continues to decrease with increasing He accumulation resulting in an increment of the ductile to brittle transition temperature (ΔT$_i$ in Fig.4.4) . The transition from transgranular cleavage to IG crack path can be determined with fractography observations and is related to an increase of the fraction of grain boundary facets on the fracture surface.

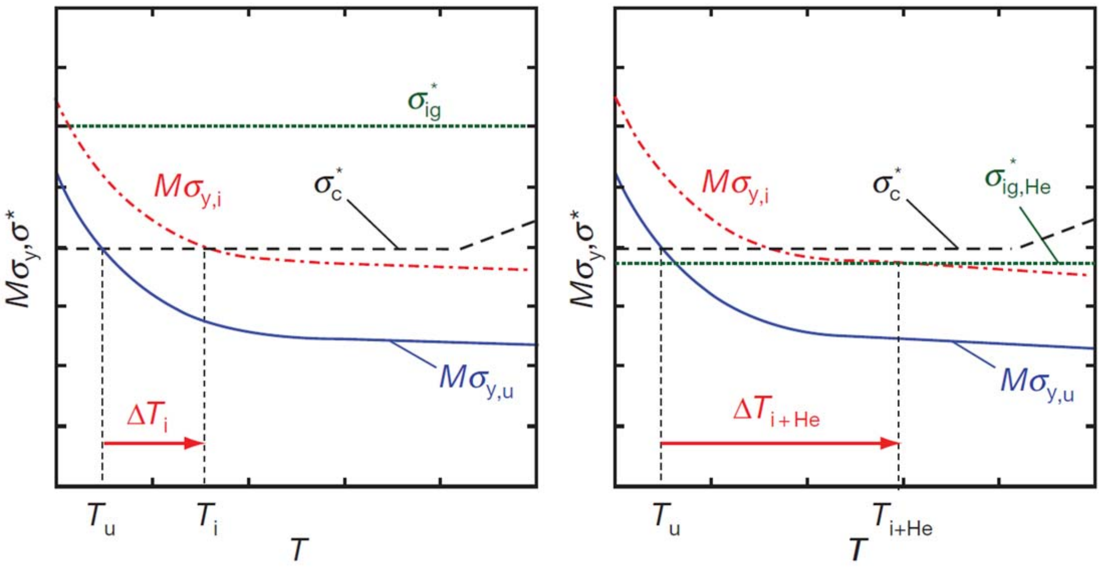

Fig.4.3: Sketch showing the mechanisms for irradiation-induced hardening (increase of yield stress, Δσ$_y$) and helium-induced grain boundary weakening effects (decrease of the intergranular fracture stress, σ$_{ig}$*) that elevate the brittle to ductile transition temperature [171].

The defect clusters produced in spallation irradiation mainly contribute to the hardening effect intra-grains, while the helium bubbles induced in spallation irradiation result in the combined effects of pronounced intra-granular hardening and weakening of grain boundaries strength. As shown in Fig. 3.5, the hardening continuously increases with dose under the present irradiation conditions. The Hardness is about 330 at 10.7 dpa, about 370 at 15.5 dpa and about 390 at 19.6 dpa. The corresponding yield stress is about 965 MPa as measured for the 10.7 dpa specimen 1080 and 1150 MPa at 15.5 dpa and 19.6 dpa, respectively, if taking the same converting factor of 2.92 as calculated from the 10.7 dpa specimen. On the other hand, the cohesion strength of grain boundaries should be weakened. This effect should increase with increase of helium concentration. It might also increase slightly with irradiation temperature in the low temperature regime because of faster helium diffusion at higher temperatures. From the fracture mode of the specimens, one can expect that for the specimen of 10.7 dpa tested at RT, although significant hardening effect appeared, both intergranular and cleavage fracture stress are σ$_{ig}$* and σ$_c$* still higher than the actual yielding stress, which leads to ductile fracture of the specimen. At 19.6 dpa, Mσ$_y$ increased to a level clearly higher than σ$_{ig}$* and σ$_c$* not only at RT but also at 300 °C. Meanwhile, the GBs are strongly weakened that results in $\sigma_{ig}^* < \sigma_c^*$, leading to intergranular fracture dominated situation. At intermediate doses of 15.2 and 15.8 dpa of the four specimens, the fracture surface of the 15.8 dpa specimen tested at RT appeared about half-to-half of intergranular and transgranular cleavage fracture. This implies that $\sigma_{ig}^* \sim \sigma_c^*$, and both are greater than $M\sigma_y$. Whereas the mixed fracture mode of ductile and transgranular cleavage for the 15.2 dpa specimen tested at 250 °C indicates that σ_c^* is about the same as $M\sigma_y$. For $\sigma_c^* \sim 2000$ MPa, M is about 1.8-2.0, which is in agreement with usual expectations.

Henry [79] et al obtained the similar result in T91 and EM10 specimens irradiated in the same irradiation experiment, STIP II. The high dose of specimens of 18-20 dpa and tested at RT and 250 °C exhibited no necking appearance and intergranular and cleavage fracture surface. At 350 °C a T91 specimen also showed fully brittle fracture, while an EM10 specimen demonstrated some necking and rather ductile fracture with numerous secondary cracks on fracture surface. However, except for two specimens of 19.3 dpa tested at RT that failed in elastic regime, all other specimens broke after yielding. The two specimens that failed in elastic regime still reached a stress level of about 1100 MPa, higher than that of the F82H specimens tested in this work. A clear difference between F82H, T91 and EM10 steels is that the grain size of T91 and EM10 are smaller than that of F82H.

In this study, although just Eurofer97 and MANET-II specimens of 19.8 dpa were tested, they did show a behavior different from that of F82H, rather similar to that of T91 and EM10, as shown in Fig. 3.2 and 3.3. The Eurofer97 specimen of 19.8 dpa exhibited about 1% elongation at RT, and the MANET-II specimen of 19.8 dpa presented more than 2% elongation at 300 °C. A noteworthy observation is that there were many secondary cracks on the fracture surfaces of the Eurofer97 and MANET-II specimens, although the fracture surfaces were dominant with intergranular and transgranular features. The secondary cracks were mostly along grain boundaries. The formation and opening of secondary cracks may contribute to the main part of the elongation of the specimens.

4.4 Deformation microstructure and fracture mechanisms

In subsections 3.3.2 and 3.3.3, the deformation microstructures of irradiated FM steels have been presented in details. Dislocation tangles and cells formed during plastic deformation are hard to be distinguished from the pre-existing dislocation structures in FM steel. They are formed by classical mechanisms of dislocation nucleation, propagation and accumulation. Phenomenological laws based on dislocation dynamics of the strain-hardening were already used and shown to reproducing well the experimental curves of FM steels [174]. They will not be discussed here. Only the deformation mechanisms consisting of dislocation motion in defect free channels and deformation twinning will be discussed in this section.

4.4.1 Relationship of defect free channels with deformation and fracture

Defect free channels were only observed in the region close to the necking area of the F82H specimen (K19) irradiated at 15.2 dpa/1305 appm He and tested at 250 °C, and of MANET-II specimen irradiated at 11.1 dpa and tested at room temperature. The K19 specimen fractured in relatively ductile mode but without strain-hardening. This behavior was significantly different from F82H specimen (K22) irradiated in similar irradiation condition (15.8 dpa/1350 appm He) that failed totally brittle in the elastic loading when tested at RT. In literature, most of the defect free channel observations have been done in different fcc irradiated metals such as Cu, Au, Ni and austenitic steels [21, 90-95, 100, 102, 103, 108, 175-177]. However, it is also been observed in bcc irradiated metals: irradiated iron [46, 105], vanadium and vanadium alloy [22, 104]. To our knowledge, for FM steels, defect free channels were observed only once in neutron irradiated F82H [106].

Defect free channels are responsible for plastic flow localization, and consequently of inhomogeneous deformation, which is usually considered as the main cause for the observed loss of ductility. The existence of defect free channels in relatively brittle sample is the signature of dislocation activity and plastic deformation occurring in the neck region prior to failure. Although the total elongation of the F82H specimen in which the channels were observed is only 4%, the reduction area on the fracture surface is 25%, which means that the necking was localized in a small volume. According to the SEM observations of fracture surface, plenty of shallow dimples were observed. All these results attest that defect free channels do not lead to intergranular brittle fracture but are rather related to the loss of elongation and ductility. Nevertheless, many researchers consider that defect free channels are directly involved in intergranular cracking, especially in irradiation assisted stress corrosion cracking (IASCC) research community. For instance, Evrard and Sauzay [24, 178] studied the effect of dislocation channel on intergranular microcrack nucleation during tensile deformation of pre-irradiated austenitic stainless steels. They performed finite element computations within the framework of crystal plasticity, from which they showed the influence of the geometry of the channel (width, length, orientation with respect to the grain boundary) on the grain boundary stress field. The results of the simulations are further elaborated into a micro-crack nucleation criterion of Griffith type, which properly describes the grain boundaries characteristics on intergranular cracking irradiated austenitic stainless steels. In a review article of Was et al. [23], it could not be concluded which of the emission or the termination of dislocation channels at grain boundaries is most effective in inducing IGSCC. It was also outlined that the exact role of localized deformation in IGSCC remains largely not understood.

In this work, the defect free channels do not seem to have a direct relation with the intergranular fracture. They certainly correlate to some extend with the loss of ductility following irradiation, but their exact role in the ductility reduction remains in all cases difficult to quantify. Indeed, the overall plastic behavior of the irradiated FM steels is a very complex problem that cannot be reduced to a simplistic view considering that the plastic deformation strictly occurs in the defect-free channels. For instance the interaction between different channels, the density of channels and its evolution with strain have to be taken into account, as well as the ferritic matrix surrounding the channels that must deform to fulfill the displacement compatibility. In an attempt to address these issues, a two dimensional finite element model was developed by Odette et al. [179] where soft bands where imbedded in a stronger matrix. In particular, the authors pointed out that flow localization in defect-free channel is not a prerequisite to explain the low uniform elongation of irradiated materials and that a complete and comprehensive description of the reduction of the uniform elongation must take into account the concurrent deformation of the strong matrix and soft channels.

The exact role of defect free channels in the irradiated FM steels can be summarized as follows. The intersection of these soft bands and grain boundaries can indeed cause large stress field nearby grain boundaries. These large stresses conjugate with elemental segregation and helium or hydrogen distribution along grain boundaries produced by transmutation can weaken the strength of grain boundaries. These combined effects on the material may cause intergranular fracture as shown by some researcher. However, for the irradiation conditions where we observed defect-free channels, no intergranular fracture took place, indicating that they mainly play a role in plastic deformation.

4.4.2 The nucleation conditions of deformation twinning in FM steels and its effect on brittle fracture

One of the most interesting observations of this work is that deformation twinning occurs underneath the fracture surfaces of the completely brittle fractured samples including the 15.8 dpa F82H specimen tested at RT, the 19.6 dpa F82H specimen tested at 300 °C and the 19.8 dpa Eurofer97 specimen tested at RT. The F82H specimens with larger grain size (86 µm) fractured in the elastic regime without measurable macro-plasticity and with totally intergranular and cleavage fracture surface, while the Eurofer97 specimen with smaller grain size (16 µm) fractured at about 1% of elongation after yielding and with fully intergranular and cleavage fracture surface as well. So far, the deformation twinning has been commonly observed in irradiated austenitic steels by different investigators [103, 107, 109, 175-177]. However, to our knowledge twinning has never been observed in irradiated FM steels. We also emphasize that, up to now, twinning was found only at high dose obtained in spallation environment.

We recall that the creation of a twin region is a two-step process involving the nucleation of a small twin followed by its growth. In general, the critical event for twinning is nucleation that usually necessitates a much lower stress than that for propagation [180].

Twin-nucleation:

The different models proposed to predict the twinning stress in bcc metals and alloys lead to a very large difference in the twinning stress value. For instance, Ojha et al. [181] provides the twinning stress in Fe calculated with five different models that was found to range from 430 MPa to 7050 MPa. All these models invoke the stacking fault energy (in bcc alloys, the stacking refers to the $\{112\}$ planes) that can be, depending on the model considered, either the stable stacking fault energy, the unstable stacking fault energy, or the twin boundary migration energy. These authors developed a model to calculate the general plane fault energy (GPFE) from atomistic simulations of Fe, Fe-50%Cr, Fe-25%Ni and Fe-3%V. To calculate the twinning stress, an initially dissociated 1/2<112> on three $\{112\}$ planes is considered that glide under the application of a stress on their respective slip until the two trailing dislocations cross slip onto two slip planes parallel to that of the leading partial dislocation creating a twin nucleus. By taking into account the line energy of the partial dislocation, the interaction energy between them and the work done by the applied stress, the critical stress for twin nucleation was determined. A very good agreement was found between the calculated twinning stress and the experimentally determined one for all the materials mentioned above. These results are presented in Fig. 4.4. We used this plot to make a rough estimate of the twinning shear stress in our FM steel, which we assume to lie between the value of Fe and Fe-50%Cr. The plot in Fig. 4.5 indicates that the *critical twin nucleation effective shear stress* $\tau_{tw,nucl}$ is about 200 MPa. This value needs to be converted into the *critical applied uniaxial tensile stress for twin nucleation* $\sigma_{tw,nucl}$

by considering a geometrical Taylor's factor and by adding the athermal long range component σ_{ath} as :

$$\sigma_{tw,nucl} = M_T\, \tau_{tw,nucl} + \sigma_{ath} \tag{4.7}$$

with a Taylors' factor of 3, and σ_{ath} of about 500 MPa for FM steels as reported by Spätig et al. [174]. The critical applied uniaxial tensile stress for twin nucleation reads then 1100 MPa. With such a high stress value, it is clear that deformation twinning can dominate deformation only in some extreme conditions, such as low temperature and/or high strain rate [113-119], for which the critical stress for slip is significantly greater than 1100 MPa. It is clear that this estimated stress value for twin nucleation only gives an indication of the stress level needed to trigger twining in FM steels. It is noted that this stress corresponds to the yield stress measured by tensile stress in Eurofer97 at loading rate of 10^{-4} s^{-1}, which was found to be 1100 MPa. We conclude that the transition between slip and twinning in unirradiated should occur at temperature close to LN2 temperature where dislocation slip occurs.

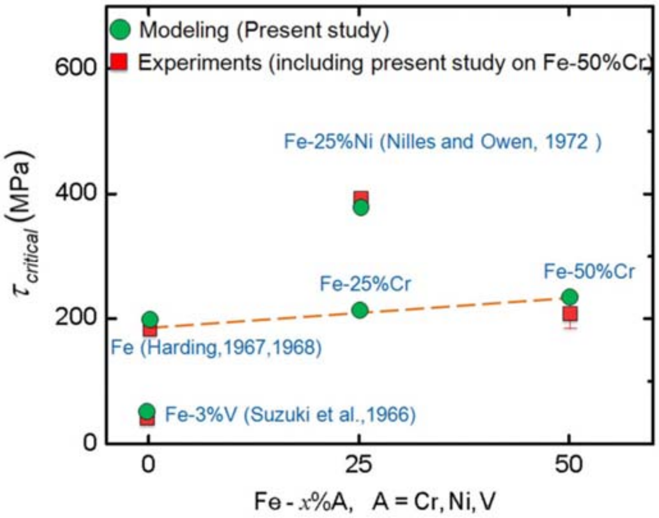

Fig 4.4: Experimental and calculated twinning nucleation critical shear stress for Fe and Fe-based alloys, according to [181].

In terms of the applied tensile stress, the critical condition for twinning initiation in irradiated specimens must be different from those in unirradiated specimens, for the reason explained below. At first glance, the occurrence of twinning in some irradiated specimens appears contradictory with $\sigma_{tw,nucl}$ = 1100 MPa. Indeed, for two F82H specimens over three, namely specimens at 15.8 dpa tested at RT and 19.6 dpa tested at 300 °C, the tensile stresses at brittle fracture were lower than the estimated $\sigma_{tw,nucl}$. We recall that the tensile fracture stress of the 15.8 dpa specimen was 1033 MPa while it was 822 MPa for the 19.6 dpa specimen. The discrepancy between the estimated $\sigma_{tw,nucl}$ at 1100 MPa and these experimental values is likely to be linked to the weakening of the grain boundaries cohesion. As discussed in the Section 4.3 above, the accumulation of He on the grain boundaries, beyond a bulk threshold of typically 500 appm He, results in a strong decrease of the intergranular fracture stress σ_{ig}^*. Thus, for specimens at high dose and high helium content, intergranular cracking may already occur in the elastic regime because the intergranular fracture stress can become lower than the critical stress for normal dislocation slip deformation so that intergranular micro-cracking occurs. When intergranular micro-crack are formed, they act as local stress intensity factors, raising the stress level at the crack tip σ_n according to the equation $\sigma_n = M\sigma_y$, with M being in the range 1.5-3. Therefore, intergranular cracking must be sufficient to trigger twinning through the stresss amplification at the micro-crack tips. In addition, since $\sigma_{y,irr}$ is greater than $\sigma_{y,unirr}$, the local stress $\sigma_{n,irr}$ at the tip of a nascent intergranular micro-crack or of an already existing micro-crack in irradiated FM steel will be larger than $\sigma_{n,unirr}$ according to the following scaling law:

$$\sigma_{n,irr} = \sigma_{n,unirr} \text{ x } (\sigma_{y,irr}/\sigma_{y,unirr}) \tag{4.8}$$

Thus, the ratio $(\sigma_{y,irr}/\sigma_{y,unirr})$ provides an additional increase of the stress at the micro-crack tip in irradiated as compared with unirradiated material. The envisaged mechanisms are depicted in (see Fig. 4.5), where an iso-stress contour for the normal stress component to the crack plane is qualitatively shown as well as the twins that form in the crack wave. Either the twins form in the process zone as a result of the very high stress field and strain gradient, which needs to be accommodated (Fig. 4.5 left), or they initiate at the interface between a crack and a precipitate (Fig. 4.5 right). Note that such a process involves a running crack and consequently has to be regarded as a highly dynamic process. It is also well known that the high stresses and strains are localized in a small zone around the crack. In other words, large stress and strain gradients exist ahead of the crack tip. So the twins nucleate very close to the crack and propagate away from the crack tip over a small distance. The observation of twin configuration in Fig. 3.33 strongly supports the view that the process of nucleation takes place during crack propagation. The twins appear wider close to the crack curve than further away, which shows that the twin propagated from the crack surfaces inside the material, all along the crack wake.

Twin-propagation:

It is well known that the stress to propagate a twin is significantly lower than that to nucleate it. So when the conditions for twin nucleation are met, the stress to overcome the irradiation-induced obstacles by the propagation partial dislocation should be sufficient. Since twining deformation involves the propagation of a single partial dislocation per glide plane, the irradiation-induced defect cannot be completely destroyed. It is indeed believed that the clearing of the defects requires the sweeping of many dislocations. This is consistent with our current observation in Fig. 3.35 revealing that both defect clusters and helium bubbles still exist in the twinning bands. Furthermore, for helium bubbles, for instance, the average size and number density (1.82 nm/1.04E+24m^{-3}) are approximately similar as those in the parent matrix (1.93 nm/1.07E+24 m^{-3}) in 19.6dpa K20 specimen, whereas, for defect clusters, number density and nature of defect clusters are hard to be determined in this study because of very thin thickness of the bands (34 nm in average).Consequently, in irradiated metals, the critical stress for the normal dislocation slip deformation depends on the required stress to overcome the pinning of irradiated defects, while the critical stress for the twinning deformation depends on the required stress to nucleate the first stacking fault.

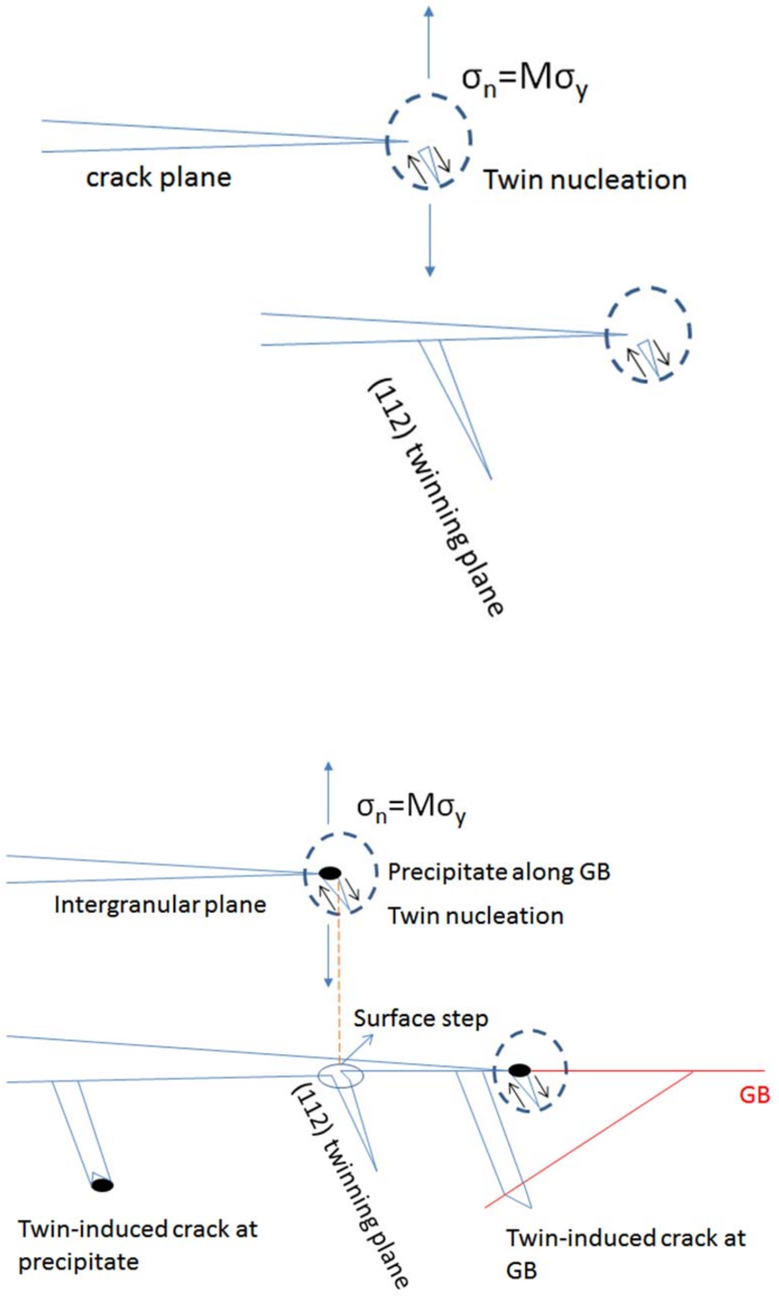
σn=Mσy
crack plane
Twin nucleation
(112) twinning plane
σn=Mσy
Precipitate along GB
Intergranular plane
Twin nucleation
Surface step
(112) twinning plane
GB
Twin-induced crack at precipitate
Twin-induced crack at GB

Fig.4.5: Illustration of the envisaged mechanisms of twin formation in the wake of a running crack. Upper: nucleation of a twin in the high-stress process zone at the crack tip. Lower: nucleation of a crack at the interface twin/precipitate and at the interface twin/GB.

Twinning-induced cracking:

From the discussion on twin-nucleation, the sequence of event proposed for the irradiated material is: 1) formation of intergranular micro-cracks followed by, 2) formation of the twins in the process zone around the micro-crack tip. Once twins are formed, they can act as micro-crack initiator as suggested by the observations in Fig 3.30, where cracks resulting from the interaction of a twin with large precipitates/carbides at prior austenite grain boundaries. The existence of such micro-cracks indicates that twinning is likely to induce additional micro-cracking as explained schematically in Fig. 4.5. In polycrystals, each grain is constrained by its neighboring grains through grain boundaries. A twin formed in grain 1 interacts with the corresponding GB. To accommodate the lattice rotation caused by twinning in grain 1, the GB is subjected to a displacement Δ proportional to the twin width [126, 127]. However, plastic deformation in grain 2 and in the adjacent to the twin boundary is limited since the dislocations are strongly pinned by irradiation-induced clusters and helium bubbles in high dose specimens. To fulfill the displacement continuity at the grain and twin boundaries without plasticity, the displacements are essentially elastic and lead to high stress in GB .The stress increases as the twin in grain 1 widens, until the GB is pulled open to nucleate a GB crack [126]. Moreover, compared with nanocrystalline materials or the low temperature testing of unirradiated materials [118, 119, 127, 132, 137, 139, 182], this high stress effect acts synergistically with the weakening of the GB due to helium accumulation and/ or element segregation caused by irradiation. Therefore, particularly for the specimens (15.8 dpa and 19.6 dpa F82H and 19.8 dpa Eurofer97 in this study) irradiated to high dose with high helium contents, the crack opening is facilitated due to the combined effects of stress concentration induced by twinning-GBs intersection and weakening of GBs strength caused by irradiation.

5. Conclusions

Three different Ferritic/Martensitic (FM) steels F82H, Eurofer97 and Manet II were irradiated to 10.7-19.8 dpa and 850-1750 appm He at temperatures of 166 to 304 °C in STIP-II. In order to investigate the fracture behaviors and the embrittlement of FM steels induced by combined effect of displacement damage and helium after spallation irradiation, tensile tests of the irradiated specimens were conducted at different temperatures. Furthermore, successive tensile tests together with SEM observations were performed at 25 °C on irradiated F82H and MANET II steels to study micro-crack initiation and propagation features. Hardness was measured on the electropolished tensile specimens before testing. TEM-lamella samples were prepared by FIB in undeformed regions of the F82H specimens of different doses and the 19.8 dpa MANET II and the 19.8 dpa Eurofer97 tensile specimens to investigate irradiation induced microstructural changes such as defect clusters and helium bubbles, and in deformed areas, particularly directly underneath fracture surfaces, of the specimens to observe the deformation microstructure.

Mechanical properties of FM steels after irradiation

The tensile test results show that all the irradiated specimens exhibit significant hardening and loss of ductility as compared with the unirradiated specimens. The F82H specimen of 10.7 dpa possesses pretty large total elongation at RT, although uniform elongation decreased to less than 1%. Fracture surface is dominant in dimple-ductile. The 15.8 dpa F82H specimen tested at RT failed in elastic regime without any plastic deformation, in a mixed transgranular cleavage and intergranular fracture surface. The specimen of 15.2 dpa F82H specimen tested at 250 °C show a small amount of ductility with a mixed ductile and quasi-cleavage fracture mode, while the 19.6 dpa F82H specimen tested at 300 °C present fully embrittlement with intergranular dominant fracture mode.

Compared with F82H, the brittle fracture mode in MANET II and Eurofer97 is different. The Eurofer97 specimen of 19.8 dpa presented about 1% elongation at RT with a mixed intergranular and cleavage fracture mode, and the MANET specimen of 19.8 dpa demonstrated more than 2% elongation at 300 °C with an intergranular dominant fracture mode together with a small portion in dimple fracture mode. The difference is attributed to the smaller grain size in Eurofer97 and MANET II and the main part of elongation is speculated to be induced by many secondary cracks.

Vickers hardness was measured on the tensile specimens before tensile testing. The hardness results demonstrate a clearly increasing trend with increasing irradiation dose and helium content in F82H, Eurofer97 and MANET II specimens. Especially, the increase of hardness was still not saturated at the highest dose (20.4 dpa), which is attributed to the helium effect on hardening.

The fracture behaviors could be interpreted with the combined effects of the pronounced intra-granular hardening induced by defect clusters and helium bubbles and the helium weakening on the grain boundary strength.

Micro-crack initiation and propagation behavior

The successive small punch (SP) tests accompanying with SEM observations performed on unirradiated T91 indicated that micro-cracks initiated from the inclusions when tested at RT, whereas on grain boundaries (GBs) or lath boundaries (LBs) when tested at LN2 temperature.

The micro-crack initiation on side surfaces was observed in irradiated F82H and MANET II tensile specimens during successive tensile testing. This crack initiation is attributed to the brittle layer produced by EDM. In the F82H specimen of 11.1 dpa the cracks were arrested by GBs, while in the specimen of 15.8 dpa fast crack propagation resulted in fracture in elastic regime and the crack propagation could not be captured during the test.

After removing about 20 µm thickness from each surface by electro-polishing, first cracks were just observed on 4.6% strain level in MANET II specimen of 11.1 dpa during successive tensile testing.

As-irradiated microstructures of FM steels

The as-irradiated microstructure of F82H specimens of 12.3 to 20.4 dpa was investigated by TEM. All the TEM samples were prepared from un-deformed region of tensile specimens.

Small defect clusters were observed in the 12.3 dpa specimen, together with few large defect clusters with loop-shape. In the specimens of 17.2, 17.7 and 20.4 dpa, many large dislocation loops were seen besides the small clusters. In addition, helium bubbles were observed in all of these four specimens. The average size of defect clusters (including loops) increases from 4.2 nm to 11.8 nm when dose increasing from 12.3 dpa to 20.4 dpa, whereas the number density does not show a significant change.

Helium bubbles are very small in the specimen of 12.3 dpa, 1015 appm He irradiated at 175 °C. The average size of visible helium bubbles is about 1 nm. The size of bubbles increases with irradiation dose and is about 1.93 nm in specimen irradiated to 20.4 dpa, 1795 appm He at 317 °C. The values of number density of helium bubble in specimens of 12.3 dpa and 17.2 dpa are believed to be underestimated due to the invisibility of very tiny bubbles (<1 nm) in the specimen of 12.3 dpa and the reduced contrast in the relatively thick region (about 50 nm) of the specimen of 17.2 dpa.

The barrier strength of defect clusters was assessed as 0.37±0.1 in dispersed barrier model based on the TEM results of the irradiated F82H specimens.

Defect-free channeling in irradiated FM steels

The localized deformation bands as defect free channels along $\{110\}$ and $\{112\}$ slip plane were observed in the F82H specimen of 15.2 dpa tested at 250 °C defect free channels with $\{110\}$ slip plane were were observed in the MANET II specimen irradiated to 11.1 dpa tested at RT. The width of the channels is approximate 100 nm.

Deformation twinning in brittle fractured irradiated FM steels

Interestingly, deformation twins were observed in the 15.8 and 19.6 dpa F82H, 19.8 dpa Eurofer97 fractured samples. For F82H specimen, twins were observed underneath both intergranular and cleavage fracture surface, while it was only observed underneath intergranular fracture surface in Eurofer97 specimen. The detailed features are as follows.

- The twins were observed in the regions both directly under fracture surfaces and a couple of micrometers away from fracture surface. There was only one twinning system activated in the same prior austenite grain.
- The twinning plane was identified as (112) which is the typical twinning plane in BCC metals and the thickness varied from 10 to 190 nm with an average thickness of 34 nm.
- The thickness of twins becomes thinner gradually with distance away from a fracture surface and stopped in the matrix finally, which indicates that these twins were initiated on the fracture surface.
- Twins were seen to be arrested in the vicinities of grain boundaries and large precipitates, where it could not propagate to the adjacent grain. However, twins could penetrate martensitic lath boundaries.
- Defect-clusters and helium bubble structures observed inside the twinning bands were similar to that outside twins. For instance, in the F82H specimen irradiated to 19.6 dpa, 1740 appm at 305 °C and tested at 300 °C, the average size and number density of helium bubbles inside of the twinning band (1.82 nm/1.04E+24 m^{-3}) are approximately the same as those in the parent matrix (1.93 nm/1.07E+24 m^{-3}).

The nucleation of deformation twins is attributed to the high stress level caused by irradiation hardening combined with stress concentration in front of crack tip. Micro-crack initiation was observed to be induced by the twin-boundary or twin-precipitates interaction, which is contemplated to be facilitated due to the combined effects of stress concentration induced by twin-GB intersection as well as the weakening of the grain boundaries cohesion induced by helium.

References

[1] M. Tamura, H. Hayakawa, M. Tanimura, A. Hishinuma, T. Kondo, Development of potential low activation ferritic and austenitic steels, Journal of Nuclear Materials, 141-143 (1986) 1067-1073.

[2] Y. Dai, Suitability of steels as ESS mercury target container materials, In Proceedings of the 13th Meeting of the International Collaboration on Advanced Neutron Sources, ESS-PM-4 (1995) ICANS-XIII.

[3] R.L. Klueh, A.T. Nelson, Ferritic/martensitic steels for next-generation reactors, Journal of Nuclear Materials, 371 (2007) 37-52.

[4] R.L. Klueh, D.J. Alexander, Irradiation effects on impact behavior of 12Cr-1MoVW and 2 1/4 Cr-1Mo steels, in: ASTM Special Technical Publication, 1992, pp. 1256-1266.

[5] R.L. Klueh, D.J. Alexander, Tensile and charpy impact properties of irradiated reduced-activation ferritic steels, in: ASTM Special Technical Publication, 1999, pp. 911-930.

[6] Y. Dai, P. Marmy, Charpy impact tests on martensitic/ferritic steels after irradiation in SINQ target-3, Journal of Nuclear Materials, 343 (2005) 247-252.

[7] Y. Dai, J. Henry, Z. Tong, X. Averty, J. Malaplate, B. Long, Neutron/proton irradiation and He effects on the microstructure and mechanical properties of ferritic/martensitic steels T91 and EM10, Journal of Nuclear Materials, 415 (2011) 306-310.

[8] X. Jia, Y. Dai, Microstructure of the F82H martensitic steel irradiated in STIP-II up to 20&#xa0;dpa, Journal of Nuclear Materials, 356 (2006) 105-111.

[9] H. Schroeder, Batfalsky, P.,, The dependence of the high temperature mechanical properties of austenitic stainless steels on implanted helium, Journal of Nuclear Materials, 117 (1983) 287.

[10] K. Kesternich, Rothaut, J.,, Reduction of helium embrittlement in stainless steel by finely dispersed TiC precipitates, Journal of Nuclear Materials, 103&104 (1981) 845.

[11] B.M. Oliver, Y. Dai, R.A. Causey, Helium and hydrogen release measurements on various alloys irradiated in SINQ, Journal of Nuclear Materials, 356 (2006) 148-156.

[12] B.M. Oliver, Y. Dai, Helium and hydrogen measurements on pure materials irradiated in SINQ Target 4, Journal of Nuclear Materials, 386-388 (2009) 383-386.

[13] Y. Dai, Y. Foucher, M.R. James, B.M. Oliver, Neutronics calculation, dosimetry analysis and gas measurements of the first SINQ target irradiation experiment, STIP-I, Journal of Nuclear Materials, 318 (2003) 167-175.

[14] K. Shiba, A. Hishinuma, Low-temperature irradiation effects on tensile and Charpy properties of low-activation ferritic steels, Journal of Nuclear Materials, 283–287, Part 1 (2000) 474-477.

[15] E. Wakai, S. Jitsukawa, H. Tomita, K. Furuya, M. Sato, K. Oka, T. Tanaka, F. Takada, T. Yamamoto, Y. Kato, Y. Tayama, K. Shiba, S. Ohnuki, Radiation hardening and -embrittlement due to He production in F82H steel irradiated at 250&#xa0;°C in JMTR, Journal of Nuclear Materials, 343 (2005) 285-296.

[16] P. Jung, J. Henry, J. Chen, J.C. Brachet, Effect of implanted helium on tensile properties and hardness of 9% Cr martensitic stainless steels, Journal of Nuclear Materials, 318 (2003) 241-248.

[17] H. Ullmaier, J. Chen, Low temperature tensile properties of steels containing high concentrations of helium, Journal of Nuclear Materials, 318 (2003) 228-233.

[18] A. Hasegawa, Nogami, S., & Imaseki, K., High Temperature Helium Embrittlement of 316FR Steel, CYRIC annual report, 2009 (2009) 31 - 38.

[19] H. Trinkaus, On the modeling of the high-temperature embrittlement of metals containing helium, Journal of Nuclear Materials, 118 (1983) 39-49.

[20] L.K. Mansur, M.L. Grossbeck, Mechanical property changes induced in structural alloys by neutron irradiations with different helium to displacement ratios, Journal of Nuclear Materials, 155–157, Part 1 (1988) 130-147.
[21] Y. Dai, PhD Thesis 1388, Ecole Polytechnique Federale De Lausanne, (1995).
[22] T.S. Byun, N. Hashimoto, K. Farrell, E.H. Lee, Characteristics of microscopic strain localization in irradiated 316 stainless steels and pure vanadium, Journal of Nuclear Materials, 349 (2006) 251-264.
[23] G.S. Was, D. Farkas, I.M. Robertson, Micromechanics of dislocation channeling in intergranular stress corrosion crack nucleation, Current Opinion in Solid State and Materials Science, 16 (2012) 134-142.
[24] P. Evrard, M. Sauzay, Modelling of the effect of dislocation channel on intergranular microcrack nucleation in pre-irradiated austenitic stainless steels during low strain rate tensile loading, Journal of Nuclear Materials, 405 (2010) 83-94.
[25] W. Schilling, H. Ullmaier, Physics of Radiation Damage in Metals, in: Materials Science and Technology, Wiley-VCH Verlag GmbH & Co. KGaA, 2006.
[26] M.T. Robinson, Basic physics of radiation damage production, Journal of Nuclear Materials, 216 (1994) 1-28.
[27] A. International, Standard particle for neutron radiation damage simulation by charged-particle irradiation, ASTM International, (2009).
[28] T.D. de la Rubia, R.S. Averback, H. Hsieh, R. Benedek, Molecular dynamics simulation of displacement cascades in Cu and Ni: Thermal spike behavior, Journal of Materials Research, 4 (1989) 579-586.
[29] D.J. Bacon, T. Diaz de la Rubia, Molecular dynamics computer simulations of displacement cascades in metals, Journal of Nuclear Materials, 216 (1994) 275-290.
[30] H. Ullmaier, F. Carsughi, Radiation damage problems in high power spallation neutron sources, Nuclear Instruments and Methods in Physics Research Section B: Beam Interactions with Materials and Atoms, 101 (1995) 406-421.
[31] C.-C. Fu, J.D. Torre, F. Willaime, J.-L. Bocquet, A. Barbu, Multiscale modelling of defect kinetics in irradiated iron, Nat Mater, 4 (2005) 68-74.
[32] G.S. Was, Fundamentals of Radiation Materials, Springer, (2007).
[33] S.J. Zinkle, 1.03 - Radiation-Induced Effects on Microstructure*, in: R.J.M. Konings (Ed.) Comprehensive Nuclear Materials, Elsevier, Oxford, 2012, pp. 65-98.
[34] S.J. Zinkle, B.N. Singh, Analysis of displacement damage and defect production under cascade damage conditions, Journal of Nuclear Materials, 199 (1993) 173-191.
[35] R.S. Averback, T.D. de la Rubia, Displacement Damage in Irradiated Metals and Semiconductors, in: E. Henry, S. Frans (Eds.) Solid State Physics, Academic Press, 1997, pp. 281-402.
[36] C.C.R.A. Agullo-Lopez. F., Point Defects in Materials, Academic Press: San Diego, CA, (1988) p 445.
[37] Y. Shimomura, H. Fukushima, M.W. Guinan, Cascade structure in low temperature fission and fusion neutron-irradiated metals, Journal of Nuclear Materials, 174 (1990) 210-219.
[38] M. Kiritani, N. Yoshida, H. Takata, Y. Maehara, Growth of Interstitial Type Dislocation Loops and Vacancy Mobility in Electron Irradiated Metals, Journal of the Physical Society of Japan, 38 (1975) 1677-1686.
[39] L.K. Mansur, Theory of transitions in dose dependence of radiation effects in structural alloys, Journal of Nuclear Materials, 206 (1993) 306-323.
[40] R. Sizmann, The effect of radiation upon diffusion in metals, Journal of Nuclear Materials, 69–70 (1978) 386-412.
[41] N. Yoshida, M. Kiritani, Point Defect Clusters in Electron-Irradiated Gold, Journal of the Physical Society of Japan, 35 (1973) 1418-1429.
[42] M. Kiritani, electron radiation damage of metals and nature of point defects by high voltage electron microscopy, International conference on radiation damage in metals, CONF-751006-P2, II (1975) 695-714.

[43] B.L. Eyre, Transmission electron microscope studies of point defect clusters in fcc and bcc metals, Journal of Physics F: Metal Physics, 3 (1973) 422.
[44] M. Kiritani, H. Takata, Dynamic studies of defect mobility using high voltage electron microscopy, Journal of Nuclear Materials, 69–70 (1978) 277-309.
[45] M. Eldrup, B.N. Singh, S.J. Zinkle, T.S. Byun, K. Farrell, Dose dependence of defect accumulation in neutron irradiated copper and iron, Journal of Nuclear Materials, 307–311, Part 2 (2002) 912-917.
[46] S.J. Zinkle, B.N. Singh, Microstructure of neutron-irradiated iron before and after tensile deformation, Journal of Nuclear Materials, 351 (2006) 269-284.
[47] M. Li, M. Eldrup, T.S. Byun, N. Hashimoto, L.L. Snead, S.J. Zinkle, Low temperature neutron irradiation effects on microstructure and tensile properties of molybdenum, Journal of Nuclear Materials, 376 (2008) 11-28.
[48] M. Eldrup, M. Li, L.L. Snead, S.J. Zinkle, Characterization of defect accumulation in neutron-irradiated Mo by positron annihilation spectroscopy, Nuclear Instruments and Methods in Physics Research Section B: Beam Interactions with Materials and Atoms, 266 (2008) 3602-3606.
[49] A.F. Rowcliffe, E.H. Lee, High temperature radiation damage phenomena in complex alloys, Journal of Nuclear Materials, 108–109 (1982) 306-318.
[50] J.J. Kai, R.L. Klueh, Microstructural analysis of neutron-irradiated martensitic steels, Journal of Nuclear Materials, 230 (1996) 116-123.
[51] R.L. Klueh, Harries, D. R., High-Chromium Ferritic and Martensitic Steels for Nuclear Applications, W. Conshohocken, PA: ASTM, (2001) p 221.
[52] P.J. Maziasz, Formation and stability of radiation-induced phases in neutron-irradiated austenitic and ferritic steels, Journal of Nuclear Materials, 169 (1989) 95-115.
[53] M.L. Jenkins, Kirk, M.A, Characterization of Radiation Damage by Transmission Electron Microscopy, Taylor&Francis Group, (2000).
[54] D.B. Williams, Carter, C.B., Transmission Electron Microscopy, A Textbook for Materials Science, Springer 2nd edition (2009).
[55] P.B. Hirsch, Howie, A., Nicholson, R.B., Pashley, D.W., Whelan, M.J., Electron Microscopy of thin crystals, Krieger Pub Co, (1977).
[56] R.W. Conn, E.E. Bloom, J.W. Davis, R.E. Gold, R. Little, K.R. Schultz, D.L. Smith, F.W. Wiffen, Lower Activation Materials and Magnetic Fusion-Reactors, Nucl Technol-Fusion, 5 (1984) 291-310.
[57] G.J. Butterworth, O.N. Jarvis, Comparison of transmutation and activation effects in five ferritic alloys and aisi 316 stainless steel in a fusion neutron spectrum, Journal of Nuclear Materials, 123 (1984) 982-988.
[58] N.M. Ghoniem, A. Shabaik, M.Z. Youssef, development of low activation vandium steel for fusion applications, in, 1984, pp. 201-208.
[59] R.L. Klueh, E.E. Bloom, The development of ferritic steels for fast induced-radioactivity decay for fusion reactor applications, Fusion Engineering and Design, 2 (1985) 383-389.
[60] D. Dulieu, K.W. Tupholme, G.J. Butterworth, Development of low-activation martensitic stainless steels, Journal of Nuclear Materials, 141-143 (1986) 1097-1101.
[61] T. Noda, F. Abe, H. Araki, M. Okada, Development of low activation Ferritic steels, Journal of Nuclear Materials, 141-143 (1986) 1102-1106.
[62] R.L. Klueh, D.S. Gelles, T.A. Lechtenberg, Development of ferritic steels for reduced activation: The US program, Journal of Nuclear Materials, 141-143 (1986) 1081-1087.
[63] D.S. Gelles, Klueh, R.L., Okada, M. , Reduced Activation Materials for Fusion Reactors, American Society for Testing and Materials, ASTM STP 1047 (1990) p 113.
[64] P.J. Maziasz, R.L. Klueh, J.M. Vitek, Helium effects on void formation in 9Cr-1MoVNb and 12Cr-1MoVW irradiated in HFIR, Journal of Nuclear Materials, 141-143 (1986) 929-937.
[65] D.S. Gelles, Microstructural development in reduced activation ferritic alloys irradiated to 200 dpa at 420°C, Journal of Nuclear Materials, 212-215 (1994) 714-719.

[66] E.A. Little, L.P. Stoter, MICROSTRUCTURAL STABILITY OF FAST REACTOR IRRADIATED 10-12%Cr FERRITIC-MARTENSITIC STAINLESS STEELS, in: ASTM Special Technical Publication, 1982, pp. 207-233.
[67] M.B. Toloczko, F.A. Garner, C.R. Eiholzer, Irradiation creep and swelling of the US fusion heats of HT9 and 9Cr-1Mo to 208 dpa at ~ 400°C, Journal of Nuclear Materials, 212-215 (1994) 604-607.
[68] X. jia, Dai, Y., &M. Victoria., Impact of irradiation temperature on the microstructure of F82H martensite/ferritic steel irradiated in a proton and neutron mixed spectrum, journal of Nuclear Materials, 305 (2002) 1-7.
[69] X. Jia, Y. Dai, Microstructure in martensitic steels T91 and F82H after irradiation in SINQ Target-3, Journal of Nuclear Materials, 318 (2003) 207-214.
[70] C. Wassilew, K. Herschbach, E. Materna-Morris, K. Ehrlich, IRRADIATION BEHAVIOUR OF 12% Cr MARTENSITIC STEELS, in, 1984, pp. 607-614.
[71] R.L. Klueh, J.M. Vitek, Elevated-temperature tensile properties of irradiated 9 Cr-1 MoVNb steel, Journal of Nuclear Materials, 132 (1985) 27-31.
[72] R.L. Klueh, J.M. Vitek, Tensile behavior of irradiated 12Cr-1MoVW steel, Journal of Nuclear Materials, 137 (1985) 44-50.
[73] R.L. Klueh, J.M. Vitek, Tensile properties of 9Cr-1MoVNb and 12Cr-1MoVW steels irradiated to 23 dpa at 390 to 550 ° C, Journal of Nuclear Materials, 182 (1991) 230-239.
[74] R.L. Klueh, J.M. Vitek, Fluence and helium effects on the tensile properties of ferritic steels at low temperatures, Journal of Nuclear Materials, 161 (1989) 13-23.
[75] R.L. Klueh, D.J. Alexander, Charpy impact toughness of martensitic steels irradiated in FFRF: effect of heat treatment, in: ASTM Special Technical Publication, 1994, pp. 591-606.
[76] C. Wassilew, K. Ehrlich, Effect of neutron irradiation on the dynamic fracture toughness behavior of the 12% Cr steel MANET-I investigated using subsize V-notch specimens, Journal of Nuclear Materials, 191-194 (1992) 850-854.
[77] X. Jia, Y. Dai, Small punch tests on martensitic/ferritic steels F82H, T91 and Optimax-A irradiated in SINQ Target-3, Journal of Nuclear Materials, 323 (2003) 360-367.
[78] Y. Dai, B. Long, Z.F. Tong, Tensile properties of ferritic/martensitic steels irradiated in STIP-I, Journal of Nuclear Materials, 377 (2008) 115-121.
[79] J. Henry, X. Averty, Y. Dai, J.P. Pizzanelli, Tensile behaviour of 9Cr–1Mo tempered martensitic steels irradiated up to 20dpa in a spallation environment, Journal of Nuclear Materials, 377 (2008) 80-93.
[80] Y. Dai, X. Jia, S.A. Maloy, Annealing effects on mechanical properties and microstructure of F82H irradiated at ⩽60°C with 800MeV protons, Journal of Nuclear Materials, 343 (2005) 241-246.
[81] Y. Dai, G.R. Odette, T. Yamamoto, 1.06 - The Effects of Helium in Irradiated Structural Alloys, in: R.J.M. Konings (Ed.) Comprehensive Nuclear Materials, Elsevier, Oxford, 2012, pp. 141-193.
[82] K. Shiba, A. Hishinuma, Low-temperature irradiation effects on tensile and Charpy properties of low-activation ferritic steels, Journal of Nuclear Materials, 283–287, Part 1 (2000) 474-477.
[83] Y. Dai, W. Wagner, Materials researches at the Paul Scherrer Institute for developing high power spallation targets, Journal of Nuclear Materials, 389 (2009) 288-296.
[84] W.L. Hu, Gelles, D.S., Effects of Radiation on Materials, 14th International Symposium, ASTM STP 956, II (1989) p 453.
[85] J. Rensman, E. Lucon, J. Boskeljon, J. van Hoepen, R. den Boef, P. ten Pierick, Irradiation resistance of Eurofer97 at 300 °C up to 10 dpa, Journal of Nuclear Materials, 329–333, Part B (2004) 1113-1116.
[86] A. Alamo, J.L. Bertin, V.K. Shamardin, P. Wident, Mechanical properties of 9Cr martensitic steels and ODS-FeCr alloys after neutron irradiation at 325 °C up to 42 dpa, Journal of Nuclear Materials, 367–370, Part A (2007) 54-59.
[87] E. Gaganidze, H.C. Schneider, B. Dafferner, J. Aktaa, Embrittlement behavior of neutron irradiated RAFM steels, Journal of Nuclear Materials, 367–370, Part A (2007) 81-85.

[88] H.-S. Yu, E.-G. Na, S.-H. Chung, Assessment of stress corrosion cracking susceptibility by a small punch test, Fatigue & Fracture of Engineering Materials & Structures, 22 (1999) 889-896.
[89] J. Isselin, T. Shoji, Crack initiation resistance characterization of weld by small-punch test in boiling water reactor environment, International Journal of Pressure Vessels and Piping, 93–94 (2012) 22-28.
[90] M.S. Bapna, T. Mori, M. Meshii, The observation of slip channels in quenched gold, Philosophical Magazine, 17 (1968) 177-184.
[91] M.S. Bapna, M. Meshii, The interaction of dislocations and tetrahedral stacking faults in quench-hardened gold single crystals, MT, 3 (1972) 3205-3211.
[92] M.S. Bapna, M. Meshii, Deformation of quench-hardened gold single crystals, Materials Science and Engineering, 16 (1974) 181-191.
[93] T. Mori, M. Meshii, Plastic deformation of quench-hardened aluminum single crystals, Acta Metallurgica, 17 (1969) 167-175.
[94] C.H. Ritschel, Dissertation A, AdW der DDR, ZFW Dresden, (1982).
[95] H. Gleiter, E. Hornbogen, Theorie der Wechselwirkung von Versetzungen mit kohärenten geordneten Zonen (I), physica status solidi (b), 12 (1965) 235-250.
[96] M.J. Blackburn, Williams, J.C., Strength deformation modes and fracture in TiAl alloys, Trans. Am. Soc. Metals, 62 (1969) 398-409.
[97] T.H. Sanders, Staley, J.T., Fatigue and Microstructure, ASM, Metals, (1978) 467-522.
[98] A. Gysler, G. Lütjering, V. Gerold, Deformation behavior of age-hardened Ti-Mo alloys, Acta Metallurgica, 22 (1974) 901-909.
[99] T. Diaz de la Rubia, H.M. Zbib, T.A. Khraishi, B.D. Wirth, M. Victoria, M.J. Caturla, Multiscale modelling of plastic flow localization in irradiated materials, Nature, 406 (2000) 871-874.
[100] D.J. Edwards, B.N. Singh, J.B. Bilde-Sørensen, Initiation and propagation of cleared channels in neutron-irradiated pure copper and a precipitation hardened CuCrZr alloy, Journal of Nuclear Materials, 342 (2005) 164-178.
[101] J.S. Robach, I.M. Robertson, B.D. Wirth, A. Arsenlis, In-situ transmission electron microscopy observations and molecular dynamics simulations of dislocation-defect interactions in ion-irradiated copper, Philosophical Magazine, 83 (2003) 955-967.
[102] Z. Yao, R. Schäublin, M. Victoria, The microstructure and tensile properties of pure Ni single crystal irradiated with high energy protons, Journal of Nuclear Materials, 307–311, Part 1 (2002) 374-379.
[103] Z. Jiao, J.T. Busby, G.S. Was, Deformation microstructure of proton-irradiated stainless steels, Journal of Nuclear Materials, 361 (2007) 218-227.
[104] M. Sugiyama, K. Fukumoto, H. Matsui, Dislocation channel formation process in V–Cr–Ti alloys irradiated below 300 °C, Journal of Nuclear Materials, 329–333, Part A (2004) 467-471.
[105] B.N. Singh, A. Horsewell, P. Toft, Effects of neutron irradiation on microstructure and mechanical properties of pure iron, Journal of Nuclear Materials, 271–272 (1999) 97-101.
[106] N. Hashimoto, S.J. Zinkle, R.L. Klueh, A.F. Rowcliffe, K. Shiba, Deformation Mechanisms in Ferritic/martensitic Steels Irradiated in HFIR, MRS Online Proceedings Library, 650 (2000) null-null.
[107] K. Farrell, T.S. Byun, N. Hashimoto, Deformation mode maps for tensile deformation of neutron-irradiated structural alloys, Journal of Nuclear Materials, 335 (2004) 471-486.
[108] T.S. Byun, E.H. Lee, J.D. Hunn, Plastic deformation in 316LN stainless steel – characterization of deformation microstructures, Journal of Nuclear Materials, 321 (2003) 29-39.
[109] Y. Dai, X. Jia, J.C. Chen, W.F. Sommer, M. Victoria, G.S. Bauer, Microstructure of both as-irradiated and deformed 304L stainless steel irradiated with 800 MeV protons, Journal of Nuclear Materials, 296 (2001) 174-182.
[110] S.J. Zinkle, Y. Matsukawa, Observation and analysis of defect cluster production and interactions with dislocations, Journal of Nuclear Materials, 329–333, Part A (2004) 88-96.

[111] M. Niewczas, R.G. Hoagland, Molecular dynamic studies of the interaction of a/6⟨112⟩ Shockley dislocations with stacking fault tetrahedra in copper. Part II: Intersection of stacking fault tetrahedra by moving twin boundaries, Philosophical Magazine, 89 (2009) 727-746.
[112] A. Serra, D.J. Bacon, Interaction of a moving { } twin boundary with perfect dislocations and loops in a hcp metal, Philosophical Magazine, 90 (2009) 845-861.
[113] J.N. Johnson, R.W. Rohde, Dynamic Deformation Twinning in Shock-Loaded Iron, Journal of Applied Physics, 42 (1971) 4171-4182.
[114] L.E. Murr, M.A. Meyers, C.S. Niou, Y.J. Chen, S. Pappu, C. Kennedy, Shock-induced deformation twinning in tantalum, Acta Materialia, 45 (1997) 157-175.
[115] C.Q. Chen, J.N. Florando, M. Kumar, K.T. Ramesh, K.J. Hemker, Incipient deformation twinning in dynamically sheared bcc tantalum, Acta Materialia, 69 (2014) 114-125.
[116] J. Bošanský, T. Šmida, Deformation twins — probable inherent nuclei of cleavage fracture in ferritic steels, Materials Science and Engineering: A, 323 (2002) 198-205.
[117] A. Higginbotham, M. Suggit, E. Bringa, P. Erhart, J. Hawreliak, G. Mogni, N. Park, B. Remington, J. Wark, Molecular dynamics simulations of shock-induced deformation twinning of a body-centered-cubic metal, Physical Review B, 88 (2013) 104105.
[118] W.D. Biggs, P.L. Pratt, The deformation and fracture of alpha-iron at low temperatures, Acta Metallurgica, 6 (1958) 694-703.
[119] T.G. Lindley, R.E. Smallman, The plastic deformation of polycrystalline vanadium at low temperatures, Acta Metallurgica, 11 (1963) 361-371.
[120] T. Šmida, J. Bošanský, Deformation twinning and its possible influence on the ductile brittle transition temperature of ferritic steels, Materials Science and Engineering: A, 287 (2000) 107-115.
[121] T. Šmida, J. Bošanský, Fracture mode transition phenomena in steels as a consequence of the change of operating deformation mode, Materials Science and Engineering: A, 323 (2002) 21-26.
[122] M.W. Chen, J.W. McCauley, D.P. Dandekar, N.K. Bourne, Dynamic plasticity and failure of high-purity alumina under shock loading, Nat Mater, 5 (2006) 614-618.
[123] B.A. Simkin, M.A. Crimp, T.R. Bieler, A factor to predict microcrack nucleation at γ–γ grain boundaries in TiAl, Scripta Materialia, 49 (2003) 149-154.
[124] B.A. Simkin, B.C. Ng, M.A. Crimp, T.R. Bieler, Crack opening due to deformation twin shear at grain boundaries in near-γ TiAl, Intermetallics, 15 (2007) 55-60.
[125] T.R. Bieler, A. Fallahi, B.C. Ng, D. Kumar, M.A. Crimp, B.A. Simkin, A. Zamiri, F. Pourboghrat, D.E. Mason, Fracture initiation/propagation parameters for duplex TiAl grain boundaries based on twinning, slip, crystal orientation, and boundary misorientation, Intermetallics, 13 (2005) 979-984.
[126] Y. Zhang, P.C. Millett, M. Tonks, B. Biner, Deformation-twin-induced grain boundary failure, Scripta Materialia, 66 (2012) 117-120.
[127] Y. Zhang, P.C. Millett, M. Tonks, S.B. Biner, Deformation twins in nanocrystalline body-centered cubic Mo as predicted by molecular dynamics simulations, Acta Materialia, 60 (2012) 6421-6428.
[128] J.P. Hirth, Theory of Dislocations, Krieger Pub Co, (1982).
[129] A.H. Cottrell, B.A. Bilby, LX. A mechanism for the growth of deformation twins in crystals, The London, Edinburgh, and Dublin Philosophical Magazine and Journal of Science, 42 (1951) 573-581.
[130] P. Pirouz, Deformation mode in silicon, slip or twinning?, Scripta Metallurgica, 21 (1987) 1463-1468.
[131] K.P.D. Lagerlöf, J. Castaing, P. Pirouz, A.H. Heuer, Nucleation and growth of deformation twins: A perspective based on the double-cross-slip mechanism of deformation twinning, Philosophical Magazine A, 82 (2002) 2841-2854.
[132] T.L. Altshuler, J.W. Christian, Low temperature twinning in pure iron, Acta Metallurgica, 14 (1966) 903-908.
[133] J.W. Christian, S. Mahajan, Deformation twinning, Progress in Materials Science, 39 (1995) 1-157.
[134] L.M. Hsiung, D.H. Lassila, Shock-induced deformation twinning and omega transformation in tantalum and tantalum–tungsten alloys, Acta Materialia, 48 (2000) 4851-4865.

[135] J. Marian, W. Cai, V.V. Bulatov, Dynamic transitions from smooth to rough to twinning in dislocation motion, Nat Mater, 3 (2004) 158-163.
[136] E.B. Simonsen, Twinning in iron, Acta Metallurgica, 8 (1960) 809-810.
[137] M. Chen, E. Ma, K.J. Hemker, H. Sheng, Y. Wang, X. Cheng, Deformation Twinning in Nanocrystalline Aluminum, Science, 300 (2003) 1275-1277.
[138] J. Wang, Z. Zeng, C.R. Weinberger, Z. Zhang, T. Zhu, S.X. Mao, In situ atomic-scale observation of twinning-dominated deformation in nanoscale body-centred cubic tungsten, Nat Mater, 14 (2015) 594-600.
[139] Q. Yu, Z.-W. Shan, J. Li, X. Huang, L. Xiao, J. Sun, E. Ma, Strong crystal size effect on deformation twinning, Nature, 463 (2010) 335-338.
[140] W.Z. Han, G.M. Cheng, S.X. Li, S.D. Wu, Z.F. Zhang, Deformation Induced Microtwins and Stacking Faults in Aluminum Single Crystal, Physical Review Letters, 101 (2008) 115505.
[141] R.J. McCabe, I.J. Beyerlein, J.S. Carpenter, N.A. Mara, The critical role of grain orientation and applied stress in nanoscale twinning, Nat Commun, 5 (2014).
[142] D.H. Warner, W.A. Curtin, S. Qu, Rate dependence of crack-tip processes predicts twinning trends in f.c.c. metals, Nat Mater, 6 (2007) 876-881.
[143] S. Hai, E.B. Tadmor, Deformation twinning at aluminum crack tips, Acta Materialia, 51 (2003) 117-131.
[144] L. Liu, H.C. Wu, J. Wang, S.K. Gong, S.X. Mao, Twinning-dominated nucleation, propagation and deflection of crack in molybdenum characterized with in situ transmission electron microscopy, Philosophical Magazine Letters, 94 (2014) 225-232.
[145] A. Spielmannová, A. Machová, P. Hora, Transonic twins in 3D bcc iron crystal, Computational Materials Science, 48 (2010) 296-302.
[146] V.A. Borodin, P.V. Vladimirov, Molecular dynamics simulations of quasi-brittle crack development in iron, Journal of Nuclear Materials, 415 (2011) 320-328.
[147] B.Q. Li, M.L. Sui, B. Li, E. Ma, S.X. Mao, Reversible Twinning in Pure Aluminum, Physical Review Letters, 102 (2009) 205504.
[148] H. Zhang, B. Long, Y. Dai, Metallography studies and hardness measurements on ferritic/martensitic steels irradiated in STIP, Journal of Nuclear Materials, 377 (2008) 122-131.
[149] Y. Dai, X. Jia, R. Thermer, D. Hamaguchi, K. Geissmann, E. Lehmann, H.P. Linder, M. James, F. Gröschel, W. Wagner, G.S. Bauer, The second SINQ target irradiation program, STIP-II, Journal of Nuclear Materials, 343 (2005) 33-44.
[150] J.T. Busby, M.C. Hash, G.S. Was, The relationship between hardness and yield stress in irradiated austenitic and ferritic steels, Journal of Nuclear Materials, 336 (2005) 267-278.
[151] R.F. Egerton, Electron Energy Loss Spectroscopy in the Electron Microscope, Plenum, New York, (1996).
[152] K. Iakoubovskii, K. Mitsuishi, Y. Nakayama, K. Furuya, Mean free path of inelastic electron scattering in elemental solids and oxides using transmission electron microscopy: Atomic number dependent oscillatory behavior, Physical Review B, 77 (2008) 104102.
[153] J. Schindelin, I. Arganda-Carreras, E. Frise, V. Kaynig, M. Longair, T. Pietzsch, S. Preibisch, C. Rueden, S. Saalfeld, B. Schmid, J.-Y. Tinevez, D.J. White, V. Hartenstein, K. Eliceiri, P. Tomancak, A. Cardona, Fiji: an open-source platform for biological-image analysis, Nat Meth, 9 (2012) 676-682.
[154] J.F. Ziegler, M.D. Ziegler, J.P. Biersack, SRIM – The stopping and range of ions in matter (2010), Nuclear Instruments and Methods in Physics Research Section B: Beam Interactions with Materials and Atoms, 268 (2010) 1818-1823.
[155] Z. Tong, Y. Dai, Tensile properties of the ferritic martensitic steel F82H after irradiation in a spallation target, Journal of Nuclear Materials, 385 (2009) 258-261.
[156] T. Zhang, C. Vieh, K. Wang, Y. Dai, Irradiation-induced evolution of mechanical properties and microstructure of Eurofer 97, Journal of Nuclear Materials, 450 (2014) 48-53.

[157] X. Jia, The effects of simultaneous radiation damage and helium production on the microstructure and resulting mechanical properties of spallation source candidate materials, PhD Thesis, Ecole Polytechnique Federale De Lausanne, (2002).
[158] K.D. Zilnyk, V.B. Oliveira, H.R.Z. Sandim, A. Möslang, D. Raabe, Martensitic transformation in Eurofer-97 and ODS-Eurofer steels: A comparative study, Journal of Nuclear Materials, 462 (2015) 360-367.
[159] C. Vieh, Hardening induced by radiation damage and helium in structural materials, PhD Thesis, Ecole polytechnique federale de Lausanne, (2015).
[160] A.K. Seeger, On the theory of radiation damage and radiation hardening, In: Proceedings of the Second United Nations International Conference on The Peaceful Uses of Atomic Energy, 6 (1958) 250-273.
[161] O. E, Symposium on Internal Stresses in Metals and Alloys, The Institute of Metals, London, (1948).
[162] B. A.L., in Proceedings, Second International Conference on the Strength of Metals and Alloys, American Society for Metals, (1970) 693-728.
[163] M.L. Grossbeck, 1.04 - Effect of Radiation on Strength and Ductility of Metals and Alloys, in: R.J.M. Konings (Ed.) Comprehensive Nuclear Materials, Elsevier, Oxford, 2012, pp. 99-122.
[164] V. Kuksenko, C. Pareige, P. Pareige, Y. Dai, Production and segregation of transmutation elements Ca, Ti, Sc in the F82H steel under mixed spectrum irradiation of high energy protons and spallation neutrons, Journal of Nuclear Materials, 447 (2014) 189-196.
[165] L. Peng, Y. Dai, Helium-induced hardening effect in ferritic/martensitic steels F82H and Optimax-A irradiated in a mixed spectrum of high energy protons and spallation neutrons, Journal of Nuclear Materials, 417 (2011) 996-1000.
[166] X.Y. Liu, S.B. Biner, Molecular dynamics simulations of the interactions between screw dislocations and self-interstitial clusters in body-centered cubic Fe, Scripta Materialia, 59 (2008) 51-54.
[167] P.V. Durgaprasad, B.K. Dutta, R.K. Singh, Assessment of irradiation hardening by DD simulations, Computational Materials Science, 95 (2014) 393-398.
[168] F. Bergner, C. Pareige, M. Hernández-Mayoral, L. Malerba, C. Heintze, Application of a three-feature dispersed-barrier hardening model to neutron-irradiated Fe–Cr model alloys, Journal of Nuclear Materials, 448 (2014) 96-102.
[169] A. Prokhodtseva, Modelling oriented investigations of primary radiation damage in ultra high purity Fe and FeCr alloys, PhD Thesis, Ecole polytechnique federale de Lausanne, (2013).
[170] P.V. Durgaprasad, B.K. Dutta, R.K. Singh, Assessment of irradiation hardening by DD simulations, Computational Materials Science, 95 (2014) 393-398.
[171] Y. Dai, G.R. Odette, T. Yamamoto, The Effects of Helium in Irradiated Structural Alloys, (2012) 141-193.
[172] G.R. Odette, T. Yamamoto, H.J. Rathbun, M.Y. He, M.L. Hribernik, J.W. Rensman, Cleavage fracture and irradiation embrittlement of fusion reactor alloys: mechanisms, multiscale models, toughness measurements and implications to structural integrity assessment, Journal of Nuclear Materials, 323 (2003) 313-340.
[173] N.E. Dowling, Mechanical Behavior of Materials: engineering methods for deformation, fracture, and fatigue, Prentice-Hall, New Jersey, (1999).
[174] P. Spätig, R. Bonadé, G.R. Odette, J.W. Rensman, E.N. Campitelli, P. Mueller, Plastic flow properties and fracture toughness characterization of unirradiated and irradiated tempered martensitic steels, Journal of Nuclear Materials, 367–370, Part A (2007) 527-538.
[175] E.H. Lee, T.S. Byun, J.D. Hunn, K. Farrell, L.K. Mansur, Origin of hardening and deformation mechanisms in irradiated 316 LN austenitic stainless steel, Journal of Nuclear Materials, 296 (2001) 183-191.

[176] E.H. Lee, T.S. Byun, J.D. Hunn, M.H. Yoo, K. Farrell, L.K. Mansur, On the origin of deformation microstructures in austenitic stainless steel: part I—microstructures, Acta Materialia, 49 (2001) 3269-3276.
[177] E.H. Lee, M.H. Yoo, T.S. Byun, J.D. Hunn, K. Farrell, L.K. Mansur, On the origin of deformation microstructures in austenitic stainless steel: Part II—Mechanisms, Acta Materialia, 49 (2001) 3277-3287.
[178] M. Sauzay, K. Vor, Influence of plastic slip localization on grain boundary stress fields and microcrack nucleation, Engineering Fracture Mechanics, 110 (2013) 330-349.
[179] G.R. Odette, M.Y. He, E.G. Donahue, P. Spätig, T. Yamamoto, Modeling the multiscale mechanics of flow localization-ductility loss in irradiation damaged bcc alloys, Journal of Nuclear Materials, 307–311, Part 1 (2002) 171-178.
[180] M.A. Meyers, O. Vöhringer, V.A. Lubarda, The onset of twinning in metals: a constitutive description, Acta Materialia, 49 (2001) 4025-4039.
[181] A. Ojha, H. Sehitoglu, L. Patriarca, H.J. Maier, Twin nucleation in Fe-based bcc alloys—modeling and experiments, Modelling and Simulation in Materials Science and Engineering, 22 (2014) 075010.
[182] L. Wang, P. Liu, P. Guan, M. Yang, J. Sun, Y. Cheng, A. Hirata, Z. Zhang, E. Ma, M. Chen, X. Han, In situ atomic-scale observation of continuous and reversible lattice deformation beyond the elastic limit, Nat Commun, 4 (2013).

Curriculum Vitae

Personal

Name	Kun Wang
Date of birth	08th November, 1986
Place of birth	Anhui, China
Citizenship	China

Education

2011-2015	PhD student, Department of material science and engineering, École Polytechnique Fédérale de Lausanne (EPFL), Switzerland. The work was performed at the Laboratory of Nuclear Materials of NES, Paul Scherrer Institue, Villigen, Switzerland.
2008-2011	Master in Material Physics and Chemistry, Institute of Solid Physics, China Academy of Sciences, Hefei, China.
2004-2008	Bachelor in Powder Material Science and Engineering, Central South University, Changsha, China.

List of Publications

[1] **K. Wang**, Y. Dai, P. Spätig, Microstructure and fracture behavior of F82H steel under different irradiation and tensile test conditions, Journal of Nuclear Materials (2015), http://dx.doi.org/10.1016/j.jnucmat.2015.09.031
[2] T. Zhang, C. Vieh, **K. Wang**, Y. Dai, Irradiation-induced evolution of mechanical properties and microstructure of Eurofer 97, Journal of Nuclear Materials, 450, 48-53 (2014).
[3] **K. Wang**, X. P. Wang, R. Liu, T. Hao, C. S. Liu and Q. F. Fang, The study on the microwave sintering of tungsten at relatively low temperature, Journal of Nuclear Materials, 431, 206-211 (2012).
[4] R. Liu, T. Hao, **K. Wang**, T. Zhang, X. P. Wang, C. S. Liu and Q. F. Fang, Microwave sintering of W/Cu functionally graded materials, Journal of Nuclear Materials, 431, 196-201 (2012).
[5] Y. Zhou, **K. Wang**, R. Liu, X. P. Wang, C. S. Liu and Q. F. Fang, High performance tungsten synthesized by microwave sintering method, Int. Journal of Refractory Metals and Hard Materials, 34, 13-17 (2012).
[6] D.H. Zhu, **K. Wang**, Q.F. Fang, The optimization design of first- wall W-Cu functionally graded materials, Rare Metal Materials and Engineering (Chinese), 40,1658-1661 (2011).

Presentations at conferences and workshops

- 12th International Workshop on Spallation Materials Technology, Bregenz, Austria, Oct 19-23, 2014
  Oral presentation: Deformation mechanisms of irradiated ferritic/martensitic steels
- NES PhD Day, Villigen, Switzerland, May 22, 2013.
  Oral presentation: Embrittlement induced by the Synergistic Effects of Radiation Damage and Helium in Structural Materials
- 16th International Conference on Fusion Reactor Materials, Beijing, China, Oct 20-25, 2013
  Poster presentation: Embrittlement induced by the Synergistic Effects of Radiation Damage and Helium in Structural Materials
- GETMAT International Workshop, Berlin, Germany, Sep 17-19, 2013.
  Poster presentation: Embrittlement induced by the Synergistic Effects of Radiation Damage and Helium in Structural Materials